No two neurons are alike: degeneracy in neurons and neural circuits

By

Kun Tian
Doctor of Philosophy

Graduate Division of Biological and Biomedical Sciences
Neuroscience

Astrid A. Prinz
Advisor

Gordon J. Berman
Committee Member

Robert Butera
Committee Member

Shawn Hochman
Committee Member

Dieter Jaeger
Committee Member

Peter Wenner
Committee Member

Accepted:

Lisa A. Tedesco, Ph.D.
Dean of the James T. Laney School of Graduate Studies

Date

No two neurons are alike: degeneracy in neurons and neural circuits

By

Kun Tian
B.S. University of Illinois at Urbana-Champaign, 2013

Advisor: Astrid A. Prinz, Ph.D.

An abstract of
A dissertation submitted to the Faculty of the
James T. Laney School of Graduate Studies of Emory University
in partial fulfillment of the requirements for the degree of
Doctor of Philosophy
in Neuroscience
2019

Abstract

No two neurons are alike: degeneracy in neurons and neural circuits

By Kun Tian

Neurons and neural circuits need to balance flexibility with stability to constantly adapt to the changing environment while maintaining stable outputs. One of the candidate mechanisms is degeneracy, which refers to the phenomenon that different combinations of a neuron or neural circuit's parameters (i.e. degenerate solutions) can give rise to similar neural activity. Degeneracy has been widely observed in invertebrate and vertebrate neural systems, yet still little is known about relationships among the degenerate solutions and how they relate to the function of neurons and neural circuits. Combining experimental data with computational modeling, we explored the questions above in two neural systems: the pyloric circuit in the crab *Cancer borealis* and the sympathetic postganglionic neurons (SPNs) in mice.

The pyloric circuit generates a stereotypical rhythm, and multiple combinations of its cellular and synaptic parameters can produce similar pyloric rhythm. To explore the questions above, we measured the linear structures of the degenerate solutions, and found that reducing the variability of pyloric rhythm features, but not the number of parameters, led to increased strength of linear structures of the degenerate solutions.

SPNs, the last common motor output of the sympathetic nervous system, pass converged motor commands from the spinal cord to downstream muscles and visceral organs. SPNs located in the thoracic region (tSPNs) innervate vasculature, and a RNA-Seq study identified two types of vasculature-innervating tSPNs, NA2 and NA3, which differ in their cell size, but little is known about whether they differ in excitability and ability to integrate synaptic inputs. We built the first physiologically-realistic model of tSPNs in mice based on experimental data, and then built a database of tSPN model versions that match the cell size of NA2- and NA3-type tSPNs. We found that, compared to NA2-type tSPNs, NA3-type have lower densities of hyperpolarizing currents and higher input resistance, making them more excitable with greater ability to integrate synaptic inputs.

Together, these insights from examining a collection of degenerate solutions instead of a single one will help us better understand how neurons and neural circuits employ degenerate solutions to maintain stable outputs against perturbations and injuries.

No two neurons are alike: degeneracy in neurons and neural circuits

By

Kun Tian

B.S. University of Illinois at Urbana-Champaign, 2013

Advisor: Astrid A. Prinz, Ph.D.

A dissertation submitted to the Faculty of the
James T. Laney School of Graduate Studies of Emory University
in partial fulfillment of the requirements for the degree of
Doctor of Philosophy
in Neuroscience
2019

ACKNOWLEDGEMENTS

The past six years have been challenging, sometimes gloomy, but always intriguing and fulfilling. I am leaving Emory University even more passionate about research than when I came here, which would not have happened without all the support from my family and friends, my lab mates, my mentor and committee members, and the Neuroscience graduate program at Emory University, so I want to take this opportunity to thank all who walk along this journey by my side.

First and foremost, I want to thank my family and friends. Dad, I really appreciate all the support you provided me for the past six years. More importantly, you built courage into me and taught me to face and learn from my mistakes relentlessly. Mom, thank you for your endless love and understanding. Because of you, I become more and more resilient and fearless as days pass by. Thank you to all my friends who kept me rooted during the ups and uplifted during the downs. You managed to distract me from doing research every once a while, and reminded me that life is also about board games, peated whisky, the outdoors, and all the fun times we spent together.

I also want to thank all my lab mates who helped shape my dissertation work. In the Prinz lab, Amber Hudson provided me the experimental data for the work in Chapter 2, and Ryan Hooper taught me to do electrophysiological recordings and all the tricks to keep the crabs healthy. Cengiz Gunay from the Calabrese lab introduced me to multi-objective evolutionary algorithms and helped me kickstart parallel computing. The computational model in Chapter 3 was built upon experimental data collected by Michael McKinnon from the Hochman lab, and the second part of Chapter

3 was inspired by data collected by Celia Li from the Hochman lab. I am deeply grateful to all of your help. Countless people I have met at conferences and summer school also inspired me with thoughts and ideas , which I really appreciate.

Astrid, you have been an amazing mentor for me. I could not make it through this journey without your support and understanding. You gave me the freedom to define and shape the work in Chapter 2, were my bullshit detector when I did not think clearly, and were extremely patient during the years when things did not work. I love you not only as my mentor, but also as my friend.

Thank you to my committee – Gordon Berman, Rob Butera, Shawn Hochman, Dieter Jaeger, and Pete Wenner - for all your support and advice for the past six years. I want to give special thanks to committee members who I have collaborated with. Gordon, I am really fortunate to have you on my committee and am really grateful for all the advice you provided on the work in Chapter 2. Shawn, I admire your ability to turn any talk into a stand-up comedy show, and really appreciate all the patience and advice you gave me for the past few years on the work in Chapter 3.

I am really grateful to have science in my life and to have the opportunity spending six years on one of the gazillion puzzles out there. This experience taught me how to stay calm and focused under pressure, and geared me up for all the scientific adventures in the future. I hope I can return all the fortunes life endowed me with by making something awesome one day.

LIST OF FIGURES

LIST OF TABLES

LIST OF ABBREVIATIONS

AB	anterior burster neuron
AD	autonomic dysreflexia
ANS	autonomic nervous system
CSPG	chondroitin sulfate proteoglycans
C_m	membrane capacitance
CPG	central pattern generator
DE	differential evolution
ES	evolution strategy
GA	genetic algorithm
G_A	conductance of A-type transient potassium current
G_{CaL}	conductance of L-type calcium current
G_{CaT}	conductance of T-type calcium current
G_{CaS}	conductance of S-type calcium current
G_h	conductance of hyperpolarization-activated cation current
G_{KCa}	conductance of calcium-dependent potassium current
G_{Kd}	conductance of delayed-rectifier potassium current
G_{Leak}	conductance of leak current
G_M	conductance of non-inactivating potassium current
G_{MI}	conductance of neuromodulation-dependent inward current

G_{Na}	conductance of fast sodium current
IC	inferior cardiac neuron
LP	lateral pyloric neuron
HP	homeostatic plasticity
HIP	homeostatic intrinsic plasticity
HSP	homeostatic synaptic plasticity
mEPSC	miniature excitatory postsynaptic current
mIPSC	miniature inhibitory postsynaptic current
MOEA	multi-objective evolutionary algorithm
mPSC	miniature postsynaptic current
NMJ	neuromuscular junction
NPY	neuropeptide Y
NSGA II	nondominated sorting genetic algorithm II
PCA	principal component analysis
PD	pyloric dilator neuron
PSO	particle swarm optimization
PY	pyloric constrictor neuron
SCI	spinal cord injury
SNA	spontaneous network activity
SPN	sympathetic postganglionic neuron

STG	stomatogastric ganglion
STNS	stomatogastric nervous system
tSPN	thoracic sympathetic postganglionic neuron
τ_D	decay time constant
τ_m	membrane time constant
τ_R	rise time constant
usAHP	ultra-slow after-hyperpolarization
VD	ventricular dilator neuron

TABLE OF CONTENTS

Chapter 1 General Introduction

To maintain stable outputs, neural circuits need to constantly adapt to developmental changes and environmental perturbations. This ability to adapt implies that neurons and neural circuits possess multiple ways to produce the same (or similar) output given constant changes of their morphological and molecular construction, neuromodulatory inputs, and environment, a property called degeneracy. It refers to the phenomenon that different combinations of the underlying parameters can give rise to similar neural activity or behavior (Edelman and Gally, 2001; Marder and Taylor, 2011; Mason et al., 2015). Degeneracy is prevalent in biological systems. In genetics, the genetic code is degenerate with different codons coding for the same amino acid. In immunology, different antibodies can bind to the same antigen. In this chapter, we focus on degeneracy at the single neuron and the neural circuit level, which has been widely observed in both invertebrate and vertebrate neural systems. For example, the pyloric circuit of the crab *Cancer borealis* generates a stereotyped rhythm to aid in digestion, and multiple combinations of its underlying ion channel densities can produce similar pyloric rhythm (Prinz et al., 2004; Marder and Goaillard, 2006; Ransdell et al., 2013a). In *Caenorhabditis* elegans, degenerate thermoregulation and feeding pathways make these behaviors more robust (Cropper et al., 2016). The pathways to pathological neural states can also be degenerate. For example, hyperexcitability in rat somatosensory afferents can arise from different combinations of the underlying sodium and potassium membrane currents (Rho and Prescott, 2012; Ratté et al., 2014).

Degeneracy is not only important to maintain stable neural activity against developmental changes and perturbations, but also can widen the range of achievable firing rates and aid switching between different behaviors (Drion et al., 2015; Cropper et al., 2016). Although the phenomenon of degeneracy has been widely observed, little is known about structures of the degenerate solutions and how they contribute to maintaining neural activity. What are the structures of the degenerate solutions? Do neurons and neural circuits employ those structures to maintain stable neural activity against developmental changes and perturbations, and if so, how do they do it? In this chapter, we first review experimental and computational studies related to these questions (Section 1.1 and 1.2), and then discuss the computational approach employed in the following chapters to explore these questions (Section 1.3).

1.1 Structures of degenerate parameter sets

Degeneracy can be visualized as a many-to-one mapping from the solution space in the parameter space to the viable region in the output space (Fig 1.1A) (O'Leary and Wyllie, 2011). The parameter space is a high-dimensional space, with each dimension representing one parameter. For this dissertation, parameters of a neural circuit are ion channel densities and synaptic strengths, which together determine neural activities. Each salient feature of neural activities, such as average firing rate, adaptation ratio, etc., is a dimension in the output space. All points in the parameter space that map to the same point or region in the output space are degenerate to each other, and are referred to as degenerate parameter sets or degenerate solutions, where each point in the parameter space is a parameter set of specific values for each ion channel density and/or synaptic strength (Fig 1.1B). All degenerate solutions comprise the solution space.

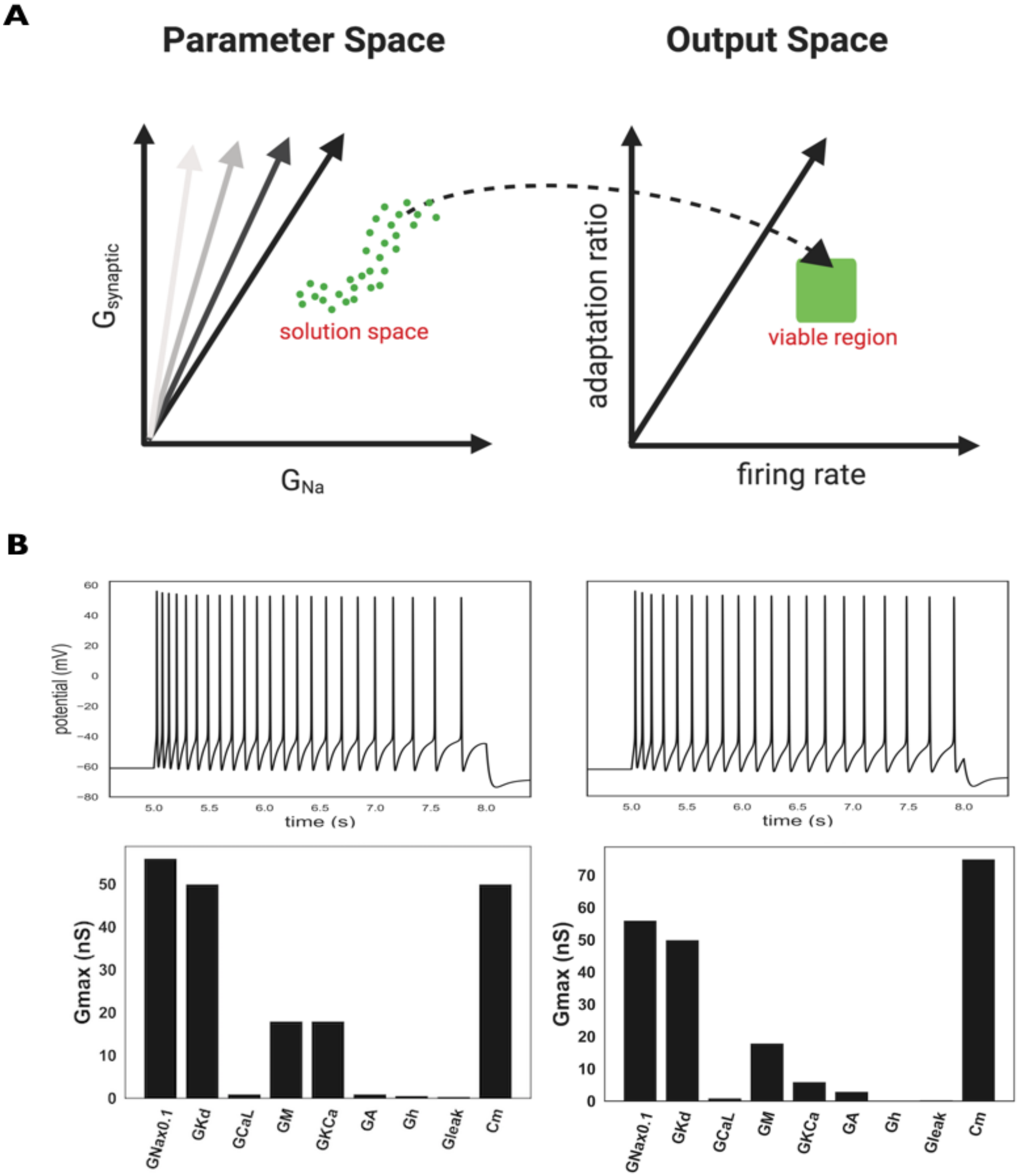

Figure 1.1 Visualizing degeneracy in high-dimensional space. (A) Degeneracy is defined as the mapping from the solution space, which is a subset of the parameter space, to the viable region in the output space. Example used here is the mapping from cellular and synaptic conductances of a mouse thoracic sympathetic postganglionic neuron model to its space of firing output features. **(B)** Neuron models with similar behavior but different parameters. Top: Voltage traces from two physiologically-realistic tSPN models with almost identical firing rates and spike rate adaptation ratios. Bottom: Parameters for the two tSPN models, which are quite different. G_i parameters is maximal conductance of current i. The model is described in Chapter 3.

1.1.1 Ion channel correlations and sloppiness

Experimental studies have shown the existence of degeneracy in both invertebrates (Grashow et al., 2010; Beverly et al., 2011; Zhao and Golowasch, 2012; Lamb and Calabrese, 2013) and vertebrates (Leonardo, 2005; Swensen and Bean, 2005; Cao and Oertel, 2011; Amendola et al., 2012), but we lack a comprehensive understanding of the structures of those degenerate solutions and how they relate to the function of neurons and neural circuits.

The pyloric circuit in the crab *Cancer borealis* is a good model to study structures of degenerate solutions because the underlying cellular and synaptic components and the anatomical connections between neurons have been identified and well characterized in experiments. Specifically, the pyloric circuit is a central pattern generator consisting of three types of neurons called pyloric dilator (PD), lateral pyloric (LP) and pyloric constrictor (PY), which burst in turn to generate a stereotyped tri-phasic pyloric rhythm. All neurons contain a rich repertoire of ion channels and are connected by two types of inhibitory synapses, which are glutamatergic and cholinergic.

One type of the structure found in pyloric circuit's solution space is the linear correlation between the density of two ion channels, a phenomenon called ion channel correlation. Both experimental and computational studies have shown that different combinations of the ion channel densities and synaptic strengths can produce similar pyloric rhythms (Prinz et al., 2004; Grashow et al., 2010; Ransdell et al., 2013a), and have further identified ion channel correlations needed to maintain the pyloric rhythm. For example, a positive correlation between a hyperpolarization-activated cation current (I_h)

and a fast-inactivating potassium current (I_A) has been shown to maintain spiking frequency in the PD neuron (Zhao and Golowasch, 2012) (Fig 1.2A). Another study in a motor neuron of the crab pyloric circuit found that I_A is also coupled with a calcium-dependent potassium current (I_{KCa}) and that blocking one leads to a rapid increase in the other (Ransdell et al., 2012). There are a few up-to-date reviews on ion channel correlations in single neurons (Golowasch, 2014; Schulz and Lane, 2017), but little is known about correlations at the neural circuit level, especially correlations between cellular and synaptic currents (Taylor et al., 2009).

Knowing that certain ion channel correlations maintain the pyloric rhythm, we wondered how many and which pairs are linearly correlated. These questions are challenging to study in experiments, but can be investigated using conductance-based models of a single neuron or of the pyloric circuit. Such studies have further identified ion channel correlations that were difficult to identify in experiments. For example, in a PD neuron model, spike phase patterns are maintained by covarying a fast sodium current (I_{Na}) and a transient calcium current (I_{CaT}) (Soofi et al., 2012). Another study showed that covariation of I_{CaT} and a delayed-rectifier potassium current (I_{Kd}) preserved the output of motor neurons (Ball et al., 2010). A synthesis of ion channel correlations across cell types indicates that they are distinct in different cell types and therefore can be a defining characteristic of cell identity (Hudson and Prinz, 2010; Temporal et al., 2014; Schulz and Lane, 2017).

However, most of the ion channel pairs in these models show weak to no correlation. A study constructed approximately 1,000 degenerate model instances of the LP neuron, and found that over 90% of the ion channel pairs examined had weak correlation coefficients between -0.2 and 0.2 (Taylor et al., 2009). Another model of the PD neuron showed that combinations of two ion channel densities leading to different types of neural activities usually form a continuous region, but each region shows weak to no linear correlations internally (Bialek, 2012; LeMasson et al., 1993) (Fig 1.2B). Similar results were also seen in other invertebrate and vertebrate neural circuits (Achard and De Schutter, 2006; Doloc-Mihu and Calabrese, 2014; Anirudhan and Narayanan, 2015), indicating that this is a universal phenomenon.

Combining these findings, we see that ion channel correlations are generally absent or weak, with a few strong ones regulating and maintaining functional outputs. This observation indicates sloppiness in the parameter spaces of these models. Models are sloppy if the simulated neural activities they produce are sensitive to changes of a small number of parameters or parameter combinations (i.e. stiff parameters) and insensitive to changes of the others (i.e. sloppy parameters) (Daniels et al., 2008; Transtrum et al., 2015) (Fig 1.2C). Sloppiness is a general feature of models with multiple parameters, as even a neuron model containing just five membrane currents can exhibit sloppiness (Goldman et al., 2001). This can be understood intuitively: ionic currents are either inward or outward, and one type of inward current (e.g. I_{Na}) can be reduced by some amount while the neural activity remains invariant as long as the reduction is balanced by changes in other inward or outward currents. Sloppiness analysis can be combined with experiments to understand how populations of neurons maintain stable outputs. A recent experiment simultaneously recorded spiking activities from hundreds of hippocampal neurons cultured on high-density multi-electrode arrays, and found that firing rate was maintained at the population level even though single neurons exhibited considerable spontaneous firing rate fluctuations (Slomowitz et al., 2015). A follow-up study applied the analysis of sloppiness to recordings from cultured hippocampal neurons and found that the spontaneous fluctuations exhibited by single neurons tended to occur along sloppy dimensions in parameter space (Panas et al., 2015).

1.1.2 From linear to nonlinear structures

Ion channel correlations only characterize linear relationships between ion channels, so although most correlations were weak in computational studies, this does not mean that there are no other structures contained in degenerate parameter sets. For example, an experimental study found that coregulation of a triplet of ionic channel densities was needed to maintain output features such as burst period and duration (Zhao and Golowasch, 2012). Modeling studies also found that for neuron models that produce similar outputs, the pairwise distributions of ion channel densities could be nonlinear. For example, the distribution of I_{Na} and I_{Kd} was L-shaped for all instances of a neuron model that generated one-spike burster activity, but the average I_{Na} and I_{Kd} over all those instances failed to produce the same neural activity because it fell outside the L-shaped solution space for one-spike bursting (Golowasch et al., 2002) (Fig 1.2D). Similar results were also observed in a more complex cerebellar Purkinje neuron model (Achard and De Schutter, 2006). In theory, nonlinear distributions of ion channel densities could take many forms, such as donut-shaped or banana-shaped, to name a few (Prinz, 2010a; Marder and Taylor, 2011). All these studies call for an open-minded interpretation of data when it comes to extracting structures out of degenerate solutions.

Nonlinear pairwise distributions of ion channel densities, such as donut-shaped or banana-shaped, are theoretical scenarios. Quite often, the distributions from experimental data or computational models are irregular and noisy, making it challenging to discern any patterns or structures. In this scenario, we can start by investigating whether the degenerate parameter sets are connected to each other in parameter space, which would allow for smooth transitions from one degenerate solution to another when the system is perturbed. One analysis of a canonical pyloric neuron model showed that although all bursting model instances scattered into 30 disconnected region in parameters space, 99.99% of them were in the largest region, and the seemingly disconnected 0.01% of bursting solutions were explained by the coarse sampling of parameter space by the simulated parameter combinations (Taylor et al., 2006). Further study showed that bursting neuron models that matched the specific features of the LP neuron in the pyloric circuit fell into a single "island" (Taylor et al., 2009). The observation that degenerate parameter sets generally fall into one connected region in parameter space implies that low-dimensional structures are embedded in the high-dimensional parameter space, and could potentially be extracted using dimensionality reduction and visualization methods. One of the most prevalent dimensionality reduction methods is principal component analysis (PCA), which projects high dimensional data to low-dimensional structures while preserving variance in the data. Dimensionality reduction is one type of visualization technique. Other visualization techniques suitable to analyze data from electrophysiology recordings and conductance-based models include hyperplane fitting, dimensional stacking, and parameterscape (Goldman et al., 2001; Taylor et al., 2006; Gutierrez et al., 2013).

In a nutshell, structures of degenerate parameter sets are sloppy, and are characterized by largely weak ion channel correlations coupled with a few strong ones.

Weak to absent correlations are usually treated as negative results in experiments, but here we argue that from a system perspective, the prevalence of weak ion channel correlations is a feature of degenerate systems and is important for robustness against perturbations. A system with a majority of strong ion channel correlations implies that it is tightly regulated, which may ensure proper function more efficiently under normal conditions but is less robust to perturbations and injuries. Unlike many engineered systems operating under predictable conditions, living systems face unpredictable and constant changes in the environment and it is therefore important that they maintain robustness in many scenarios.

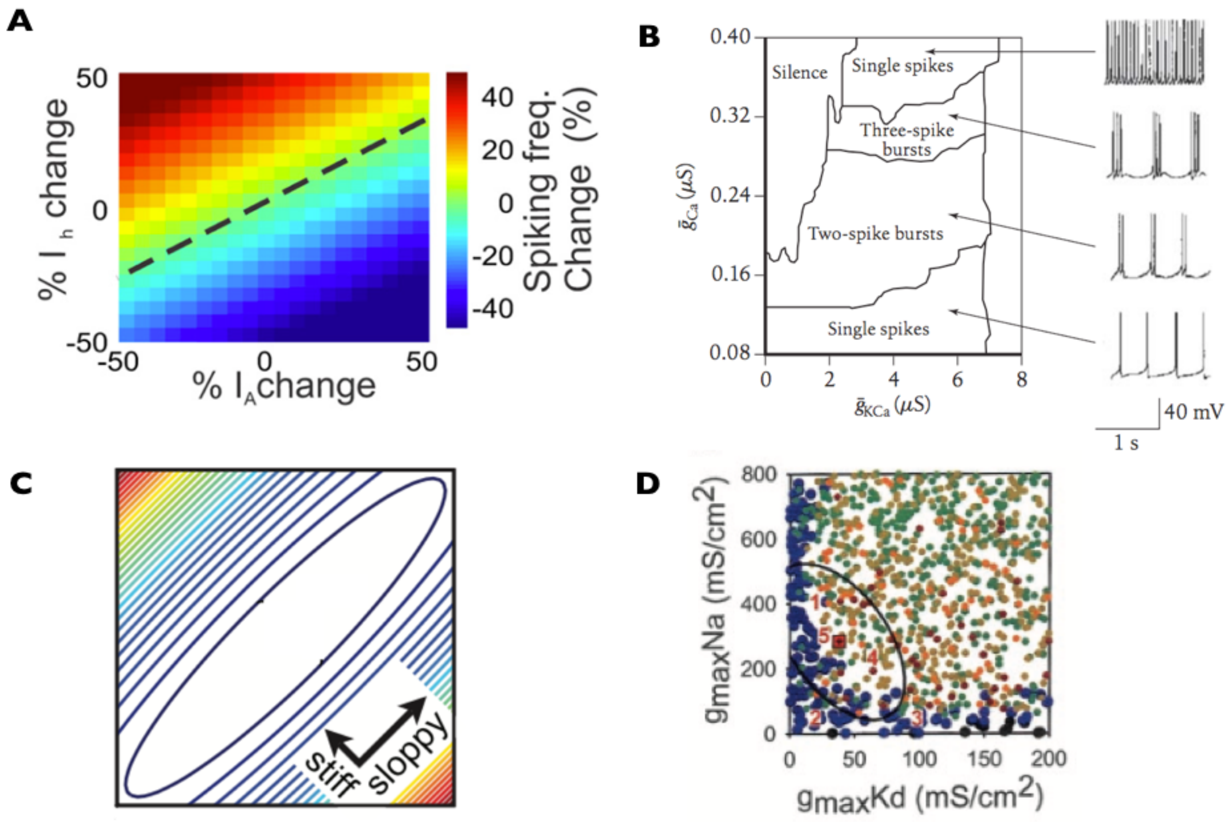

Figure 1.2 Structures of degenerate solutions. (A) A linear correlation between a fast inactivating potassium current (I_A) and a hyperpolarization-activated cation current (I_h) maintains spiking frequency in a crab PD neuron model. Percent change is relative to a canonical spiking model version. Black dashed line indicates degenerate parameter combinations that produce the same

spike frequency as the canonical model. Figure is adapted from Zhao & Golowasch, 2012. **(B)** Combinations of a calcium-dependent potassium current (I_{KCa}) and a calcium current (I_{Ca}) in a model of the crab LP neuron that produce different types of neural activities (i.e. single spikes, two-spike bursts) are separated by nonlinear boundaries. Figure is adapted from Bialek, 2012. **(C)** Stiff and sloppy dimensions in the parameter space. The contours represent constant output value, and color change maps to the rate of change of output values. Figure is adapted from Gutenkunst et al., 2007. **(D)** Number of spikes per burst (black: 0; blue: 1; green: 2; olive: 3; orange: 4; burgundy: 5) for bursting neurons with the indicated maximal conductance of a sodium current (I_{Na}) and a delayed-rectifier potassium current (I_{Kd}). One-spike bursters (blue) lie in an L-shaped region. Combination of average parameter values of one-spike bursters (red square) falls outside L-shaped region and does not produce one-spike bursts, Ellipse indicates range of one standard deviation around the average and also largely falls outside L-shaped region. Figure is adapted from Golowasch et al., 2002.

1.2 Degenerate solutions and homeostatic plasticity mechanisms

Neurons and neural circuits may encounter a wide range of genetic and environmental perturbations during their lifetime, and therefore need to be both flexible to deal with diverse perturbations and reliable to produce stable outputs consistently. Studies across species have shown that, through a rich repertoire of tunable cellular and synaptic parameters, degenerate parameter sets provide the flexibility needed to restore neural activities against a wide range of genetic, anatomical, environmental, or pharmacological perturbations. But exactly how neurons and neural circuits use their repertoire of degenerate parameter sets to restore neural activities is still unclear. One of the possibilities is that degenerate parameter sets contain structures, and neurons and neural circuits employ these structures to move through parameter space to restore neural activities after perturbations and injuries. In the previous section, we discussed linear and nonlinear structures of degenerate parameter sets, such as ion channel correlations and L-shaped distributions of parameters. In this section, we review experimental and computational studies that link these structures to a stability mechanism in the nervous system called homeostatic plasticity.

In the nervous system, neurons and neural circuits possess the ability to restore neural activity against various types of perturbations, a stability mechanism called homeostatic plasticity. Homeostatic plasticity maintains stable outputs of single neurons or neural circuits against developmental changes and perturbations by adjusting the intrinsic excitability of individual neurons and/or the synaptic strengths between neurons. At a single neuron level, perturbed neural activities such as reduced neural firing rate can be compensated by increasing the number of depolarizing channels or reducing the number of hyperpolarizing channels in the membrane (Marder and Goaillard, 2006; Turrigiano, 2011). The neural circuit can also compensate for the reduced firing rate by increasing the excitatory synaptic strengths and/or reducing the inhibitory synaptic strengths in the circuit (Davis, 2006; Turrigiano, 2011). When we take snapshots of the underlying cellular and synaptic parameters at two time points, one before the perturbation, the other after neural activities were restored, we have two parameter sets that match the definition of degeneracy, i.e. different combinations of parameters that produce similar neural activities (Fig 1.3A). By examining the changes of structures in these degenerate parameter sets, we may gain insight into how neurons and neural circuits may employ structures of degenerate parameter sets to restore neural activities. In this section, we will examine the ways in which degeneracy might help maintain stable neural activities by reviewing experimental and computational studies of homeostatic plasticity at both the single neuron level and the neural circuit level.

1.2.1 Single Neuron Level

A few strong ion channel correlations have been shown to play an important role in maintaining neural activities, as discussed in the previous section, raising the question what happens to these strong correlations when neural activities are perturbed and then restored.

The pyloric circuit in the crab *Cancer borealis* generates a stereotyped pyloric rhythm that is maintained by homeostatic plasticity. The pyloric rhythm ceases when descending neuromodulatory inputs are acutely removed, a process called deafferentation. In the absence of neuromodulatory inputs, the pyloric rhythm can recover spontaneously in one to four days (Thoby-Brisson and Simmers, 1998; Golowasch et al., 1999; Luther et al., 2003). A study identified three pairwise ion channel correlations in the PD neurons of the pyloric circuit before deafferentation, which are between a high-threshold potassium current (I_{HTK}) and a fast inactivating potassium current (I_A), between I_{HTK} and a hyperpolarization-activated cation current (I_h), and between I_A and I_h. Four days after deafferentation, when the pyloric rhythm had recovered in the absence of neuromodulation, the correlations between I_{HTK} and I_A and between I_{HTK} and I_h in the PD neuron were disrupted, but the I_A and I_h correlation was preserved (Khorkova and Golowasch, 2007) (Fig 1.3B). A later study showed that this response is specific to cell type, as the same three pairs of ion channel correlations were all preserved after deafferentation in the LP neurons of the pyloric circuit (Temporal et al., 2012). However, these studies only indicate that certain ion channel correlations were not perturbed by deafferentation, but whether and how they contribute to the recovery of the pyloric rhythm are still unclear. We therefore wonder how are ion channel correlations formed and maintained.

Further studies found that monoamines such as serotonin and dopamine enable slow, activity-dependent processes that can maintain the correlation between I_A and I_h (Krenz et al., 2013; 2014; 2015) , but how this correlation is maintained after deafferentation is still unknown. Certain substances in the extracellular matrix may be involved in maintaining the correlations after deafferentation, because removal of the extracellular matrix component chondroitin sulfate proteoglycans (CSPG) delays rhythm recovery after deafferentation (Hudson et al., 2015). Another possibility is that ion channel correlations are maintained at the mRNA level, as several experimental studies have found correlations between the mRNA expression levels encoding ion channel densities (MacLean et al., 2003; Temporal et al., 2012; 2014). A third possibility is that ion channel correlations are maintained by homeostatic tuning rules, as shown in a computational study (O'Leary et al., 2013). Overall, whether ion channel correlations regulate or are regulated by homeostatic tuning rules is still unclear.

Ion channel correlations have also been observed in vertebrate systems, such as mouse hippocampal neurons and cholinergic basal forebrain neurons (Amendola et al., 2012; Tran et al., 2019), but how they contribute to robustness of neural outputs in those systems is less clear, partially because their outputs are less defined than the stereotypical rhythm in the crab *Cancer borealis*, and their robustness is therefore more difficult to define and quantify.

1.2.2 Neural Circuit Level

At the neural circuit level, it is challenging to monitor changes of multiple cellular and synaptic parameters simultaneously in experiments. Therefore, less is known about their degenerate structures in parameter space, but many studies did observe homeostatic regulation at both the cellular and synaptic level, termed homeostatic

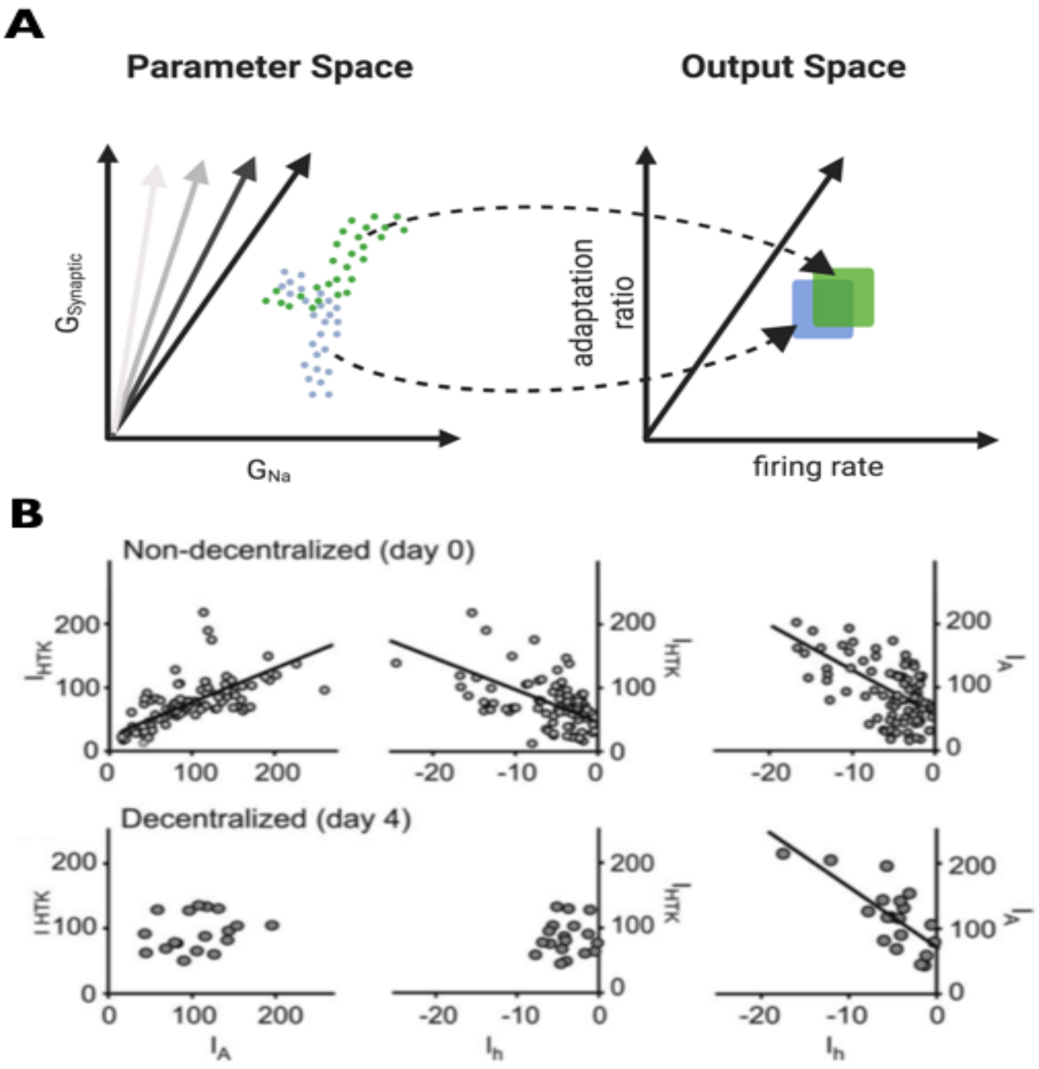

Figure 1.3 Degenerate solutions and homeostatic regulation. (A) A schematic diagram illustrating the change of degenerate solutions after perturbations. Green and blue boxes in the output space correspond to feature values of a neural output before and after a perturbation. The corresponding degenerate solutions for each scenario are shown in the parameter space. Other components of schematic as in Fig 1.1A. **(B)** Ion channel correlations in crab PD neurons before and 4 days after decentralization (see text for details). Each point corresponds to current densities of the two indicated currents measured in a PD neuron. Regression lines are plotted for statistically significant linear correlations ($p < 0.05$). Top: Currents measured before deafferentation. Bottom: Currents measured 4 days after deafferentation. Figure is adapted from Khorkova & Golowasch, 2007.

intrinsic plasticity (HIP) and homeostatic synaptic plasticity (HSP). Examining the temporal order of HIP and HSP occurrence in a neural circuit's response to perturbation may shed light on how neural circuits explore the space of degenerate solutions during homeostatic regulation.

Several studies in both invertebrate and vertebrate neural circuits showed that HIP and HSP mechanisms were recruited sequentially, yet the recruitment order seems to be species- and perturbation-dependent. In certain neural circuits, HIP was recruited before HSP. The developing spinal cord in the chicken embryo, for example, exhibits spontaneous network activity (SNA), where many neurons are coordinated to fire episodic bursts. GABAergic transmission is excitatory in this neural circuit at this developmental stage, and blocking either $GABA_A$ transmission or sodium channels *in ovo* for two days triggers an upscaling of both AMPAergic and GABAergic miniature postsynaptic current (mPSC) amplitude to compensate for the perturbations (Gonzalez-Islas and Wenner, 2006; Wilhelm and Wenner, 2008). Further study showed that blocking $GABA_A$ receptors for 12 hours triggered an increase of intrinsic excitability in the motoneurons of the developing spinal cord first, which occurred in parallel to the SNA recovery, followed by upscaling of synaptic currents after the SNA recovery (Wilhelm et al., 2009). Another study incubated rodent hippocampal slices with CNQX/APV to reduce global network activity for 2 days or 4 days prior to electrophysiology recordings. The slices incubated for 2 days only showed homeostatic changes in cellular excitability, while the slices incubated for 4 days showed both changes in cellular excitability and inhibitory synaptic strength, indicating that in the hippocampal network also, HIP is recruited before HSP of inhibitory synapses (Karmarkar and Buonomano, 2006). These observations suggest that HIP restores neural activity in a coarse-grained manner first, followed by HSP to fine-tune it. A computational study supports the fine-tuning idea by showing that ion channel degeneracy both expands the range of a neuron's firing rate and enables a fine-grained tuning of its firing rate (Drion et al., 2015).

HSP may also be recruited before HIP. For example, in the primary visual cortex of rodents, sensory deprivation by lid suture triggered homeostatic synaptic plasticity first, followed by increased intrinsic excitability (Lambo and Turrigiano, 2013). Interestingly, other types of perturbations to visual inputs like TTX injection and retinal lesions only triggered synaptic scaling to compensate for the perturbation (Maffei and Turrigiano, 2008; Keck et al., 2013). It thus has been proposed that homeostatic intrinsic plasticity is induced when the synaptic form is not sufficient to compensate for drops in sensory drive.

Recruitment of HIP and HSP can also be competitive. At the *Drosophila* neuromuscular junction (NMJ), inhibition of postsynaptic glutamate receptors triggers a homeostatic increase in presynaptic neurotransmitter release to restore muscle depolarization (Davis et al., 1998). Two A-type potassium channel genes, *shal* and *shaker*, are reciprocally coupled to maintain A-channel expression at the NMJ. *shal* mutation is compensated by increased shaker expression. However, this increased shaker expression blocks the expression of trans-synaptic homeostatic signaling at the NMJ, indicating a hierarchical recruitment of HIP and HSP (Bergquist et al., 2010).

HIP and HSP can not only be recruited in order, but also in parallel to cooperatively adjust neural activities. The crab pyloric circuit responds to deafferentation by a decrease of the inhibitory synaptic strength and certain hyperpolarizing ionic currents (i.e. I_{Kd} and I_{KCa}) while enhancing others (i.e. I_h and I_A) (Mizrahi et al., 2001; Thoby-Brisson and Simmers, 2002). In hippocampal networks, both over-excitation and inactivation of $GABA_B$ receptors perturbed firing rate, and tuning at both the intrinsic and synaptic levels was observed to restore firing rate (Slomowitz et al., 2015; Vertkin et al., 2015). Another study that incubated rat hippocampal slices with TTX for 2 days also found homeostatic increases in both miniature excitatory postsynaptic current (mEPSC) frequency and intrinsic excitability (Echegoyen et al., 2007). These studies pose the question whether HIP and HSP are redundant or play different roles to adjust neural activities. An experiment blocking the I_{HTK} in the motor neurons in the crab *Cancer borealis* showed that neural activity was restored by simultaneous changes in the conductance of I_A and strength of electric coupling, with the former accounting for restoring neuronal excitability and the latter for restoring synchrony between neurons (Lane et al., 2016). Another recent computational study suggests HIP and HSP work cooperatively to tune the mean and variance of a single neuron's firing rate, respectively (Cannon and Miller, 2016). These findings suggest that HIP and HSP play different roles to restore perturbed neural activities.

Together, these studies show a rich repertoire of mechanisms recruiting HIP and HSP, depending on the perturbation paradigms (Maffei and Turrigiano, 2008) and cell types (Greenhill et al., 2015). These results indicate that the cellular and synaptic components of degenerate solutions may contain different structures and should be examined separately, which is addressed in Chapter 2.

1.3 Ensemble modeling

The conventional approach in physiologically realistic modeling fits a single computational model to either a typical or an average experimental dataset, and conducts analysis by perturbing this single model. We have gained enormous insights from this conventional approach, but it has limits. Predictions generated from single models are limited because they ignore the intrinsic variability of neurons and circuits, which corresponds to a large pool of neural dynamics and have been observed at the mRNA, conductance and physiology levels in diverse animal models (Schulz et al., 2006, 2007; Wilhelm et al., 2009; Grashow et al., 2010). Also, the distributions of pairs of parameters might be nonlinear, for example banana-shaped, in which case the average of all parameters may fail to produce the same neural activity because the average fell outside the banana-shaped solution space (Golowasch et al., 1992; Golowasch et al., 2002; Marder and Taylor, 2011). These limits become problematic when we aim to understand a phenomenon or mechanism observed at the population level. For example, chronic multi-electrode array recordings in hippocampal slices found that the distribution of spontaneous firing rates and synchrony were maintained at the population but not the individual level (Panas et al., 2015; Slomowitz et al., 2015), a phenomenon that cannot be explained by fitting a model to typical or average data. Another example is degeneracy observed in neurons and neural circuits. To understand these phenomena, we need a different modeling approach called ensemble modeling.

Ensemble modeling refers to the category of parameter fitting and simulation methods that incorporate variability of parameters or neural activities observed in experiments to generate and analyze a group of physiologically-realistic models instead of a single model (Van Geit et al., 2008; Prinz, 2010a). In the context of this dissertation, given predefined measures of neural activities (mean, standard deviation, etc.) and a conductance-based model of the recorded neuron or neural circuit, ensemble modeling methods enable us to find a group of model instances that can produce neural activities falling in the predefined range of outputs. One type of ensemble modeling approach is constructing a database of model instances by systematically varying the parameters in the model, and then filtering the database of resulting parameter combinations by the targeted range of neural activity or neural activities to collect a group of model instances that are different in parameter values but can all produce targeted neural activity. This approach was employed to examine degeneracy in the pyloric circuit and in the Globus pallidus neuron (Prinz et al., 2003, 2004; Günay et al., 2008), and was employed in Chapter 3.

The database approach, also called brute force search, is suitable for a model with a relatively small number of parameters. As the number of parameters grows, the number of data needed to cover the search space evenly and thoroughly grows exponentially, a phenomenon called the curse of dimensionality. In this scenario, a different type of ensemble modeling approach called stochastic optimization is more suitable (Luke, 2013; Van Geit et al., 2008). Stochastic optimization algorithms employ a certain degree of randomness to search for the optimal or a group of optimal parameter sets given the targeted neural activities. One type of stochastic optimization algorithm is called evolutionary algorithms, which is based on the "survival of the fittest" principle of natural selection (Eiben and Smith, 2003). Each parameter set has a fitness value that is based on how closely the modeled neural activity resembles the biological activity, and parameter sets with higher fitness values have a better chance to survive and to breed children. There are many variations of evolutionary algorithms, such as genetic algorithms (GA), evolution strategies (ES), and differential evolution (DE), etc., which have all been employed to fit parameters of neuron or neural circuit models (Achard and De Schutter, 2006; Bahuguna et al., 2017). Another type of stochastic optimization algorithm commonly seen is the particle swarm optimization (PSO) algorithm, which is inspired by the swarming and flocking behaviors in birds. This method was employed to improve ion channel kinetics in a Globus pallidus neuron model (Hendrickson et al., 2011).

Choosing an appropriate ensemble modeling approach for a given experimental dataset requires a deep understanding of both the nitty-gritty and nuances of various algorithms as well as specific features or structures of the given experimental dataset, and is not the focus in this dissertation. For the pyloric circuit model in Chapter 2 that consists of 34 parameters, we employed a variation of the evolutionary algorithms called multi-objective evolutionary algorithms (Fortin et al., 2013; Druckmann et al., 2007; Deb et al., 2002), which is explained in detail in Chapter 2.

Chapter 2 Degenerate solutions in the pyloric circuit of the crab *Cancer borealis*

2.1 Introduction

2.1.1 Background

Degeneracy, the phenomenon that different combinations of a system's parameters can give rise to similar activity or behavior, is prevalent in biological systems (Edelman and Gally, 2001; Marder and Taylor, 2011; Mason, 2015). For example, in genetics, different codons can encode the same amino acid. In the pyloric circuit of the crab *Cancer borealis*, a neural circuit that generates a stereotyped rhythm to aid in digestion, similar pyloric rhythms can be produced by different combinations of the neural circuit's ion channel densities and synaptic strengths (Prinz et al., 2004; Marder and Goaillard, 2006; Ransdell et al., 2013b). The phenomenon of degeneracy has been widely observed in invertebrate and vertebrate neural systems (Leonardo, 2005; Swensen and Bean, 2005; Grashow et al., 2010; Beverly et al., 2011; Cao and Oertel, 2011; Amendola et al., 2012; Zhao and Golowasch, 2012; Lamb and Calabrese, 2013; Tran et al., 2019), yet it is still unclear what the structures of degenerate parameter sets are (i.e. combinations of parameters that can produce similar neural activity or behavior), and how these structures relate to the function of neurons and neural circuits.

One candidate structure is a linear correlation between the densities of two ion channels, a phenomenon called ion channel correlation. In the pyloric circuit of the crab *Cancer borealis*, several ion channel correlations have been identified and found to maintain the rhythm. For example, a hyperpolarization-activated cation current (I_h) and a fast-inactivating potassium current (I_A) are coupled to maintain spiking frequency in the pyloric dilator (PD) neuron (Zhao and Golowasch, 2012) (Fig 1.2A). Covarying a fast sodium current (I_{Na}) and a transient calcium current (I_{CaT}) maintains spike phase patterns in a PD neuron model (Soofi et al., 2012). Ion channel correlations have also been observed in mouse hippocampal and cholinergic basal forebrain neurons as well as in the neuromuscular junction in *Drosophila*, yet it is unclear whether and how they help to maintain neural activities (Bergquist et al., 2010; Tran et al., 2019).

On the other hand, when we examine correlations of all pairs of ion channel densities in a neuron or neural circuit, most pairs show weak to no correlation (Achard and De Schutter, 2006; Taylor et al., 2009; Anirudhan and Narayanan, 2015). In a PD neuron model, different combinations of a calcium-dependent potassium current (I_{KCa}) and a calcium current (I_{Ca}) lead to different types of neural activities, such as silence, tonic spiking, and repetitive bursting, etc. Combinations of parameter values that lead to similar neural activities usually form a continuous region in parameter space, but degenerate solutions in each region show weak to no linear correlations (Bialek, 2012; LeMasson et al., 1993) (Fig 1.2B).

Linear correlations between ion channel densities have been observed in both invertebrates and vertebrates (Khorkova and Golowasch, 2007; Ransdell et al., 2012; Temporal et al., 2012; Tran et al., 2019), and are found to maintain neural activities (MacLean et al., 2005; Grashow et al., 2010; Zhao and Golowasch, 2012). We therefore wonder what are the factors that influence the strength of linear structures in degenerate parameter sets and how do the linear structures relate to the functions of neurons and neural circuits.

We investigated this question by combining a physiologically-realistic model of the pyloric circuit in the crab *Cancer borealis* with a multi-objective evolutionary algorithm that enabled us to find a collection of degenerate parameter sets that can produce pyloric rhythms mimicking those observed *in vitro* (Prinz, 2010a; Fortin and Parizeau, 2013). We then imposed two types of constraints on this approach to see how each constraint shapes and changes the structures of degenerate parameter sets, as follows. Our results show that constraining the degenerate parameter sets by reducing the variability of pyloric rhythm features from +/- 2 std to +/- 1 std (i.e. standard deviation) increases the overall strength of linear correlations in the degenerate parameter sets, while constraining the parameter sets by reducing the number of parameters does not. Together, this suggests that output variability is one of the factors that influences the strength of linear structures in degenerate parameter sets. The more constrained the output variability is, the stronger the overall linear structures of degenerate solutions are.

2.1.2 Overview of the pyloric circuit in the crab *Cancer borealis*

The stomatogastric nervous system (STNS) of the crab *Cancer borealis* is a part of the crustacean nervous system and contains four ganglia and their connecting nerves. One of the ganglia is the stomatogastric ganglion (STG), which contains two distinct but interconnected central pattern generators (CPGs) that generate rhythms regulating gastric mill (chewing) and pylorus (filtering of chewed food) movements (Fig 2.1A). A set of neurons in the STG comprises the pyloric circuit, which generates the pyloric rhythm that controls the movement of the pylorus. This set of neurons includes one anterior burster (AB), two pyloric dilator (PD), one lateral pyloric (LP), four to six pyloric constrictor (PY), one inferior cardiac (IC), and one ventricular dilator (VD) neurons (Harris-Warrick, 1992). The IC neuron often fires together with the LP neuron, and the VD neuron fires synchronously with the PY neurons. AB is an interneuron and is electrically coupled to the PD neurons, while the rest are motor neurons that innervate muscles to control food filtering. To simplify the simulation, functionally equivalent neurons are combined together in our circuit model. Therefore, the electrically coupled AB and PD neurons are merged into one pacemaker neuron, and the IC and VD neurons are not included in the model (Fig 2.1B).

Neurons in the pyloric circuit are connected to each other through glutamatergic and cholinergic synapses, which are both inhibitory. The glutamatergic synapses are chloride-mediated and rapid (Hartline and Gassie, 1979; Eisen and Marder, 1982), while the cholinergic synapses are potassium-mediated and slow (Eisen and Marder, 1982; Marder and Eisen, 1984).

The AB neuron is usually the fastest oscillator neuron in the network, which drives the electrically coupled PD neurons to fire with it. The pacemaker formed by AB and PD neurons is bursting endogenously, while LP and PY neurons are intrinsically tonic spiking or silent. When the AB/PD pacemaker kernel fires a burst of action potentials and inhibits the LP and PY neurons, LP neuron bursts with a delay due to plateau potentials triggered by post-inhibitory rebound, followed by the PY neurons, whose cellular properties delay their post-inhibitory rebound bursting. Together, the pyloric rhythm generates a tri-phasic pattern in the order of AB/PD-LP-PY with a period of ~1-2s, as shown in Fig 2.1C.

The pyloric rhythm in the crab *Cancer borealis* is maintained by homeostatic plasticity mechanisms. The rhythm ceases when descending neuromodulatory inputs are acutely removed, a process called deafferentation, but can recover 3-4 days later in the absence of neuromodulatory inputs (Thoby-Brisson and Simmers, 1998; Golowasch et al., 1999; Luther et al., 2003) (Fig 2.1D). Most of the descending neuropeptides activate the same modulator-activated inward current (I_{MI}) found in all pyloric circuit neurons, and different types of pyloric circuit neurons receive a different subset of neuropeptides (Swensen and Marder, 2000; Daur et al., 2016) (Fig 2.1E). Each neuropeptide has a different effect on the cellular dynamics. For example, the neuropeptide proctolin elicits an inward current and has a reversal potential around 0 mV (Golowasch and Marder, 1992). It strongly excites the LP and IC neurons, causing them to fire extended high-frequency bursts of action potentials (Hooper and Marder, 1987).

The STG is an ideal system to study the structures of degenerate parameter sets for several reasons. First, its relatively large and well-identified neurons and synaptic connections allow electrophysiology recordings and conductance-based modeling. Second, the rhythmic output is stereotypical so any changes of this behavior due to pharmacological manipulation or other perturbations are easy to quantify. Moreover, the pyloric rhythm is maintained by homeostatic plasticity mechanisms, enabling us to examine how degenerate parameter sets contribute to the rhythm recovery after perturbation.

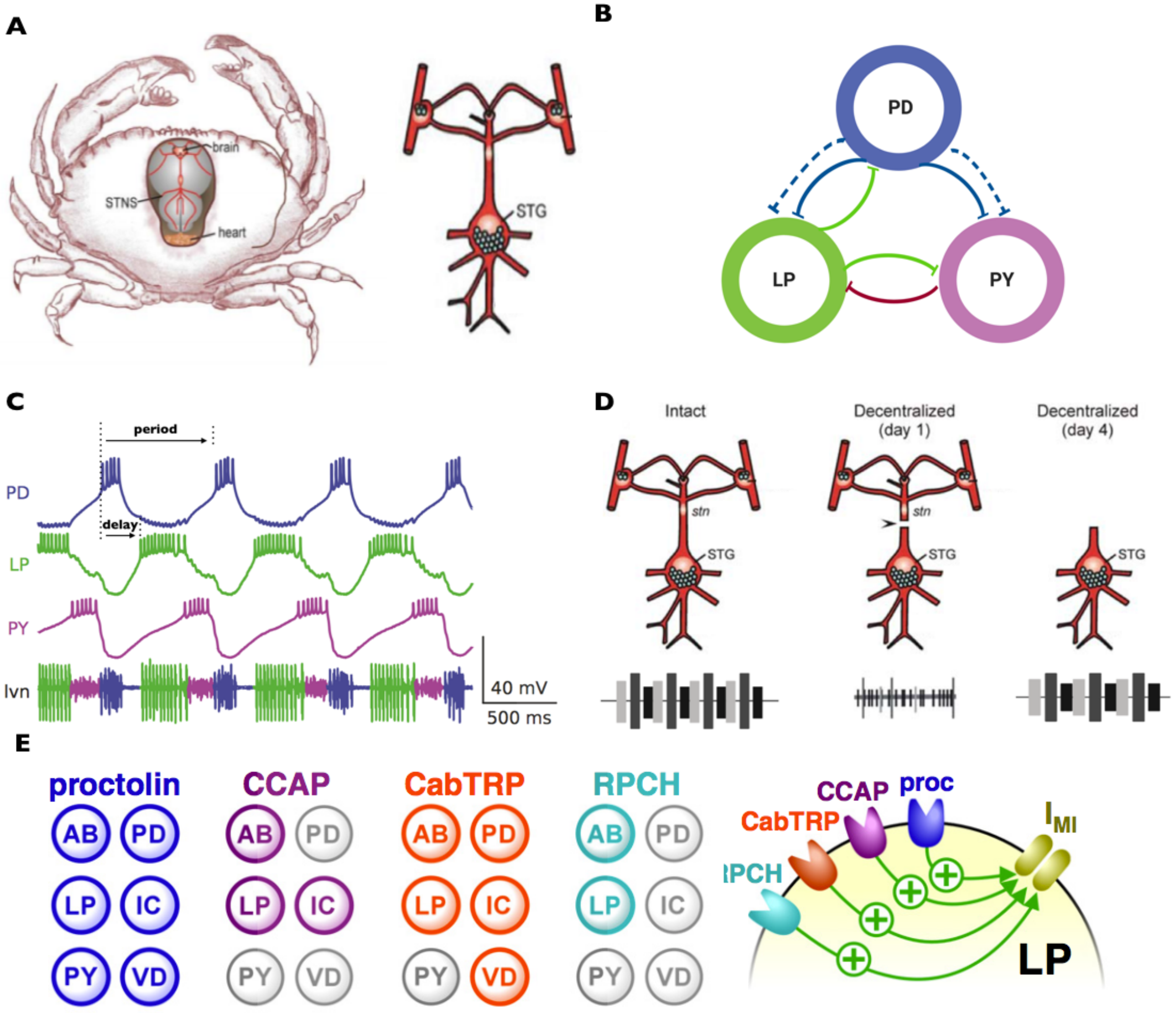

Figure 2.1 Overview of the pyloric circuit in the crab *Cancer borealis*. (A) Dorsal view of the crab *Cancer borealis* with parts of its dorsal carapace removed. The stomatogastric ganglion (STG) resides in the stomatogastric nervous system (STNS). Figure is adapted with permission from Stein, 2009. **(B)** Schematic diagram of the pyloric circuit without the AB, VC, and IC neurons. PD neuron (blue) represents the AB/PD pacemaker kernel and is intrinsically bursting, and sends both glutamatergic (solid line) and cholinergic (dashed line) inputs to LP neuron (green) and PY neuron (purple). **(C)** The pyloric rhythm *in vitro*. Bottom: Extracellular recording from *lvn* shows the triphasic rhythm of the pyloric circuit in the order of PD-LP-PY. Top: Intracellular recording from each type of neuron shows their bursting patterns. Pyloric period is defined as the interval between the onset of two PD bursts, and delay is the interval between the onset of a PD burst and the onset or offset of the following bursts in the pyloric period. Figure is adapted from Kispersky et al., 2011. **(D)** Schematics showing the pyloric rhythm recovery after deafferentation. Left: With intact neuromodulatory input from the CoG projection neurons, the pyloric CPG generates a rapid triphasic pattern (bottom). Middle: When the stomatogastric nerve (*stn*) is transected, a process called deafferentation, the pyloric rhythm stops and most pyloric neurons generate tonic activity (bottom). Right: The pyloric rhythm recovers 4 days after deafferentation in the absence of neuromodulation. Figure is adapted

with permission from Stein, 2009. **(E)** Different neuropeptides all converge on I_{MI}, but different cell types respond to a different subset of neuropeptides. RPCH: red pigment concentrating hormone; CabTRP: *Cancer borealis* tachykinin-related peptide; CCAP: crustacean cardioactive peptide; proc: proctolin. Responsive neurons shown in color, non-responsive neurons in grey. Figure is adapted with permission from Daur et al., 2016.

2.2 Methods

2.2.1 Pyloric circuit model

A conductance-based model of the pyloric circuit was built upon a previous model (Prinz et al., 2004), which consists of eight types of membrane currents for each neuron shown in Fig 2.2A (a fast sodium current, I_{Na}; a fast and slow transient calcium current, I_{CaT} and I_{CaS}; a delayed rectifier potassium current, I_{Kd}; a calcium-dependent potassium current, I_{KCa}; a fast transient potassium current, I_A; a hyperpolarization-activated inward current, I_h; a voltage-independent leak current, I_{leak}), and two types of inhibitory synaptic currents (a fast glutamate-dependent current, I_{Glu}, and a slow cholinergic-dependent current, I_{ACh}). A modulator-activated inward current, I_{MI}, was also added to each neuron (Zhang and Golowasch, 2011). Deafferentation of the pyloric circuit was simulated by setting the maximum conductance of I_{MI} in each neuron to zero. The kinetic parameters of the membrane currents are based on recordings from lobster STG neurons and are identical for all model neurons (Turrigiano et al., 1995).

The membrane voltage, V, is updated according to the equation:

$$C_m \frac{dV}{dt} = -\sum I_i - I_{input} \tag{2.1}$$

Each current, I_i, is described by the equation:

$$I_i = G_i m^p h^q (V - E_i) \tag{2.2}$$

where G_i is the maximal conductance, E_i is the reversal potential, m and h are gating variables for activation and inactivation, and p and q are integer exponents. The reversal potentials for the various membrane currents are: 50mV for I_{Na}; -80 mV for I_{Kd}, I_{KCa}, and I_A; -20 mV for I_h; -50 mV for I_{leak}; and -10 mV for I_{MI}. The reversal potential for I_{CaT} and I_{CaS} is calculated by:

$$E_{Ca} = \frac{R \cdot T}{Z_{Ca} \cdot F} \log \frac{[Ca^{2+}]_{out}}{[Ca^{2+}]} \tag{2.3}$$

where R = 8.31 $J/(mol \cdot K)$, T = 283 K, Z_{Ca} = 2, F = 96485 C/mol, and $[Ca^{2+}]_{out} = 3\ mM$.

The activation and inactivation variables m and h are updated by the equation:

$$\frac{dx}{dt} = \frac{x_\infty - x}{\tau_x} \tag{2.4}$$

The intracellular calcium concentration is updated by:

$$\tau_{Ca} \frac{d[Ca^{2+}]}{dt} = -\alpha(I_{CaS} + I_{CaT}) - [Ca^{2+}] + [Ca^{2+}]_0 \tag{2.5}$$

where τ = 200 ms is the Ca^{2+} buffering time constant, α = 14.96 $\mu M/nA$ is the conversion factor from current to concentration, and $[Ca^{2+}]_0$ = 0.05 μM is the steady-state intracellular Ca^{2+} concentration if no Ca^{2+} flows across the membrane (Prinz et al., 2003).

The synaptic current is calculated as:

$$I_{syn} = g_{syn}(V_{post} - E_{syn}) \tag{2.6}$$

where g_{syn} is the maximal synaptic conductance, V_{post} is the membrane potential of the postsynaptic neuron, and E_{syn} is the reversal potential of the synapse, which is -70 mV for glutamatergic synapses and -80 mV for cholinergic synapses (Prinz et al., 2004).

Detailed implementation of each membrane and synaptic current is included in Appendix 5.1.

2.2.2 Multi-objective evolutionary algorithm (MOEA)

To automate the construction of a set of heterogeneous pyloric circuit models of various ion channel densities and synaptic strengths that could all produce physiologically-realistic pyloric rhythms, we employed an ensemble modeling approach called multi-objective evolutionary algorithms (MOEA) (Prinz, 2010a; Fortin and Parizeau, 2013; Deb et al., 2002). MOEAs are automated parameter fitting algorithms that are suitable to models with many parameters and more than one objective to fit. Objectives can be features of neural activities such as firing rate, burst duration, etc. (Van Geit et al., 2008). The algorithm consists of two parts: multiple objective functions that measure whether the simulated output matches experimental data or other criteria defined by the user, and a search algorithm that finds combinations of parameters producing the targeted output. The 34 parameters in our model are the maximal conductances of ion channels and synaptic strengths, and the range of each parameter is indicated in Table 2.1.

We defined six objectives, which are the pyloric period and the on- and off-phase of each neuron in the pyloric circuit (Fig 2.1C). Phase relationships are measured by dividing the delay relative to the preceding PD burst start with which a neuron starts or ends bursting by the pyloric period, i.e. phase = delay / period. The targeted range for each objective was extracted from experimental data and the literature (Table 2.2) (Goaillard et al., 2009; Hudson et al., 2015). Instead of assigning a weight to each objective, all objectives were employed in parallel to compare pyloric rhythms from the simulation to those from experiments.

The specific MOEA used in this project is an improved version of nondominated sorting genetic algorithm II (NSGA II) from the Distributed Evolutionary Algorithms in Python (DEAP) Toolbox (Deb et al., 2002; Fortin and Parizeau, 2013) (version 1.0.2), which is inspired by the "survival of the fittest" principle of natural selection. NSGA II was chosen both because it can handle models with a large number of parameters and because it can generate a group of models that together represent both the mean and the variance of the experimental dataset (Druckmann et al., 2007).

Each run of NSGA II starts with a population of randomly initialized parameter sets, checks the fitness of each parameter set, and breeds the next generation of parameter sets by random mutation and cross-over of the fittest parameter sets. This process iterates until it reaches a certain number of generations, and all parameter sets in the last generation that can produce targeted pyloric rhythms are deemed qualified. Qualified parameter sets from each run range from 0 to the size of population, depending on the initial conditions. Together, all qualified parameter sets from all runs compose the dataset for certain predefined pyloric rhythms, where each parameter set produces a single instance of the pyloric rhythm observed *in vitro* and all parameter sets as a whole capture the variability of pyloric rhythms *in vitro*.

Fitness is based on how similar the simulated and biological pyloric rhythms are regarding each feature, and the similarity, s, is calculated by:

$$s = \begin{cases} 0, \ if\ f_{min} \le f_{model} \le f_{max} \\ \quad \left(\frac{f_{model} - f_{mean}}{f_{s.d.}}\right)^2 \end{cases} \tag{2.6}$$

where f_{model} is the feature value of the simulated pyloric rhythm, f_{mean} and $f_{s.d.}$ are the mean and standard deviation of each feature indicated in Table 2.2, and f_{min} and f_{max} are f_{mean} +/- 2 $f_{s.d.}$, respectively.

To avoid getting stuck in local optima, the algorithm ensures that all the qualified parameter sets are as dissimilar as possible and randomizes the initial search point for each run. Individual runs of NSGA II are independent of each other, and therefore can be parallelized to speed up the search. We parallelized the processing of NSGA II by running it on high-performance computing clusters with the following parameters: number of generations = 60, size of population = 252, crossover rate = 0.8, and mutation rate = 1 / 34. Size of population was determined by the Das and Dennis's systematic approach with M = 6 and p = 5 (Deb and Jain, 2014; Das and Dennis, 1998). The crossover and mutation rates were based on values commonly found in the literature. Specifically, the mutation rate was calculated by 1 / n, where n is the number of parameters in the model (Fortin and Parizeau, 2013). Number of generations was determined by incrementing from 10, 20,…, to 120 to find the optimal value that balances convergence rate with execution time.

To make sure that we had enough data for correlation analysis, a learning curve of a certain ion channel correlation (y-axis) and the number of parameter sets (x-axis) was plotted for both a strong ion channel correlation (i.e. between I_A and I_{CaS} in PD neuron) and a weak one (i.e. between I_A and I_{KCa} in PD neuron) (data not shown). We also calculated confidence intervals by bootstrapping (section 2.2.3.2) to further confirm that our datasets were representative.

2.2.3 Data analysis

2.2.3.1 Kernel density estimation

Kernel density estimation for visualization of parameter distributions was implemented based on the *KernelDensity* function from Python's scikit-learn Toolbox (version 0.20.1) with a Gaussian kernel and a bandwidth of the maximum value of each parameter shown in Table 2.1 divided by 15.

2.2.3.2 Bootstrap

Confidence intervals of the bar plots and histograms were bootstrapped using the *resample* function from Python's scikit-learn Toolbox with the following parameters: replace=True, and number of bootstraps = 1,000. Confidence interval of the regression lines was automatically computed by Python's Seaborn Toolbox (version 0.9.0).

2.2.3.3 Pearson's correlation coefficient and correlation matrix

Pearson's correlation coefficient was computed by the *pearsonr* function from Python's SciPy Toolbox (version 1.2.1), and the correlation matrix was plotted using *matshow* function from Python's Matplotlib Toolbox (version 2.2.4).

2.2.3.4 Principal component analysis

Parameter sets were standardized using the *StandardScaler* function from Python's scikit-learn Toolbox, and their principal components and the corresponding eigenvalues were computed using the *PCA* function from Python's scikit-learn Toolbox.

2.2.4 Implementation and code accessibility

Simulation and analysis scripts were written in Python 2.7.12 and executed in PyCharm (CE 2017.1.2) on macOS 10.12.3 with a 1.7-GHz processor. Automated parameter fitting was parallelized by the SCOOP module (version 0.7.1.1) and run on the Neuroscience Gateway Portal (Sivagnanam et al., 2013). Differential equations were numerically integrated using the Exponential Euler method with a time step of 0.05 ms (Dayan & Abbott, 2001). Python code of simulation and data analysis is available at https://github.com/pinewave/pyloric-circuit-model.

Table 2.1 Range of maximal conductances of base pyloric circuit model

Type	Maximal conductance	Minimum (nS)	Maximum (nS)
PD	G_{Na}	1	400
	G_{CaT}	0.01	5
	G_{CaS}	0.01	8
	G_A	1	100
	G_{KCa}	0.1	10
	G_{Kd}	1	200
	G_h	1e-4	0.02
	G_{leak}	1e-3	0.02
	G_{MI}	1e-3	0.5
LP	G_{Na}	1	200
	G_{CaT}	0.01	5
	G_{CaS}	0.1	12
	G_A	0.1	60
	G_{KCa}	01.	10
	G_{Kd}	1	100
	G_h	1e-3	0.1
	G_{leak}	1e-4	0.04
	G_{MI}	1e-3	0.5
PY	G_{Na}	1	600
	G_{CaT}	0.01	5
	G_{CaS}	0.01	4
	G_A	1	100
	G_{KCa}	0.1	10
	G_{Kd}	1	224
	G_h	1e-4	0.08
	G_{leak}	1e-4	0.04
	G_{MI}	1e-3	0.5
Synaptic	PD to LP, G_{Glu}	1e-6	2e-4
	PD to LP, G_{ACh}	1e-6	2e-4
	LP to PD, G_{Glu}	1e-6	2e-4
	LP to PY, G_{Glu}	1e-6	2e-4
	PD to PY, G_{Glu}	1e-6	2e-4
	PD to PY, G_{ACh}	1e-6	2e-4
	PY to LP, G_{Glu}	1e-6	2e-4

Table 2.2 Experimental ranges of pyloric rhythm features

FEATURE	CONTROL		RECOVERY	
	Mean	**S.D.**	**Mean**	**S.D.**
PD off	0.2	0.02	0.175	0.02
LP on	0.38	0.05	0.4	0.05
LP off	0.7	0.05	0.6	0.05
PY on	0.68	0.05	0.62	0.05
PY off	0.99	0.015	0.95	0.015
Period (s)	0.9	0.17	1.89	0.59

2.3 Results

2.3.1 Computational approach

The pyloric circuit model contains 34 parameters, which are the maximal conductance of nine types of membrane currents observed in each neuron (Fig 2.2A) and the strength of the seven inhibitory synapses between neurons. Together all parameters compose the parameter space (Fig 2.2B). Each parameter can vary independently, and a set of values for each parameter composes a parameter set. The neural output generated by the circuit model with a given parameter set can be unrealistic (e.g. silent or tonic spiking) or realistic (e.g. physiologically-realistic pyloric rhythm).

To filter out the parameter sets that produce unrealistic neural outputs, we first need to define features of a physiologically-realistic pyloric rhythm. Pyloric rhythms *in vitro* can be characterized by various features, such as the pyloric period, burst duration, spikes per burst, etc. Studies show that phase relationships, defined as the onset or offset of a burst divided by the pyloric period, were maintained after various perturbations (Thoby-Brisson and Simmers, 1998; Luther et al., 2003), implying that they are important for the function of the pyloric rhythm in food filtering through appropriately timed activation of crab stomach muscles. We therefore characterized physiologically-realistic pyloric rhythms by the on- or off-phase of each neuron and the pyloric period. Although the pyloric rhythm is highly stereotypical, it still exhibits natural variability *in vitro*. We deemed a parameter set realistic if the phase relationships and the pyloric period of its simulated rhythm fell within the natural range of variability observed in experiments (Goaillard et al., 2009). The five phase relationships (i.e. off-phase of PD, on- and off-phase of LP, and on- and off-phase of PY) and the pyloric period comprise the output space, and natural variability of all features defines a targeted region in the output space (Fig 2.2B). Other features of the pyloric rhythms such as spike peak amplitude, burst duration, etc. were not considered both because their function in food filtering is unclear and because fewer objectives lead to better performance of the algorithm.

All parameter sets that can produce pyloric rhythms that fall within the targeted region are called degenerate parameter sets. To collect a group of degenerate parameter sets for different targeted regions, we employed a parameter fitting method called NSGA II. Given a pre-defined range for each parameter in the pyloric circuit model (Table 2.1) and a set of pyloric rhythm features (Table 2.2), NSGA II can find sets of parameter values producing pyloric rhythms that fall within the targeted region (Fig 2.3B). Fig 2.2C and 2.2D show two degenerate parameter sets that produce pyloric rhythms mimicking those seen before and after I_{MI} removal via deafferentation *in vitro*, respectively.

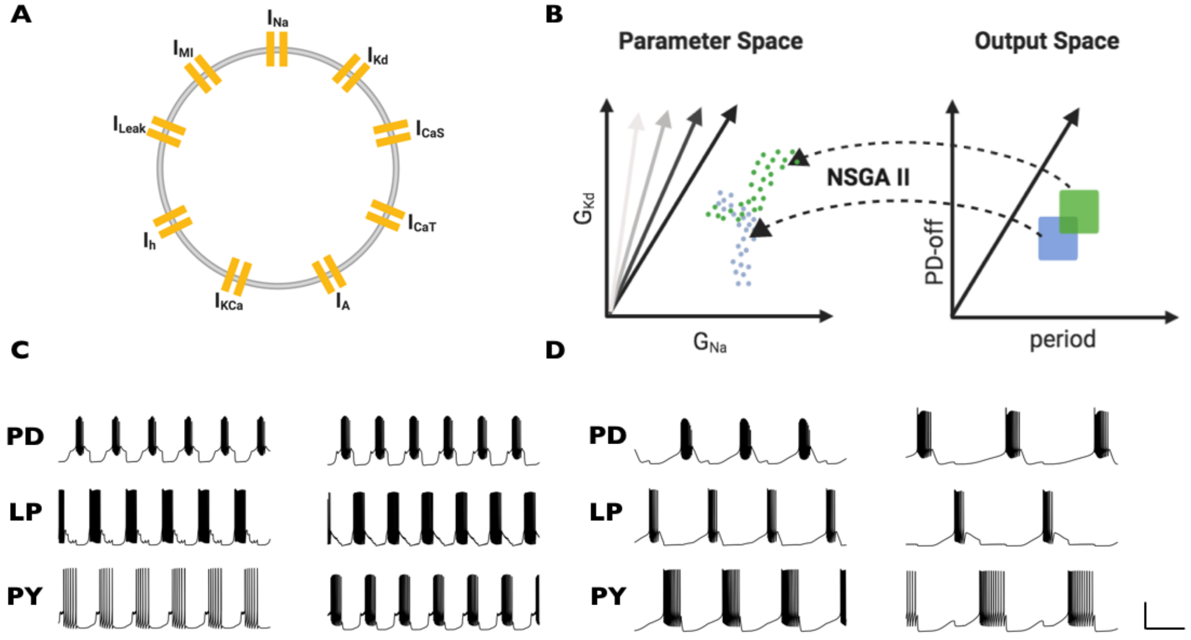

Figure 2.2 Overview of the computational approach. **(A)** A schematic diagram showing the conductance-based pyloric neuron model. Each type of pyloric neuron contains nine types of ionic currents as shown in the figure (see Methods). **(B)** A schematic diagram showing how the NSGA II algorithm works. The parameter space consists of 34 dimensions, with each dimension represented by one type of cellular or synaptic conductance in the pyloric circuit model. Salient features of the pyloric rhythm such as the pyloric period and phase relationships (i.e. PD-off, LP-on, LP-off, PY-on, PY-off phases) comprise the 6-dimensional output space. Each dot in the parameter space represents one parameter set that can produce a physiologically-realistic pyloric rhythm, which is defined by the box in the output space. Blue: before I_{MI} removal. Green: after I_{MI} removal. **(C)** Voltage traces of two parameter sets producing realistic pyloric rhythms as seen under control conditions, i.e., before I_{MI} removal. **(D)** Voltage traces of two parameter sets producing realistic pyloric rhythms as seen 4 days after deafferentation, i.e. after I_{MI} removal. Scale bar in C and D: 1s, 15mV.

2.3.2 Cellular and synaptic parameters before and after I_{MI} removal

Employing the computational approach depicted above, we collected a group of parameter sets that can produce pyloric rhythms seen before and after I_{MI} removal, respectively. Compared to pyloric rhythms before I_{MI} removal, those after I_{MI} removal differ in both the absence of I_{MI} and the ranges of features characterizing the rhythms (Table 2.2). Specifically, pyloric rhythms after I_{MI} removal have similar phase relationships but approximately double the length of pyloric period. Therefore, to tease apart whether differences between cellular and synaptic conductances before and after deafferentation are due to I_{MI} removal or due to different ranges of features, we collected a third group of degenerate parameter sets that does not have I_{MI} but produces pyloric rhythms matching those seen at control conditions. This group of parameter sets also serves as an ideal scenario where pyloric rhythms recover to exactly what they were before I_{MI} removal. Fig 2.3A illustrates the difference among the three groups of parameter sets, which are referred to as Control (n = 4,785), Recovery (ideal) (n = 4,352), and Recovery (real) (n = 3,554) datasets.

To determine whether and how each cellular and synaptic parameter changes in response to I_{MI} removal, we plotted the distribution of each parameter from each of the three groups of parameter sets. We observed that the overall strength of each parameter, measured by the median of its distribution, either increased, decreased or stayed relatively unchanged after I_{MI} removal, and examples of each scenario are shown in Fig 2.3B.

To elucidate trends of parameter changes in response to I_{MI} removal, for each parameter, we calculated the difference of the median from the Recovery (ideal) and Recovery (real) parameter sets minus the median from the Control parameter sets, respectively (Fig 2.3C and 2.3D), and divided each difference by the maximum range of each parameter shown in Table 2.1 to normalize it. We then organized the values by neuron types (i.e. PD, LP, PY) and synapses to ease the interpretation.

We observed that parameter changes are quite similar from Control to Recovery (ideal) and from Control to Recovery (real), indicating that most of the parameter changes are caused by I_{MI} removal instead of different ranges of pyloric rhythm features. Specifically, in all neurons, total calcium currents (i.e. G_{CaS} and G_{CaT}) and the calcium-dependent potassium current (i.e. G_{KCa}) were well preserved after I_{MI} removal, indicating that they are insensitive to I_{MI} removal. The A-type potassium current (G_A) and the leak current (G_{leak}) in general decreased after I_{MI} removal, which makes the neurons more excitable. On the other hand, the sodium current (G_{Na}), the delayed-rectifier potassium current (G_{Kd}), and the hyperpolarization-activated inward current (G_h) in general increased in all neurons after I_{MI} removal. The changes of synaptic strengths are also quite consistent between Recovery (ideal) and Recovery (real) datasets. In general, after I_{MI} removal, the strengths of all the fast, glutamatergic synapses decreased, while the strengths of all the slow, cholinergic synapses stayed relatively unchanged. Together, except for the change of G_{Kd}, all the other cellular and synaptic parameter changes compensated for the reduced excitation in the pyloric circuit caused by I_{MI} removal.

We do realize that the median of the distribution does not reflect all the changes that occurred after I_{MI} removal. For example, some of the parameters exhibit bi-modal or multi-modal distribution, as shown in Fig 2.3B and in Appendix 5.3. How the modality changes of the parameter distributions relate to I_{MI} removal is unclear.

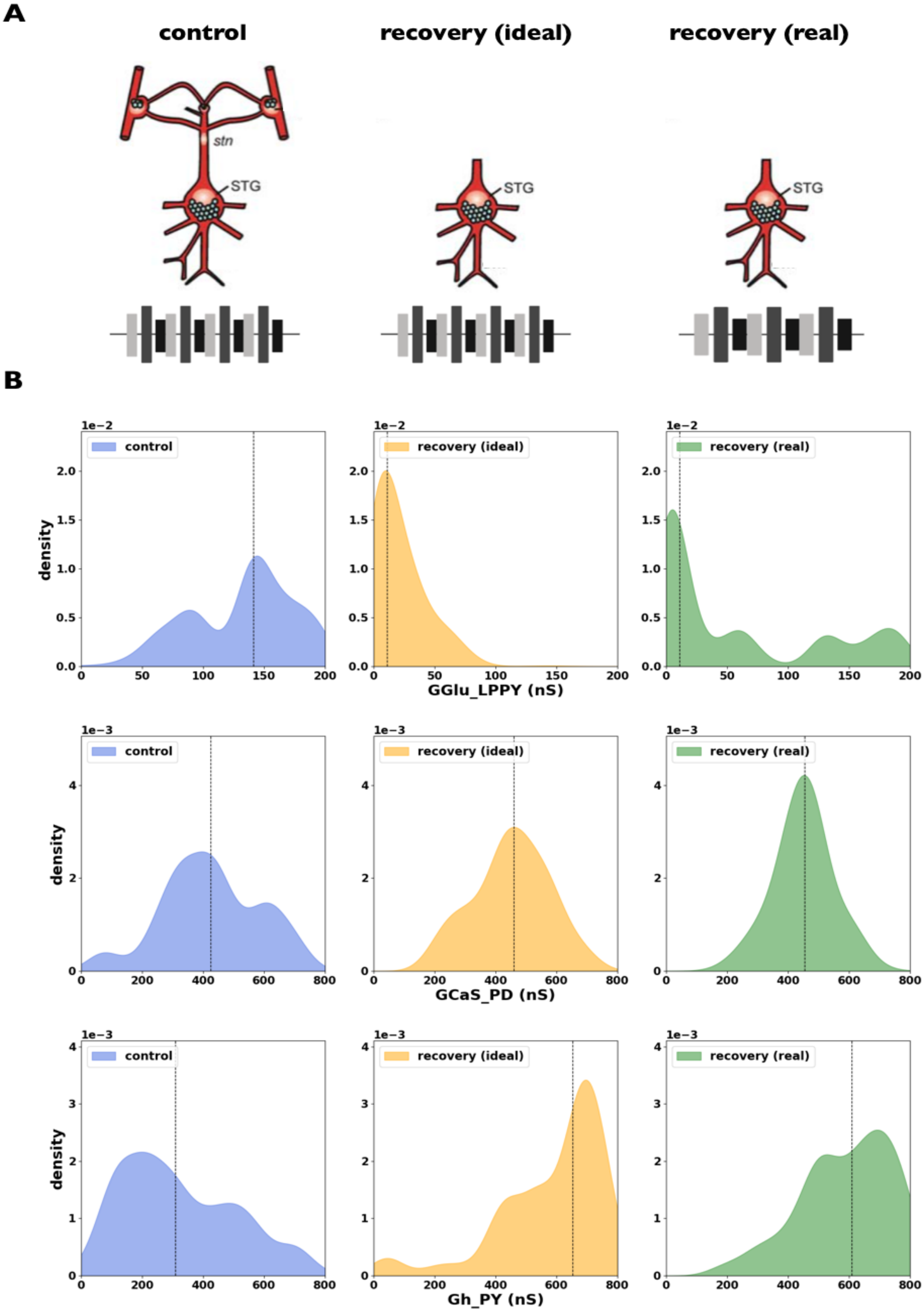
A
control
recovery (ideal)
recovery (real)
stn
STG
STG
STG
B
1e−2
control
recovery (ideal)
recovery (real)
density
0.0
0.5
1.0
1.5
2.0
0
50
100
150
200
GGlu_LPPY (nS)
1e−3
0
2
4
200
400
600
800
GCaS_PD (nS)
1e−3
0
1
2
3
4
Gh_PY (nS)

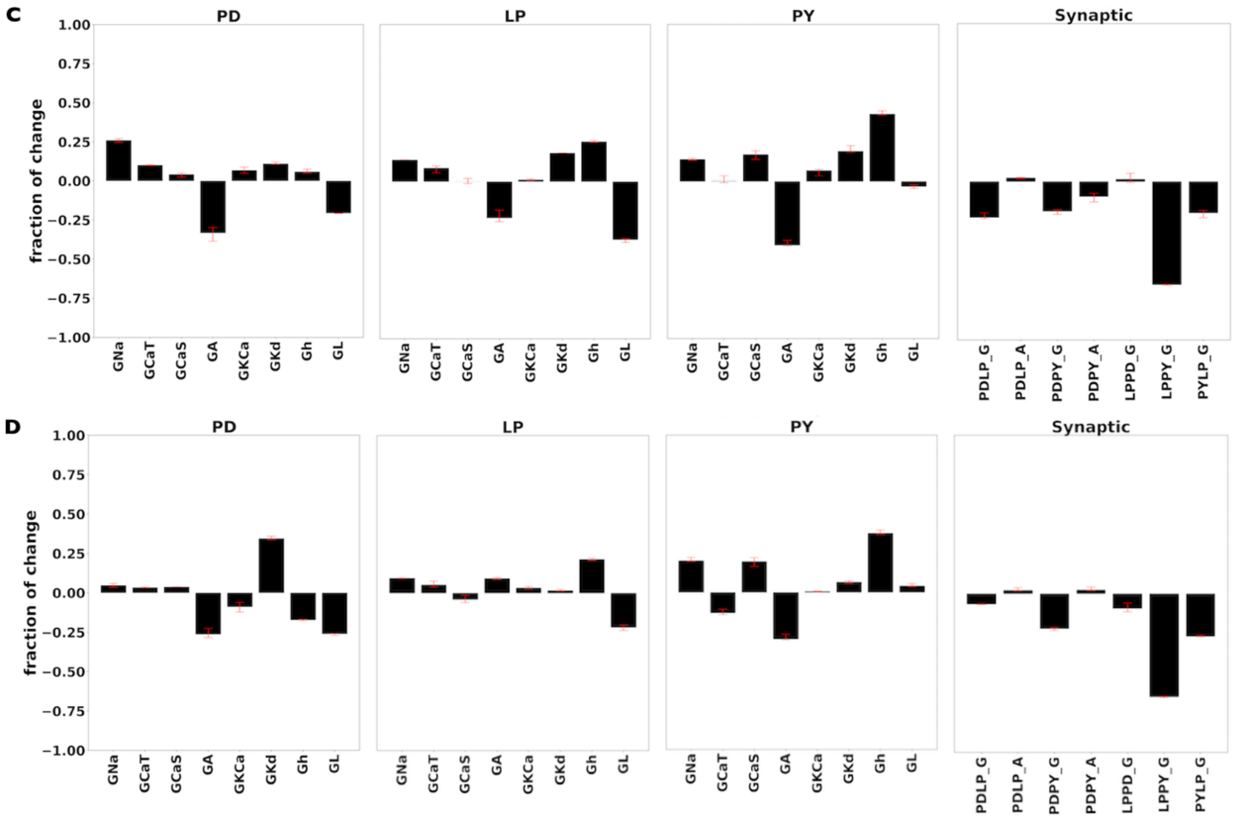

Figure 2.3 Cellular and synaptic parameters before and after I_{MI} removal. (A) A schematic diagram illustrating the three different parameter sets. *Left:* "Control" parameter sets receive neuromodulatory inputs and produce rhythms as seen under control conditions. *Middle:* "Recovery (ideal)" parameter sets receive no neuromodulatory inputs and produce rhythms as seen under control conditions. *Right:* "Recovery (real)" parameter sets receive no neuromodulatory inputs and produce rhythms as seen 4 days after deafferentation. **(B)** Distribution of three cellular or synaptic parameters from each group of parameter sets. Distributions are smoothed by kernel density estimation. Top row: Compared to control, strength of the glutamatergic synapse from LP to PY was reduced after I_{MI} removal. Middle row: Compared to control, density of I_{CaS} in PD neuron stayed relatively unchanged after I_{MI} removal. Bottom row: Compared to control, density of I_h in PY neuron increased after I_{MI} removal. Blue: Control. Yellow: Recovery (ideal). Green: Recovery (real). Dotted vertical line: median of the distribution. **(C)** Difference of the median from the "Recovery (ideal)" parameter sets minus the median from the "Control" parameter sets for each parameter in Table 2.1 (except I_{MI}). Red line: bootstrapped 90% confidence interval. **(D)** Difference of the median from the "Recovery (real)" parameter sets minus the median from the "Control" parameter sets for each parameter in Table 2.1 (except I_{MI}). Red line: bootstrapped 90% confidence interval.

2.3.3 Ion channel correlations before and after I_{MI} removal

Removal of I_{MI} from the pyloric circuit model resembles deafferentation *in vitro*, and reduces the number of parameters from 34 to 31. To see how the linear structures of degenerate parameter sets change after I_{MI} removal, we measured ion channel correlations by Pearson's correlation coefficient and visualized them by plotting the correlation matrix (Fig 2.4A). In the Control datasets, the strongest ion channel correlation is between G_{KCa} and G_{Kd} in the PD neuron, while in both the Recovery (ideal) and the Recovery (real) datasets, the strongest ion channel correlation is between G_{CaS} and G_A in the PD neuron. Scatter plots for G_{KCa} vs. G_K and for G_{CaS} vs. G_A are shown in Fig 2.4B.

To compare the overall changes of ion channel correlations before and after I_{MI} removal, we plotted the histogram of all ion channel correlation coefficient from each correlation matrix shown in Fig 2.4A. By comparing the histograms from the Control dataset vs. the Recovery (ideal) dataset, we saw that their histograms overlapped with each other, indicating similar overall strength of linear correlations (Fig 2.4C). Histograms from the Control dataset vs. the Recovery (real) dataset also overlapped with each other, indicating that targeting different ranges of features in addition to I_{MI} removal did not affect the overall strength of linear correlations (Fig 2.4D). Histograms in Fig 2.4C and Fig 2.4D also reveal that most of the ion channel correlations are weak or absent ($-0.6 < r < 0.6$), and that there are approximately equal amounts of positive and negative ion channel correlations.

To understand how the ion channel correlation between G_{CaS} and G_A forms after I_{MI} removal, we referred to the distributions of G_{CaS} and G_A in the PD neuron from each group of parameter sets in Fig 2.3, and found that the distribution of G_{CaS} in the PD neuron stayed relatively unchanged after I_{MI} removal (Fig 2.3B), while the overall strength of G_A in the PD neuron decreased (Appendix 5.3). This indicates that the strong ion channel correlation between G_{CaS} and G_A was accounted by change in the G_A distribution independent of the G_{CaS} distribution.

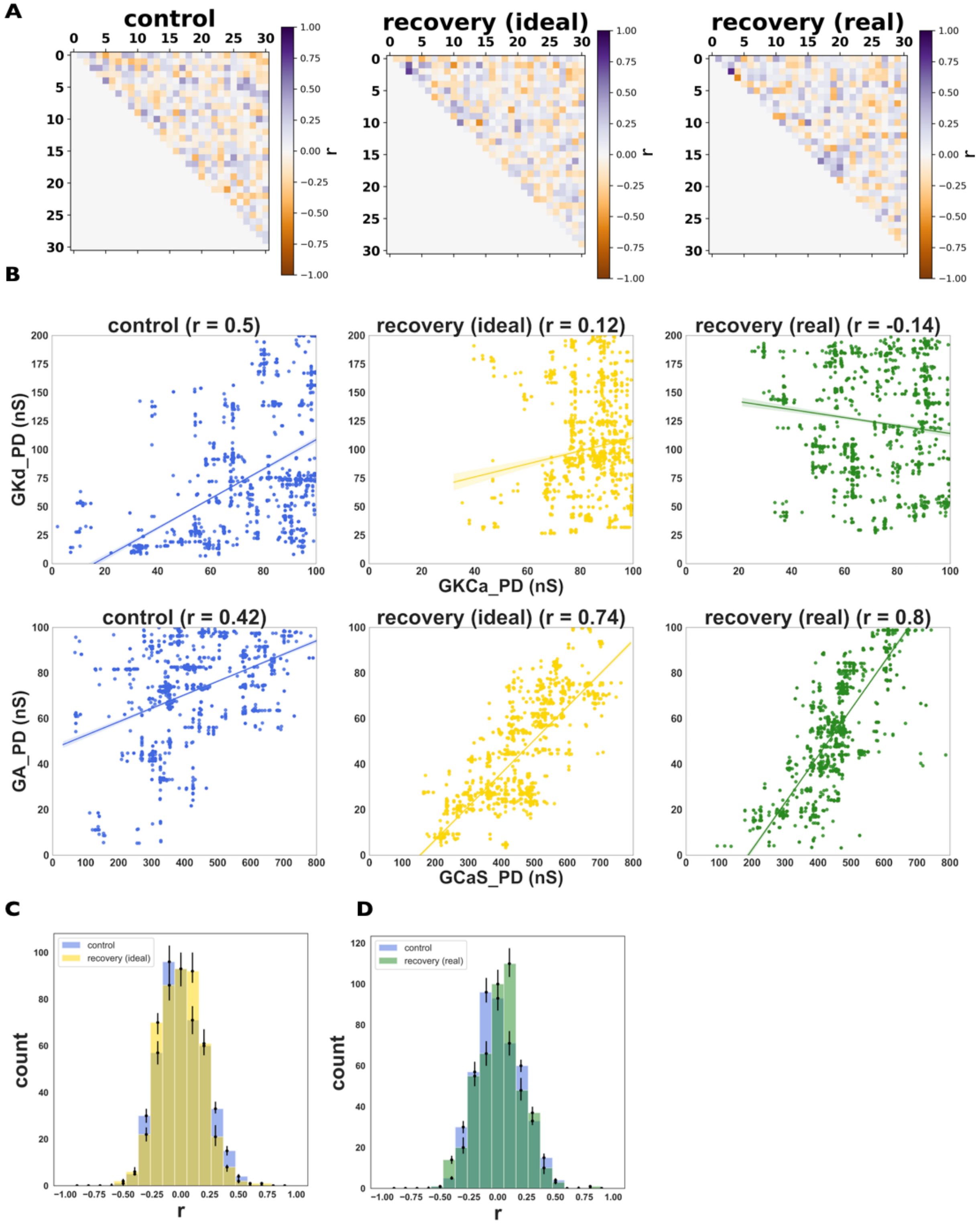

Figure 2.4 Ion channel correlations before and after I_{MI} removal. (A) Correlation matrix of all pairs of parameters from the “Control” parameter sets (left), the “Recovery (ideal)” parameter sets (middle), and the “Recovery (real)” parameter sets (right). Each correlation matrix contains 31

parameters, numbered from 0 to 30, which corresponds to the order of parameters in Table 2.1 (e.g. 0 is G_{Na} in PD, 1 is G_{CaT} in PD, etc.). All G_{MI} are not included. Correlations are measured by Pearson's correlation coefficient, and fall within the range of [-1, 1]. **(B)** Scatter plots of ion channel pairs from the "Control" parameter sets (blue), the "Recovery (ideal)" parameter sets (yellow), and the "Recovery (real)" parameter sets (green). Correlation value is included in the title, and the regression line is plotted with bootstrapped 95% confidence interval. Top row: The strongest ion channel correlation before I_{MI} removal and its corresponding distribution after I_{MI} removal. Bottom row: The strongest ion channel correlation observed after I_{MI} removal and its corresponding distribution before I_{MI} removal. (**C)** Histogram of all ion channel correlations from the "Control" (blue) versus the "Recovery (ideal)" parameter sets (yellow). Black bar: bootstrapped 95% confidence interval. **(D)** Histogram of all ion channel correlations from the "Control" (blue) versus the "Recovery (real)" parameter sets (green). Black bar: bootstrapped 95% confidence interval.

2.3.4 Ion channel correlations before and after reducing the variability of features

To relate ion channel correlations to functions of neurons and neural circuits, we wondered whether more tightly regulated neural activities are caused by stronger linear correlations of the underlying parameters. To investigate this, we reduced the variability of each rhythm feature for the Control dataset from +/- 2 std to +/- 1 std (Fig 2.5A, Top), and collected a group of degenerate parameter sets that produce pyloric rhythms satisfying the reduced variability of feature (n = 5,275). We then examined the correlation matrix for each dataset (Fig 2.5A, Bottom), and saw that the strongest positive and negative ion channel correlations after reducing the variability of the features were G_{CaS} vs G_A in the PD neuron and G_{leak} in the PY neuron vs. the glutamatergic synapses from PY to LP, respectively. Scatter plots of each pair before and after reducing the variability of the features are shown in Fig 2.5B.

To compare the overall changes of ion channel correlations before and after reducing the variability of features, we plotted the histogram of all ion channel correlations from each correlation matrix shown in Fig 2.5A, and found that reducing the variability of the features enhanced both positive and negative ion channel correlations in the degenerate parameter sets (Fig 2.5C).

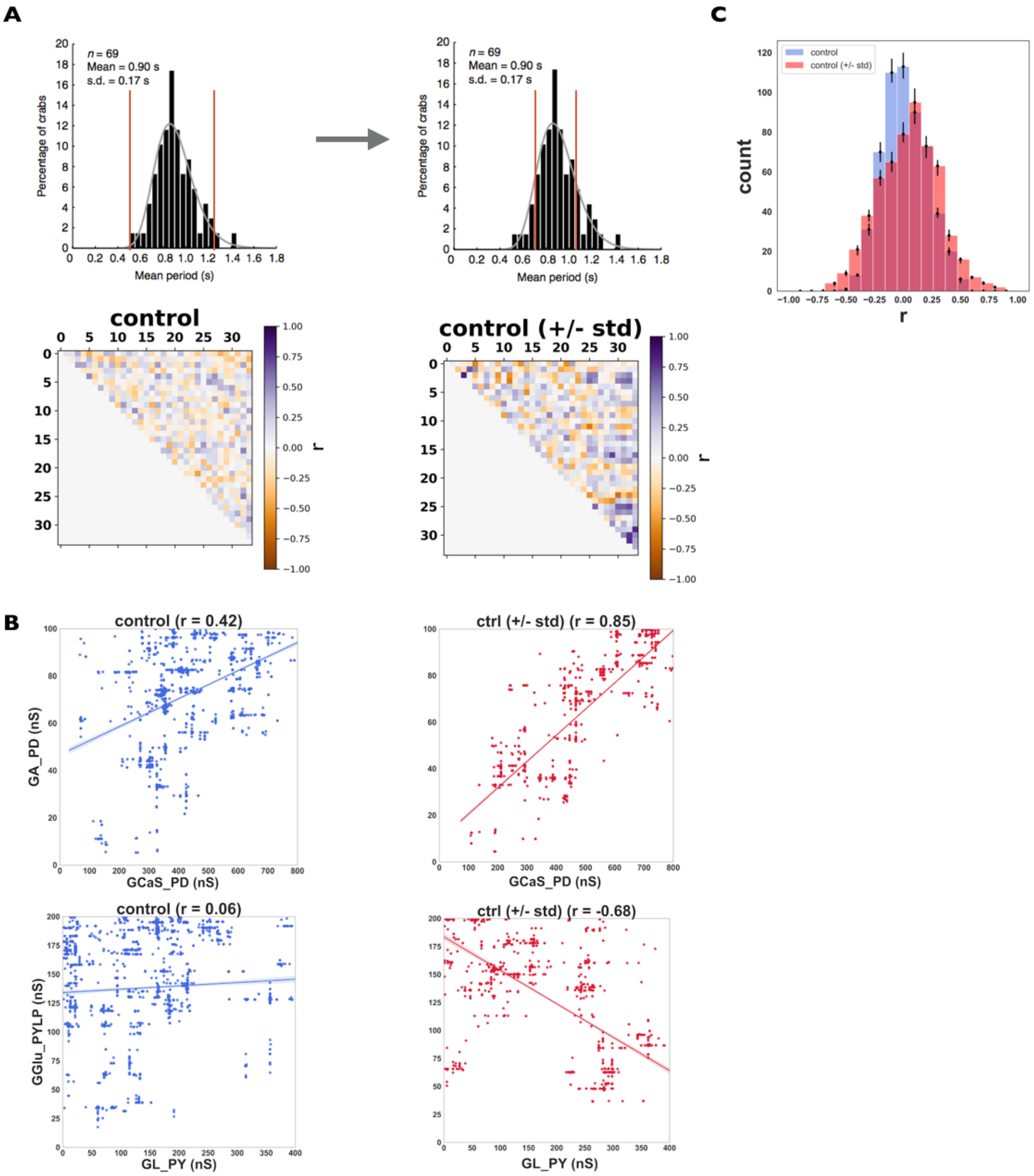

Figure 2.5 Ion channel correlations before and after reducing the variability of features. (A) Correlation matrix of all pairs of parameters from the "Control" (left) and the "Control (+/- 1 std)" parameter sets (right). Each correlation matrix contains 34 parameters, numbered from 0 to 33, which corresponds to the order of parameters in Table 2.1 (e.g. 0 is G_{Na} in PD, 1 is G_{CaT} in PD, etc.). Correlations are measured by Pearson's correlation coefficient, and fall within the range of [-1, 1]. Top row: A schematic diagram depicting the reduced variability of each feature from +/- 2 std to + / - 1 std, using the feature "period" as an example. Top row figure is adapted from Goaillard *et al.*, 2009. Bottom row: correlation matrix. **(B)** Scatter plots of ion channel correlations from the "Control"

(blue) and the “Control (+/- 1 std)” parameter sets (red). Correlation value is included in the title, and the regression line is plotted with bootstrapped 95% confidence interval. Top row: the strongest positive ion channel correlation found after reducing the variability of features (right) and its corresponding distribution before (left). Bottom row: the strongest negative ion channel correlation found after reducing the variability of features (right) and its corresponding distribution before variability reduction (left). **(C)** Histogram of all ion channel correlations from the “Control” (blue) versus the “Control (+/- 1 std)” parameter sets (red). Black bar: bootstrapped 95% confidence interval.

2.3.5 Principal component analysis

Pearson’s correlation coefficient is one way to measure linear structures of degenerate parameter sets. It assumes that the distribution of each parameter is Gaussian, which is not always the case, as evident for example in Fig 2.3B and Appendix 5.3. Therefore, we implemented another measure of linear structures of degenerate parameter sets called principal component analysis (PCA). For PCA, the fewer number of eigenvectors needed to explain the same amount of the total variance in a dataset, the stronger the linear structures are. We applied PCA to compare the Control and the Recovery (real) datasets, and found that they both needed 17 eigenvectors to explain 90% of the variance (Fig 2.6A). On the other hand, the Control dataset with reduced variability of features needed 13 eigenvectors to explain 90% of the variance (Fig 2.6B). To inspect whether our datasets contain spurious correlations, null model for each dataset was constructed by random shuffling of all values in each variable. We then performed PCA on each null model (Fig 2.6, dotted lines), and found no spurious correlations.

Together, these results are consistent with linear structures measured by Pearson’s correlation coefficient, and further confirms that reducing the variability of features, but not the number of parameters, leads to enhanced linear structures of degenerate parameter sets.

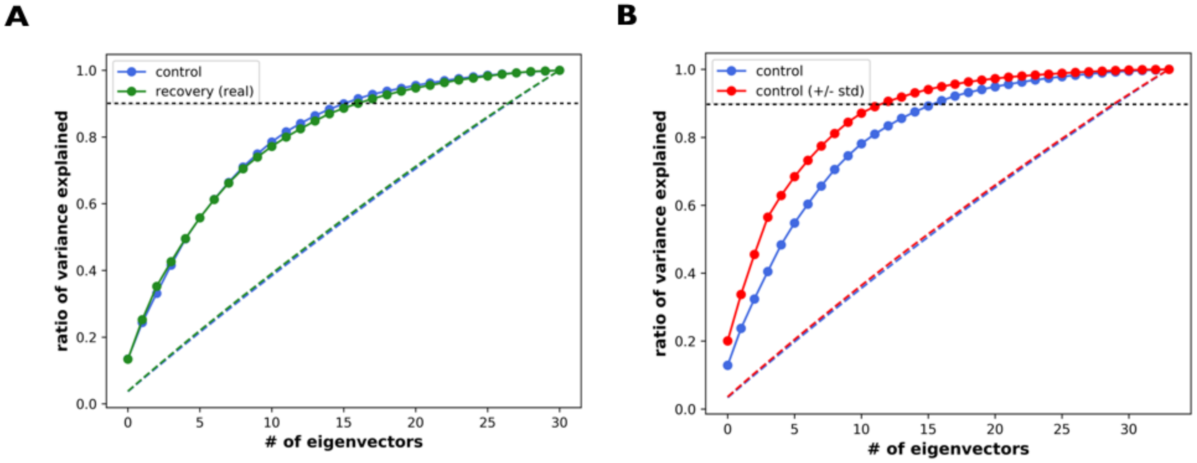

Figure 2.6 Characterizing linear structures by PCA (A) The number of eigenvectors needed to account for 90% of variance (indicated by the dotted black horizontal line) in the data is 17 for both "Control" (blue) and "Recovery (real)" (green) parameter sets. **(B)** The number of eigenvectors need to account for 90% of variance (indicated by the dotted black horizontal line) in the data is 17 for "Control" (blue) and 13 for "Control (+/- 1 std)" parameter sets (red). Dotted lines in color represent null model corresponding to each dataset.

2.4 Discussion

2.4.1 Summary of results

Experimental and computational studies across invertebrate and vertebrate neural systems and across scales have all revealed the presence of degenerate solutions, yet little is known about the structures of the degenerate solutions and how these structures relate to the function of neurons and neural circuits. By combining a pyloric circuit model with an ensemble modeling method, we collected a group of degenerate parameter sets that all produce similar pyloric rhythms. Employing this approach, we found that reducing the variability of objectives, but not the number of parameters, led to increased strength of linear structures of degenerate parameter sets. We also found that most possible pairs of ion channel correlations have weak or no linear correlations, which we think is a feature of degenerate systems. Last but not least, this approach enables us to examine and predict the concurrent changes of cellular and synaptic parameters after I_{MI} removal, which can be tested in experiments later.

2.4.2 How constraints shape structures of degenerate solutions

2.4.2.1 Constraint: Reducing the number of parameters

Removal of I_{MI} from the pyloric circuit model resembles deafferentation *in vitro*, and reduces the number of parameters from 34 to 31. I_{MI} has a reversal potential around 0 mV, and can elicit oscillatory activities in neurons. It is therefore anticipated that, to compensate for the reduced excitation that comes with the removal of I_{MI}, in general inward currents would increase and outward currents would decrease, which matches our results. We also found a significant reduction of I_{leak} in PD and LP neurons, which makes sense since reduced I_{leak} leads to increased time constant and therefore more excitable neurons. These changes overall matched the observations from the only deafferentation experiments conducted in the crab Cancer borealis that measured cellular properties , where the amplitude of I_h was significantly increased 4 days after deafferentation, while that of I_{Ca} and I_{KCa} was increased first but returned to control level 4 days after deafferentation (Khorkova and Golowasch, 2007). At the synaptic level, we found that the overall strength of all fast, glutamatergic synapses was reduced after I_{MI} removal, while that of all slow, cholinergic synapses was relatively unchanged. Given that removing I_{MI} decreased the overall excitation of the pyloric circuit, decreased strengths of these inhibitory synapses can be another mechanism to compensate for the reduced excitation.

We then measured the linear correlations of degenerate parameter sets before and after I_{MI} removal, and found that the overall strength of linear correlations were similar despite changes in individual pairs of correlations. One of the future directions is to remove other types of ion channels and see how this affects the linear correlations of degenerate parameter sets. For example, we saw a strong linear correlation between I_{CaS} and I_A in the PD neuron after I_{MI} removal, so we can remove either all I_{CaS} or all I_A from the pyloric circuit model and see how the overall strength of linear correlations changes.

2.4.2.2 Constraint: Reducing the variability of features

Neurons and neural circuits show variability across all scales, ranging from the genetic level to neural activities (Schulz et al., 2006; 2007; Goaillard et al., 2009; Wilhelm et al., 2009; Ayroles et al., 2015). Features of the pyloric rhythm in the crab *Cancer borealis*, such as pyloric period and phase relationships, also exhibit variability, and are referred to as objectives in our computational approach. By reducing the variability of objectives from +/- 2 std to +/- 1 std in the ranges of output features targeted by our parameter fitting algorithm, we observed increased strengths of linear correlations within degenerate parameter sets. Based on this result, we propose that one of the links between the two views of structures of degenerate parameter sets shown in Fig 1.2A and Fig 1.2B is the realization that the level of constraints imposed on the output variability affects the existence and tightness of linear correlations within degenerate parameter sets. At one extreme, for a tightly constrained output variability, maybe only one parameter set can produce the targeted neural activity. As we relax the constraints on variability, structures of parameter sets that can produce targeted neural activity may shift from strong linear correlations, to weak linear correlations, to regions divided by linear or nonlinear boundaries (Fig 2.7).

2.4.2.3 Another explanation for reproducibility issues in research

We are aware of the reproducibility issues in research, where researchers are unable to reproduce statistically significant findings in previously published works (Errington et al., 2014; Science2015, n.d.). Many factors contribute to the reproducibility issue. One of them was predicted by John Ioannidis, a physician from Stanford, who discussed the caveats of hypothesis testing that lead to high levels of false results in the context of modern science (Ioannidis, 2005). Based on our results, we think that another factor that might explain the issue is how constrained the output variability is. Neural activities measured from the same animal models in different labs may differ in their variability depending on many factors, such as animal source and husbandry, procedural details using the experiments, variations in chemical agents used, and experimenter skill, to name a few. Our result indicates that different output variability resulting from these factors may lead to different observations of linear correlations between the underlying parameters.

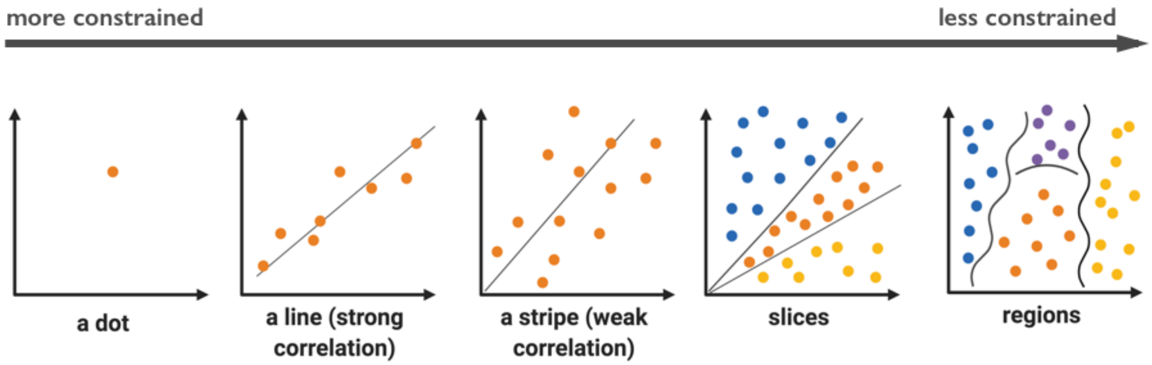

Figure 2.7 Structures of degenerate solutions and output variability. Each graph represents the parameter space of a neural system. Each dot represents one parameter set that can produce a targeted neural activity, with different colors representing different activities. Structures of degenerate parameter sets may widen from a dot (left, if output features are highly constrained) to regions divided by nonlinear boundaries (right, if constraints on output features are loose) as the output variability becomes less constrained.

2.4.3 Formation of ion channel correlations

2.4.3.1 Weak ion channel correlations and robustness

Conventionally, weak or absent ion channel correlations are interpreted as negative results and often not reported in publications. On the other hand, simulation studies of various invertebrate and vertebrate neurons and neural circuits have found that, when examining correlations between all possible pairs of ion channels, most of them are weak to absent (Achard and De Schutter, 2006; Taylor et al., 2006; Doloc-Mihu and Calabrese, 2014; Anirudhan and Narayanan, 2015). Here we propose that, from a system perspective, the prevalence of weak or absent ion channel correlations is a feature of degenerate systems and is important for robustness against perturbations. Unlike engineered systems operating under predictable conditions, living systems face uncertainties and constant changes in the environment and need to evolve a strategy to prepare for and recover from predictable and unpredictable perturbations. For example, one predictable perturbation is the change of temperature for creatures living in temperate zones (Caplan et al., 2014; Soofi et al., 2014; Haddad and Marder, 2018). A tightly regulated living system with a majority of strong linear correlations between its underlying parameters can function efficiently in a constant environment, but would be less robust to injuries and environmental perturbations. Degeneracy therefore could be a mechanism to cope with the tradeoff between efficiency and stability, enabling neurons and neural circuits to balance flexibility with stability to constantly adapt to the changing environment. The generally weak to absent linear correlations of degenerate solutions ensure flexibility, while a few strong ones ensure that neurons and neural circuits can encode information in a stable and efficient manner. We plotted the strength of each correlation before and after applying each type of constraint, and found no clear patterns of changes in correlation strength (Appendix, Fig 5.2), further confirms that weak ion channel correlations are loosely regulated in degenerate systems.

2.4.3.2 Weak ion channel correlations and sloppiness

The finding that ion channel correlations are generally weak or absent, with a few strong ones regulating neural activities, indicates a sloppy structure of the degenerate parameter sets. Sloppiness refers to the phenomenon that neural activities are sensitive to changes of parameters along a few "stiff" directions (i.e. strong ion channel correlations) and insensitive to changes of parameters along a large number of "sloppy" directions (i.e. weak ion channel correlations) (Daniels et al., 2008; Transtrum et al., 2015).

We observed that most ion channel correlations are weak or absent, and they appear or disappear when the degenerate parameter sets are constrained. It is challenging to relate the appearance and disappearance of each weak ion channel correlation to the constraints we imposed. In fact, we argue that the appearances and disappearances are more or less chaotic because those parameters reside on the sloppy dimensions, implying that they are loosely regulated and their changes do not affect neural activities of interest. As discussed above, this could be a strategy living systems evolved to balance flexibility with stability to adapt to constantly changing environments.

Analysis of sloppiness can be generalized and combined with experimental data to understand how populations of neurons maintain stable neural activity. For example, sloppiness analysis was applied to high-density multi-electrode recordings from cultured hippocampal neurons and revealed that firing rate was maintained at the population level while single neurons exhibited spontaneous firing rate fluctuations, which tend to occur along sloppy dimensions (Panas et al., 2015; Slomowitz et al., 2015).

2.4.3.3 Formation of strong ion channel correlations

The linear correlation between I_{CaS} and I_A became significantly stronger both after removing the neuromodulation-activated inward current and after reducing the variability of output features. This same correlation has also been observed in several variations of PD neuron models (Liu et al., 1998; Hudson and Prinz, 2010; O'Leary et al., 2013). In the Hudson *et al.,* 2010 model, the linear correlation between I_{CaS} and I_A was explained by independent variation of each ion channel density, which matches our result. The correlation between I_{CaS} and I_A in the Liu et al. 1998 model was regulated by an activity-dependent mechanism, where the rate of change of ion channel density is controlled by the instantaneous calcium concentration. These results indicate that the correlation between I_{CaS} and I_A can form either in an activity-dependent manner or by independent variation of ion channel densities.

2.4.3.4 Explanations for mismatches between experimental and computational findings

Certain strong ion channel correlations observed in experiments are absent in the model. For example, the correlation between I_A and I_h in PD neurons maintains post-inhibitory spiking latency (MacLean et al., 2003; 2005) and is preserved 4 days after deafferentation (Khorkova and Golowasch, 2007). Monoamines such as serotonin and dopamine enable slow, activity-dependent processes that regulate the correlation between I_A and I_h (Krenz et al., 2013; 2014; 2015), but how this correlation is maintained after deafferentation is still unknown. In our model, to make as few assumptions as possible, we did not implement any activity-dependent or neuromodulation-dependent mechanisms that directly regulate ion channel correlations, so the correlation between I_A and I_h was weak both before and 4 days after deafferentation. In future analysis, we can implement activity-dependent or neuromodulation-dependent mechanisms in the model and see how they constrain and shape the structures of degenerate parameter sets.

Another mismatch between experimental and computational findings is that negative ion channel correlations, except a few cases, are rarely observed *in vitro* (Ransdell et al., 2012; Zhao and Golowasch, 2012), but are often reported from computational studies (Taylor et al., 2009; Hudson and Prinz, 2010). The reason behind this mismatch is still unclear. One hypothesis is that constraining the model by an activity-dependent or neuromodulation-dependent mechanism might reduce the number of negative ion channel correlations, which can be tested in future studies.

2.4.4 Biological insights : Ion channel correlations at the neural circuit level

Despite a few computational and experimental studies (Grashow et al., 2010; Lane et al., 2016), it is still unclear what correlations exist between cellular and synaptic currents and how they contribute to maintaining neural activity at the neural circuit level.

Homeostatic plasticity maintains the stability of neural circuit function against developmental changes and pathological perturbations by adjusting the intrinsic excitability of individual neurons and/or the synaptic strengths between neurons. At a single neuron level, perturbed neural activities such as reduced neural firing rate can be compensated by increasing the number of depolarizing channels or reducing the number of hyperpolarizing channels in the membrane (Marder and Goaillard, 2006; Turrigiano, 2011). The neural circuit can also compensate for the reduced firing rate by increasing the excitatory synaptic strength and/or reducing the inhibitory synaptic strength of synaptic inputs it receives (Davis, 2006; Turrigiano, 2011; 2012; Vitureira et al., 2012), a mechanism called synaptic scaling. The recovery of the pyloric rhythm 3-4 days after deafferentation is regulated by homeostatic plasticity, and possibly involves tuning of both cellular and synaptic parameters. It is very challenging to conduct experiments that can track changes of both cellular and synaptic currents at the same time, and only two dynamic clamp studies have been done to examine how cellular and synaptic conductances compensate for each other to maintain similar pyloric rhythms (Grashow et al., 2010; Lane et al., 2016). Our approach offers a unique opportunity to examine changes of synaptic conductances and the correlations between cellular and synaptic conductances after deafferentation. We found that the overall strength of all fast, glutamatergic inhibitory synapses was reduced after deafferentation, while that of all slow, cholinergic inhibitory synapses stayed relatively unchanged. Reduction in the strength of inhibitory synapses compensates for the reduced excitation caused by I_{MI} removal. We also measured linear correlations between cellular and synaptic conductances, and did not find any strong linear correlations (i.e. above 0.6 or below -0.6) either before or after deafferentation.

2.4.5 Strength of our computational approach

The conventional approach in physiologically realistic modeling fits a single computational model to the average of experimental data, and conducts analysis by perturbing this single model. We have gained enormous insights from this conventional approach, but it has its own limits. Predictions generated from such single models are limited because such models ignore the intrinsic variability of neurons and circuits, which corresponds to a rich repertoire of neural dynamics and has been observed at the mRNA, conductance and physiology levels in diverse animal models (Schulz et al., 2006; 2007; Amendola et al., 2012; Temporal et al., 2012; 2014; Kim et al., 2017). Furthermore, the distribution of parameters might be nonlinear, in which case the average of the parameter sets may fail to produce neural activities generated by each parameter set (Golowasch et al., 1992; Marder and Taylor, 2011). These limits become problematic when we aim to understand a phenomenon or mechanism observed at the population level, like degeneracy in neurons and neural circuits, and therefore calls for a different modeling approach: ensemble modeling.

Employing an ensemble modeling approach called NSGA II, we were able to collect three groups of pyloric circuit model versions that can all produce one of three targeted pyloric rhythm versions, which enables us to examine structures of degenerate parameter sets and how they relate to the function of the pyloric circuit. Instead of a single model that produces a physiologically-realistic pyloric rhythm, examining a group of models that produce similar pyloric rhythms expanded our conceptual understanding of degeneracy in neurons and neural circuits.

2.4.6 Limitations in our computational approach

Ideally, to analyze structures of degenerate parameter sets, parameter sets should be sampled thoroughly and evenly, which requires a global parameter exploration method, such as constructing a database (Prinz et al., 2004). However, all global parameter exploration methods suffer from the curse of dimensionality, where the number of data points grows exponentially with the number of parameters in the model (Druckmann et al., 2007, 2014). Our model contains 34 parameters, so global parameter exploration would not be feasible, with the currently available computational power. We instead employed a parameter fitting method called NSGA II, which implements several strategies to sample the parameter space as thoroughly and evenly as possible (see Methods).

Many findings from our approach were also found independently in other simulation studies, which further implies that our results are insensitive to specific choice or setup of the chosen parameter fitting method. For example, the phenomenon that ion channel correlations are generally absent or weak, with a few strong ones regulating and maintaining the neural activity or behavior, has been observed in simulations of other invertebrate or vertebrate neurons using various parameter fitting algorithms (Achard and De Schutter, 2006; Taylor et al., 2009; Anirudhan and Narayanan, 2015). A parameter fitting algorithm, called Evolution Strategy was used to find combinations of parameters for a conductance-based model of cerebellar Purkinje cells with 24 parameters, with all identified parameter combinations able to produce similar responses to current injections (Achard and De Schutter, 2006). In that study, only 5 out of 276 possible pairs of parameters showed a linear correlation that was statistically significant. Back to the stomatogastric system, the strong linear correlation between I_A and I_{CaS} in PD that we found here was also identified in other studies (Liu et al., 1998; Hudson and Prinz, 2010; O'Leary et al., 2013). In summary, we are aware of the limits of our approach, primarily due to the curse of dimensionality, but do not think that our results are influenced by specific choices regarding the parameter fitting method.

2.4.7 Future Direction: A theoretical framework of degeneracy

In this study, we examined the linear structures of degenerate parameter sets by measuring Pearson's linear correlation between parameters and by principal component analysis. However, dynamics in living systems are highly nonlinear and therefore structures of degenerate parameter sets are possibly a combination of linear and nonlinear ones (Buzsaki, 2006; Craver, 2014). For example, the distribution of I_{Na} and I_{Kd} was L-shaped for all parameter sets of a neuron model that generated one-spike burster activity, and the average of all parameter sets that produced such neural activity failed to produce the same activity itself (Golowasch et al., 2002). Similar results were also observed in a more complex cerebellar Purkinje neuron model (Achard and De Schutter, 2006). Future work needs to apply appropriate measures to quantify nonlinear structures of degenerate parameter sets. A few candidate measures are mutual information and dimensionality reduction methods (Van der Maaten and Hinton, 2008; Berman et al., 2016).

To compare degenerate solutions at different time points during homeostatic regulation and from different neurons and neural circuits, we need to define measures of degeneracy. Degeneracy in qualitatively defined as combinations of parameters that give rise to similar outputs. But how similar is sufficient to be deemed functionally equivalent? What do we mean when we say one parameter set is more degenerate than the other? To answer these questions, we need to better understand how multiple cellular and synaptic parameters change in response to various perturbations and further develop methods to distill linear and nonlinear structures of degenerate parameter sets.

2.5 Acknowledgements

This work was supported by NIH Training Grant 5R90DA033462, and parameter search was performed on the Neuroscience Gateway Portal (Sivagnanam et al., 2013).

Chapter 3 Degenerate solutions in tSPNs in mice

3.1 Introduction

3.1.1 Background

Sympathetic postganglionic neurons (SPNs), the last common motor output of the sympathetic nervous system, pass converged motor commands from the spinal cord to downstream muscles and visceral organs. SPNs located in the thoracic region (tSPNs) of the sympathetic chain ganglia control vasomotor function to regulate vasculature in upper and middle extremities (Guyenet, 2006; Jänig, 2008), and dysfunction of tSPNs is implicated in various autonomic disorders such as autonomic dysreflexia (AD) (McLachlan, 2007; Macefield and Wallin, 2018). AD is characterized by spontaneous episode of hypertension that can be life-threatening, and occurs in patients with spinal cord injury at cervical and high thoracic regions (T6 and above) (Karlsson, 1999; Hou and Rabchevsky, 2014). tSPNs directly project to smooth muscles and organs that control blood pressure and vasculature, yet little is known about how they react to spinal cord injury, and the role they play in inducing spontaneous episodes of hypertension seen in AD.

To examine how tSPNs react to spinal cord injury, we first need to know the basic firing properties of tSPNs in healthy conditions. tSPNs are difficult to access *in vivo* due to the adherent fat surrounding them, so often their firing properties were inferred from SPNs located in the cervical and lumbar regions (Bratton et al., 2010; Rimmer and Horn, 2010). Up to date, there are only 3 *in vitro* studies of the firing properties of tSPNs in the vertebrate system (Blackman and Purves, 1969; Lichtman et al., 1980; Jobling and Gibbins, 1999), all employing a sharp microelectrode recording approach. However, recent studies indicate that, compared to whole-cell patch clamp recordings, sharp microelectrode recordings introduce electrode impalement-induced leak conductance to the neuron, leading to less accurate recordings (Staley et al., 1992; Springer et al., 2015). Our collaborators were able to perform whole-cell patch clamp recordings *ex vivo* and observed a rich repertoire of firing properties of tSPNs in mice (McKinnon et al., 2019). However, the biophysical mechanisms that produce this rich repertoire of firing properties of tSPNs are still unclear.

In addition, a recent RNA-Seq study identified two types of tSPNs expressing neuropeptide Y (NPY), NA2 and NA3, which differ in their cell diameter (Furlan et al., 2016). Roughly 7% of tSPNs are NA2 and 40% are NA3, and therefore ~50% of tSPNs are NPY^+. NPY^+ tSPNs preferentially innervate vasculature, yet little is known about whether and how they differ in intrinsic excitability and ability to integrate synaptic inputs (Springer et al., 2015). One the one hand, they may follow the size principle observed in motoneurons, where smaller neurons have higher resistance and therefore are recruited first (Cope and Pinter, 1995; Mendell, 2005). On the other hand, neurons need to maintain stable input-output relationships during development while cell size increases, and studies in various systems found that neurons of various sizes have similar excitability (Gorur-Shandilya et al., 2019).

Based on the whole-cell patch clamp recordings of tSPNs in mice, we were able to elucidate the biophysical mechanisms that underlie the basic firing properties of tSPNs by building a conductance-based single neuron model of tSPNs. We then built a database of tSPN model versions that vary in cell size and ion channel densities but can all produce realistic neural activities observed in experiments, and filtered out NA2-like and NA3-like tSPNs from the database based on cell size. By comparing the distribution of ion channel densities and f-I curves for NA2- and NA3-type tSPN models, we found that, compared to NA2-type tSPNs, NA3-type are more excitable and possess greater capability to integrate synaptic inputs.

3.1.2 Overview of sympathetic postganglionic neurons in mice

The autonomic nervous system (ANS) controls involuntary functions that are regulated by the activity of smooth muscle fibers, cardiac muscle fibers, glands, etc. Two major ANS divisions are the sympathetic and parasympathetic nervous system. Activity in the sympathetic nervous system (SNS) is generally associated with an increase in the level of excitation of an organism, which is sometimes referred to as the "fight or flight" response. The parasympathetic nervous system, on the other hand, regulates organ and gland functions at rest state, such as digestion and salivation (Kandel et al., 2000).

Sympathetic preganglionic neurons in the spinal cord integrate inputs from various subcortical and brainstem nuclei and project cholinergic inputs to sympathetic postganglionic neurons (SPNs) located in the sympathetic chain ganglia, which then project adrenergic inputs to downstream muscles and visceral organs (Fig 3.1A, right). The sympathetic chain ganglia, composed of interconnected paravertebral ganglia, are located ventral to the spinal column and are divided into four sections: superior / stellate cervical, thoracic, lumbar, and pelvic (Jänig, 2008) (Fig 3.1A, left). SPNs in the thoracic region (tSPNs) project to downstream targets such as vasculature, smooth muscles, brown adipose tissue, and sweat glands, and control various sympathetic activities (Jänig, 2008). Roughly 50% of tSPNs innervate vasculature and control blood pressure (Furlan et al., 2016; Macefield and Wallin, 2018). The majority of our collaborator's electrophysiological recordings focused on tSPNs located in the T5 region. The mean diameter of T5 cells is $23.8 \pm 5.4\ \mu m$ (Fig 3.1B).

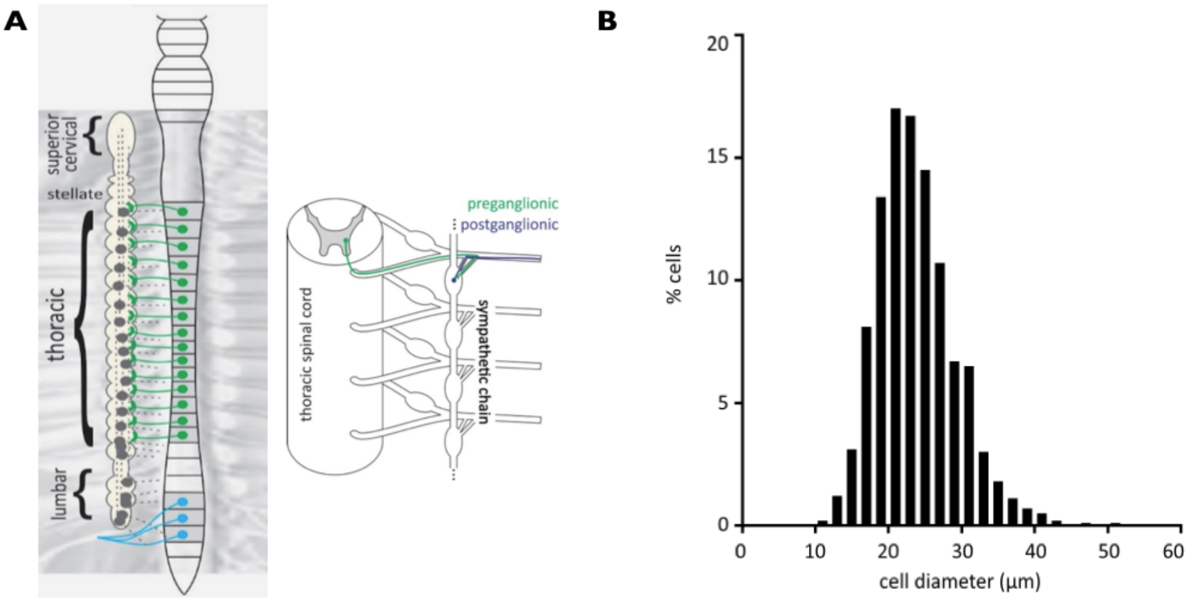

Figure 3.1 Anatomical organization of tSPNs. (**A**) Anatomical location of tSPNs. Left, The sympathetic ganglia chain runs in parallel with the spinal cord and contains four sections: superior / stellate cervical, thoracic, lumbar, and pelvic. Right, Projection from preganglionic neurons in the spinal cord (green) to postganglionic neurons in the thoracic ganglia (blue). (**B**) Histogram showing distribution of tSPN cell diameters in T5 ganglia of six animals. Figure was adapted from McKinnon *et al.*, 2019.

3.2 Methods

3.2.1 Single neuron model of tSPNs

We built a conductance-based neuron model to help determine the underlying cellular mechanisms of the observed firing properties of tSPNs. Dendritic arborizations of most tSPNs are relatively simple, indicating that cells are electrotonically compact (Jobling and Gibbins, 1999). We therefore assume that a single-compartment model can replicate all essential firing properties observed in experiments. All currents included in the model have been observed in rodent sympathetic ganglia (Galvan and Sedlmeir, 1984; Sacchi et al., 1995; Jobling and Gibbins, 1999; Rittenhouse and Zigmond, 1999) and transcript expression in mouse thoracic ganglia has recently been confirmed by a single-cell RNA sequencing study (Furlan et al., 2016).

The model is based on a model of bullfrog paravertebral sympathetic ganglia (Wheeler et al., 2004), from which the following ionic currents were taken: a fast sodium current, I_{Na}; a delayed-rectifier potassium current, I_{Kd}; a slow and non-inactivating potassium current, I_M; and a voltage-independent leak current, I_{leak}. Additional conductances were added from models derived in other species, which are: a fast transient potassium current, I_A (Rush and Rinzel, 1995); a hyperpolarization-activated cation current, I_h (Kullmann et al., 2016); and a calcium-dependent potassium current, I_{KCa} (Ermentrout and Terman, 2010). I_{KCa} depends on intracellular calcium concentration, $[Ca^{2+}]$, so a model of persistent calcium current, I_{CaL} (Bhalla and Bower, 1993) and somatic calcium dynamics (Kurian et al., 2011) were added as well. Model parameters were then tuned to fit recorded data from the present study.

The membrane voltage, V, is updated according to the equation:

$$C_m \frac{dV}{dt} = -\sum I_i - I_{input} \tag{3.1}$$

Membrane capacitance, C_m, was set at 100 pF to approximate the mean in recorded neurons. Each current, I_i, is described by the equation:

$$I_i = G_i m^p h^q (V - E_i) \tag{3.2}$$

where G_i is the maximal conductance, E_i is the reversal potential, and m and h are gating variables for activation and inactivation. A standard model neuron was used to replicate the majority of observed phenomena. Maximal conductances of this standard neuron are indicated in Table 3.1. The standard model was modified as necessary to fit individual recordings, which comprise a heterogeneous population. The reversal potentials for the various membrane currents are; 60 mV for I_{Na}; 120 mV for I_{CaL}; -90 mV for I_{Kd}, I_A, and I_{KCa}; -31.6 mV for I_h; and -55 mV for I_{leak}.

The activation and inactivation variables m and h are updated by the equation:

$$\frac{dx}{dt} = \frac{x_\infty - x}{\tau_x} \tag{3.3}$$

The intracellular calcium concentration is updated by:

$$\frac{d[Ca^{2+}]}{dt} = \lambda(-\alpha I_{CaL} - k_{CaS}[Ca^{2+}]) \tag{3.4}$$

where $\lambda = 0.01$ is the ratio of free to bound [Ca^{2+}], $\alpha = 0.002\ \mu M \cdot ms^{-1} \cdot pA^{-1}$ is the conversion factor from current to concentration, and $k_{CaS} = 0.024\ ms^{-1}$ is the somatic [Ca^{2+}] removal rate. Detailed implementation of each current is included in Appendix 5.2.

Table 3.1 Maximal conductances of base model neuron

G_i	G_{Na}	G_{CaL}	G_{Kd}	G_M	G_{KCa}	G_A	G_h	G_{leak}
Value (nS)	400	1	300	15	30	5	1	1

3.2.2 Synaptic inputs

Synaptic input was implemented with the equation:

$$I_{syn}(t) = g_{syn}(t) \cdot (V - E_{syn}) \tag{3.5}$$

where I_{syn} is synaptic current, and E_{syn} is the synaptic reversal potential set to 0 mV (Springer et al., 2015). Synaptic conductance, g_{syn}, was calculated from the equation:

$$g_{syn}(t) = s \cdot \left(e^{-t/\tau_d} - e^{-t/\tau_r}\right) \tag{3.6}$$

where τ_d and τ_r are the decay and rise time constants, respectively, s is a scaling factor to normalize the amplitude to 1nS, and t is the time since the onset of the synaptic input. Rise and decay time constants were 1 and 15ms, respectively, as estimated from voltage clamp recordings of spontaneous synaptic activity.

3.2.3 Brute force search

To automate the construction of a set of heterogeneous tSPN models of different sizes and excitability that could all reproduce the basic firing properties of tSPNs observed in experiments, we employ an ensemble modeling approach called brute force search (Prinz et al., 2004; Prinz, 2010b). We start with the base tSPN model described in Table 3.1, which contains eight free parameters: the maximum conductance of I_{Na}, I_{Kd}, I_{CaL}, I_{KCa}, I_M, I_A, I_h, and I_{leak}, and the cell capacitance. The cell capacitance is related to to cell size, and the maximum conductances together determine neuronal excitability. The explored range of each free parameter consists of five discrete values. For I_{Na}, I_{Kd}, I_{CaL}, I_{KCa}, I_M, and I_A, we constructed a range of values by multiplying its maximal conductance from the base tSPN model with 0.2, 0.6, 1, 1.4, and 1.8. To match the range observed in experiments, maximal conductance of I_{leak} from the base model was multiplied by 0.4, 0.8, 1.2, 1.6 and 2, and cell capacitance was multiplied by 0.5, 0.75, 1, 1.25, and 1.5. Together, this resulted in a database of size 5^9 =1,953,125 versions of the tSPN model with different parameter combinations that cover parameter space with a regular grid of parameter sets.

Table 3.2 Experimental ranges of tSPN firing features

Features	**Min**	**Max**
Resting membrane potential (mV)	-80	-46
Sag ratio	1.08	n/a
Firing rate at 50pA (Hz)	4.8	10
Firing rate at 75pA (Hz)	6	14.5
Firing rate at 100pA (Hz)	7	16
Adaptation ratio	1.25	2

We then parallelized the processing of the database to run it on high-performance computing clusters. Simulation results for each parameter sets were serially filtered from the database based on the following criteria, in order: i) firing rate falls in the range of [4.8, 10] Hz at 50pA current injection; ii) firing rate falls in the range of [6, 14.5] Hz at 75pA current injection; iii) firing rate falls in the range of [7, 16] Hz at 100pA current injection; iv) quasi-linear f-I curve based on values from i-iii; v) the presence of spike rate adaptation. These criteria were extracted from the measured electrophysiological properties of tSPNs and are summarized in Table 3.2. tSPN models that satisfy all five criteria above were deemed as qualified model versions.

3.2.4 Data analysis

3.2.4.1 Cell size conversion for vasculature-innervating tSPNs

Capacitance derived from cell diameter is usually smaller than that measured from electrophysiological recordings partly because the former assumes an electrotonically compact neuron and therefore often underestimates the capacitance. Capacitance in our model is based on the measurements from electrophysiological recordings. For NA2- and NA3-type neurons, we only know the average cell diameter from a previous RNA-Seq study (Furlan et al., 2016), so we estimated their capacitance based on the equation below:

$$C_E = \alpha C_A \tag{3.7}$$

where C_E is the estimated capacitance from electrophysiological recordings, and C_A is the capacitance calculated from their average cell diameters and a standard capacitance per unit area of membrane of 1 $\mu F/cm^2$. α is determined by the ratio of the average capacitance measured from electrophysiological recordings divided by the capacitance calculated from the average cell diameters of all types of tSPNs (McKinnon et al., 2019).

Values of each parameter are indicated in Table 3.3. The estimated capacitances of NA2- and NA3-type neurons are 74.15 pF and 49.7 pF, respectively, which were rounded to 75 and 50 pF in our model.

Table 3.3 Estimating capacitance of NA2- and NA3-type tSPNs

	Diameter (μm)	**C_E (pF)**	**C_A (pF)**	**α**
All tSPNs	23.8	89.2	17.79	5.01
NA2	21.72	74.15	14.8	
NA3	17.78	49.70	9.92	

3.2.4.2 Pearson's correlation coefficient and correlation matrix

Pearson's correlation coefficient was computed by the *pearsonr* function from Python's SciPy Toolbox (version 1.2.1), and the correlation matrix was plotted using the *matshow* function from Python's Matplotlib Toolbox (version 2.2.4). Significance tests were conducted using two-tailed t-test.

3.2.4.3 Standard score

Standard score measures deviations from the mean by subtracting the mean of the distribution from each value in the distribution, divided by the standard deviation of the distribution. If all values in the distribution are identical, standard score is set to 0.

3.2.5 Implementation and code accessibility

Simulation and analysis scripts were written in Python 2.7.12 and executed in PyCharm (CE 2017.1.2) on macOS 10.12.3 with a 1.7-GHz processor. Automated parameter fitting was parallelized by the SCOOP module and run on the Neuroscience Gateway Portal (Sivagnanam et al., 2013). Differential equations were numerically integrated using the

Exponential Euler method with a time step of 0.05 ms (Dayan & Abbott, 2001). Python code of simulation and data analysis is available at https://github.com/pinewave/Conductance-based-model-of-rodent-thoracic-sympathetic-postganglionic-neuron.

3.3 Results

3.3.1 Cellular mechanisms underlying firing properties of tSPNs when hyperpolarized

To build a conductance-based neuron model of tSPNs, we first set the cell capacitance and input conductance, two essential passive membrane properties of tSPNs, to approximately the average values observed in experiments, which are 100 pF and 1000 $M\Omega$, respectively.

Starting with three ionic currents extracted from a bullfrog paravertebral sympathetic ganglia model (Wheeler et al., 2004), which are I_{Na}, I_{Kd}, and I_{leak}, we then analyzed and added the ionic currents underlying three firing properties of tSPNs observed at hyperpolarization. tSPNs exhibited delay to the first action potential in a spike train when depolarized from a holding potential of -90 mV *ex vivo* (Fig 3.2Ai). No delay was observed when the same neuron was depolarized from -70 mV (Fig. 3.2Ai). Previous modeling studies indicate that the delay can be attributed to de-inactivation of the transient, voltage-gated A-type potassium current (I_A) (Rush and Rinzel, 1995), so I_A was added to the model and its maximal conductance was adjusted to match the experimental results (Fig. 3.2Aii).

Another firing property observed at various hyperpolarizing current injections was a “sag” conductance, which became more prominent when the hyperpolarizing current amplitude increased (Fig 3.2Bi). This phenomenon has been observed in mouse tSPNs (Jobling and Gibbins, 1999) and was explained by the hyperpolarization-activated inward current (I_h), whose kinetics in mouse SPNs have been characterized in a previous study (Kullmann et al., 2016). We implemented I_h in the model and adjusted its maximal conductance to replicate the voltage traces observed *ex vivo* (Fig 3.2Bii).

Post-inhibitory rebound from releasing hyperpolarizing current injection was also observed in tSPNs (Fig 3.2Ci). One common mechanism to induce post-inhibitory rebound is the de-inactivation of a fast inward current, such as the T-type calcium current (I_{CaT}) (Ermentrout and Terman, 2010). However, preliminary voltage clamp results ruled out the existence of I_{CaT} in tSPNs (McKinnon personal observations). Another candidate is I_h, where an enhanced version with larger amplitude and slower activation and inactivation kinetics could induce post-inhibitory rebound (Chen et al., 2001). However, the kinetics of the enhanced I_h did not match those characterized in mouse SPNs (Kullmann et al., 2016). We noticed that rebound firing was only observed when the resting membrane potential was near firing threshold (between -60 and -50 mV), a condition where changes in I_{Na} and I_{Kd} dynamics were able to induce post-inhibitory rebound. Specifically, at hyperpolarized voltages, the activation and inactivation of I_{Na} become faster while the activation of I_{Kd} becomes slower. Upon sudden release from the hyperpolarizing step, I_{Na} has the ability to induce a spike before the activation of I_{Kd}. By adjusting the maximal conductances of I_{Na} and I_{Kd}, we were able to replicate the post-inhibitory rebound seen in experiments (Fig 3.2Cii).

3.3.2 Cellular mechanisms underlying firing properties of tSPNs when depolarized

Two prominent firing properties of tSPNs observed at depolarizing current injection are spike rate adaptation and repetitive firing. The frequency of repetitive firing is influenced by the combination of all underlying ionic currents, so we first identified ionic currents accountable for spike rate adaptation. The low-threshold, non-inactivating potassium current (I_M) was observed in bullfrog sympathetic ganglia, where it was responsible for spike rate adaptation, so we incorporated it into our model (Wheeler et al., 2004). However, it was only able to reproduce the fast phase of spike rate adaptation (Fig 3.3B, D). I_{KCa} and I_{CaL} have been observed in rat superior cervical ganglia (Galvan and Sedlmeir, 1984; Sacchi et al., 1995; Rittenhouse and Zigmond, 1999) and were therefore incorporated into the model (Bhalla and Bower, 1993; Ermentrout and Terman, 2010). The added I_{KCa} was able to account for the slow phase of spike rate adaptation (Fig 3.3B, D), and together I_M and I_{KCa} were able to reproduce the spike rate adaptation from a recorded neuron receiving 50 pA current injection (Fig 3.3A) and to match both the maximal and sustained firing rate at various current injections (Fig 3.3C).

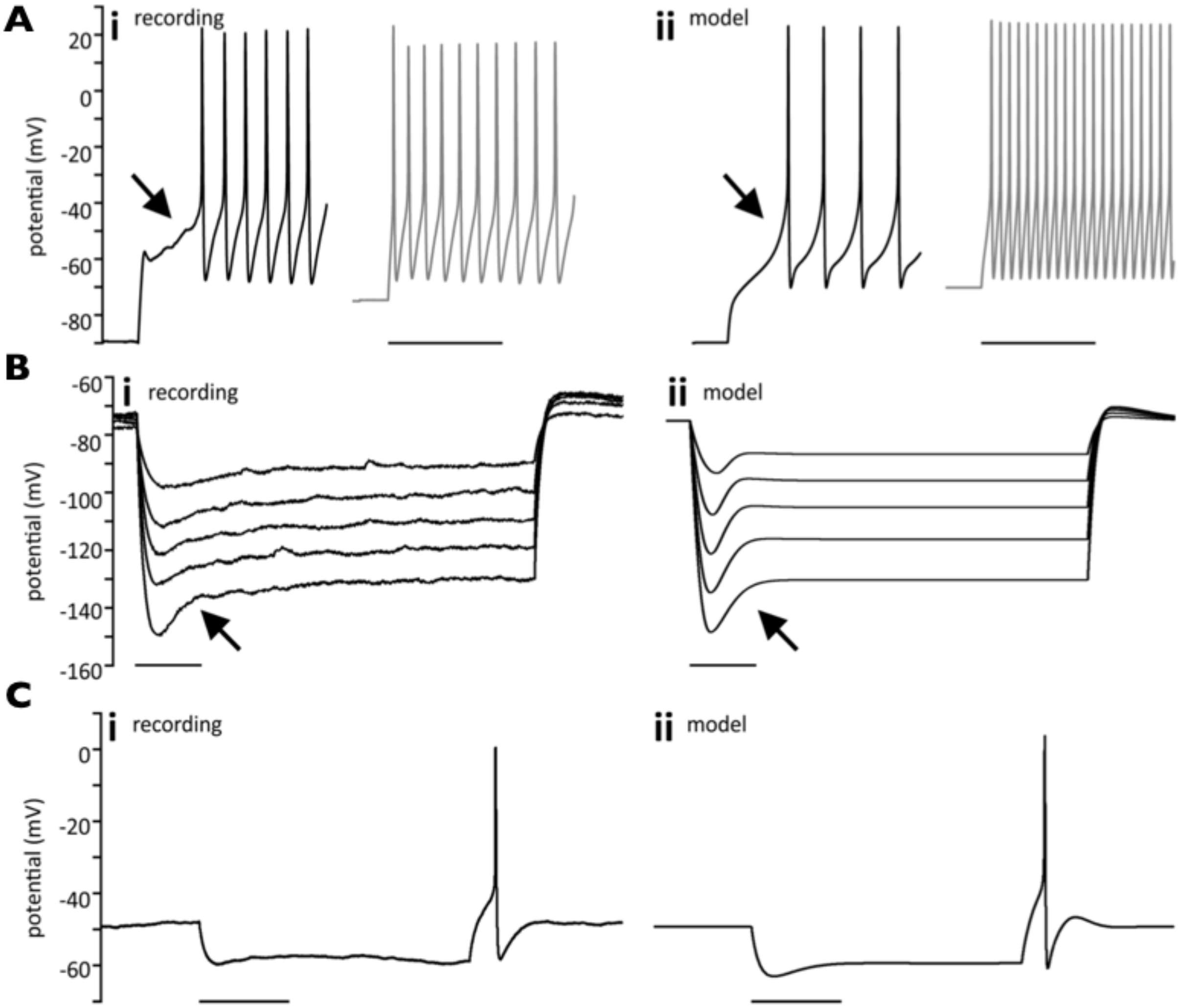

Figure 3.2 Cellular mechanisms underlying firing properties of tSPNs when hyperpolarized. (**A**) *i*, A cell depolarized from -90 mV exhibits a characteristic notch (arrow) accompanied by a delay in spiking (black trace). The same cell depolarized from -70 mV does not have a notch (gray trace). *ii*, Model neuron showing comparable results with pre-spike inflection seen only for hyperpolarized trace. Standard model with G_M 10 nS, G_{KCa} 10 nS, G_A 90 nS, G_{leak} 0 nS. **(B)** *i*, Voltage sag, indicated by arrow, upon hyperpolarization beyond -90 mV in a cell held at -70 mV. Note that the effect becomes more pronounced with greater hyperpolarization. *ii*, Model neuron showing similar sag. Standard model with G_A 5 nS and G_{leak} 0.1 nS. **(C)** *i*, Hyperpolarizing trace from a different cell held at -50 mV showing rebound spiking associated with voltage sag. *ii*, Model neuron showing rebound spiking at the same holding voltage and current injection. Maximal conductances are: G_{Na} 200 nS, G_{Kd} 2000 nS, G_{CaL} 1.2 nS, G_M 20 nS, G_{KCa} 20 nS, G_A 20 nS, G_h 1 nS, G_{leak} 2 nS. Scale bar: 1s. Figure was adapted from McKinnon *et al*., 2019.

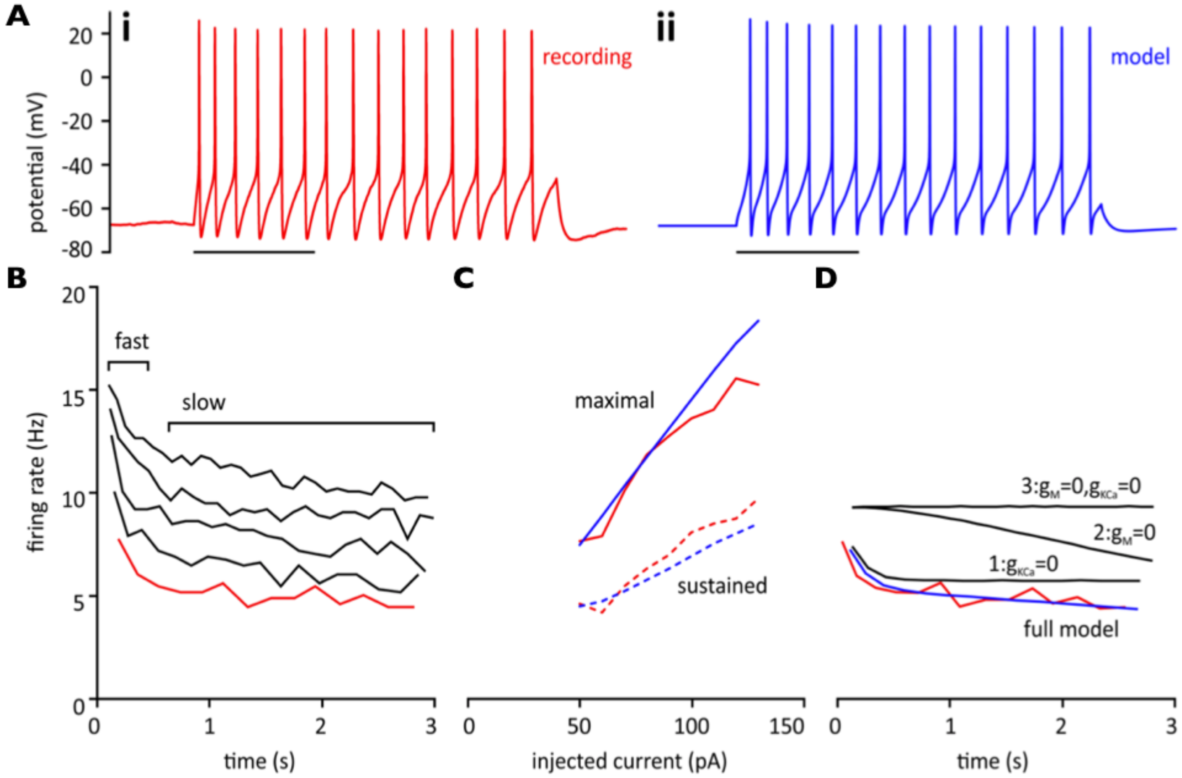

Figure 3.3 Both I_M and I_{KCa} are necessary for spike rate adaption in tSPNs. (**A**) ***i*,** Representative trace showing tSPN response to a 50 pA current injection. Note that the interspike interval increases over time, corresponding to a decrease in instantaneous frequency. ***ii***, Trace from a model cell chosen to fit the recording shows similar SRA for a 50 pA current injection. Maximal conductances are: G_{Na} 400 nS, G_{Kd} 3000nS, G_{CaL} 1.2nS, G_M 40nS, G_{KCa} 60nS, G_A 80nS, G_h 1nS, G_{leak} 2nS. Scale bar in both panels is 1s. **(B)** Instantaneous frequency versus time for the same recorded cell at 50, 70, 90, 110, and 130 pA current injection (from bottom to top). The 50 pA curve (red) corresponds to the trace in *Ai*. Fast and slow components of adaptation are indicated. **(C)** Maximal and sustained *f*-I curves match well between recorded and modeled cell over a range of injected currents. Red, maximal (top, solid) and sustained (bottom, dashed) *f*-I curves for the cell in *Ai*, *B*. Blue lines are the corresponding *f*-I curves from the model cell in *Aii*. ***D***: Instantaneous frequency versus time curves for the model cell in *Aii*. The recorded 50 pA curve from *B* is reproduced for comparison to the analogous curve generated in the model cell in *Aii* (blue). Black curves numbered 1–3 represent effect of removal of two conductances from the model. Removal of gKCa (curve 1) predominantly influences the slow SRA. Removal of gM (curve 2) predominantly influences the fast SRA. Removal of both (curve 3) eliminates SRA. The ordinate axis is shared among *B*–*D*. Figure was published in McKinnon *et al*., 2019.

After identifying all the ionic current components in the model neuron that are necessary to replicate basic firing properties of tSPNs (Fig 3.4C), we adjusted the maximal conductances of each ion current to match the increased frequency of repetitive firing in response to increased amplitude of current injections, ranging from 30 pA, 50 pA, …, to 130 pA (Fig 3.4A). f-I curves of both maximal and sustained firing rate from our model neuron fall within the range observed in experiments (Fig 3.4B). Maximal firing rate was defined as the inverse of the first interspike interval in response to current injection, while sustained firing rate was defined as the average of the inverse of the last three interspike intervals during a current injection.

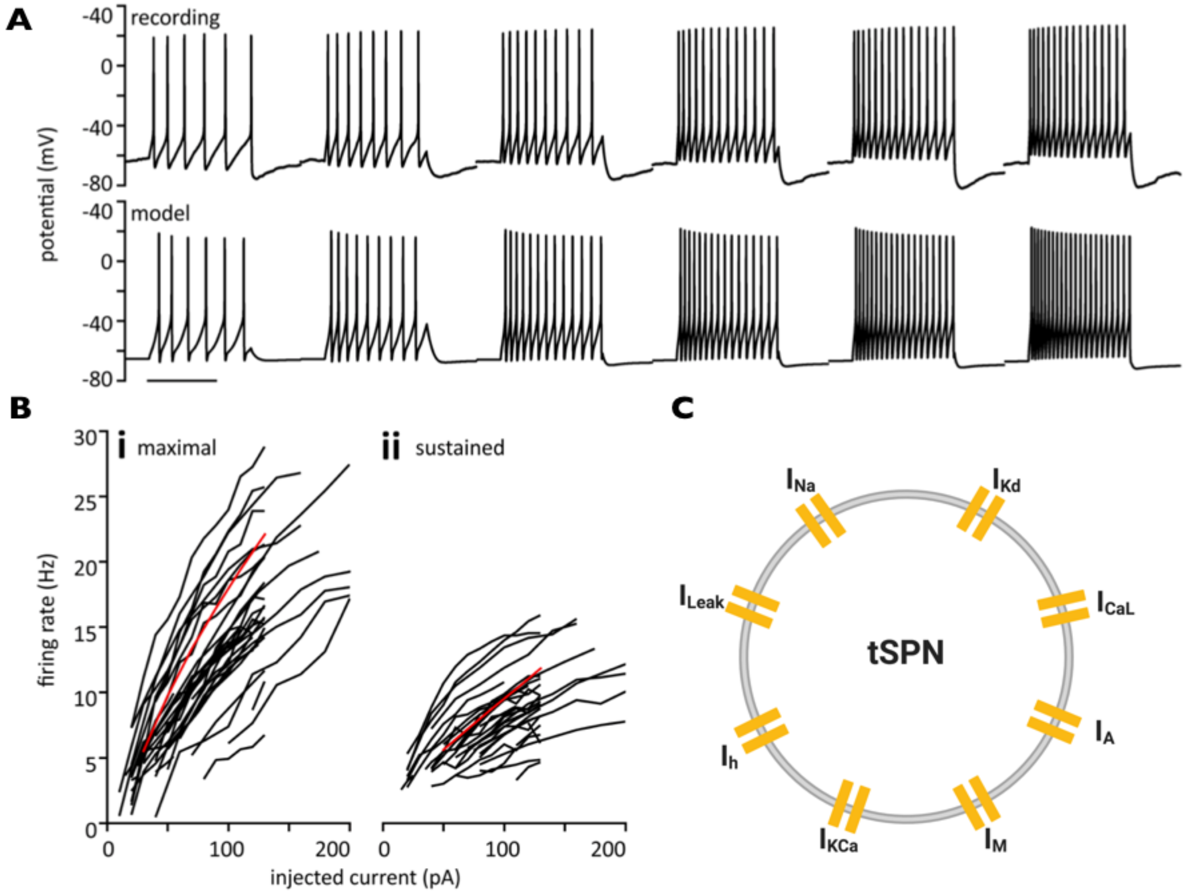

Figure 3.4 Reproducing the repetitive firing properties of tSPNs. (**A**) Top, representative trace from a tSPN showing increased repetitive firing frequency in response to increasing current steps. Bottom, model neurons also showing repetitive firing. Injected current from left to right in both recorded and model neurons is 30, 50, 70, 90, 110, 130 pA. Scale bar is 1 s. (**B**) f-I curve for recorded and model neurons. *i,* Maximal firing rate is plotted versus injected current for all cells. *ii,* Same as Bi with sustained firing rate. Red line in i and ii is maximal and sustained f-I curve from model neuron. **(C)** Diagram showing the composition of ionic currents in the single neuron model. Figure 3.4A and 3.4B were published in McKinnon *et al.,* 2019.

3.3.3 Model neuron is capable of integrating synaptic inputs

tSPNs exhibit spontaneous excitatory postsynaptic currents (sEPSCs), which can sometimes summate to generate spikes (Fig 3.5A). A recent study in the rat sympathetic neurons found 2.4-fold synaptic gain without the electrode impalement-induced leak conductance (Kullmann et al., 2016), which challenges the conventional view of tSPNs as 1:1 relays that simply pass down the motor commands from the spinal cord to downstream targets. To explore the impact of impalement-induced leak conductance on synaptic integration in mice tSPNs, we implemented a Poisson-distributed synaptic input template whose amplitude and mean frequency match values from whole-cell clamp recordings (Fig 3.5B, bottom trace). Our model neuron was able to integrate sub-threshold synaptic inputs to generate spikes (Fig 3.5B, top trace). To simulate impalement introduced by sharp microelectrode recordings, a leak conductance of 7 nS was added to the model. Setting the value to 7 nS results in an input resistance of ~ 100 $M\Omega$, which matches the mean value of input resistance observed in a previous sharp electrode experiment (Jobling and Gibbins, 1999). The model failed to integrate sub-threshold inputs after adding a 7 nS impalement-induced leak conductance (Fig 3.5B, middle trace).

3.3.4 Two types of vasculature-innervating tSPNs

Vasomotor postganglionic neurons release NPY, which activates vasoconstriction. The two types of NPY^+ tSPNs, NA2 and NA3, differ in their intrinsic excitability. We constructed a database of heterogeneous tSPN models of different sizes and ion channel densities that could all reproduce the basic firing properties observed in experiments. Out of all the model versions tested (n=1,953,125), 31, 421 model versions can generate realistic firing properties of tSPNs and are deemed as physiologically-realistic, out of which 192 match the size of NA3-type tSPNs and 5,467 match the size of NA2-type tSPNs.

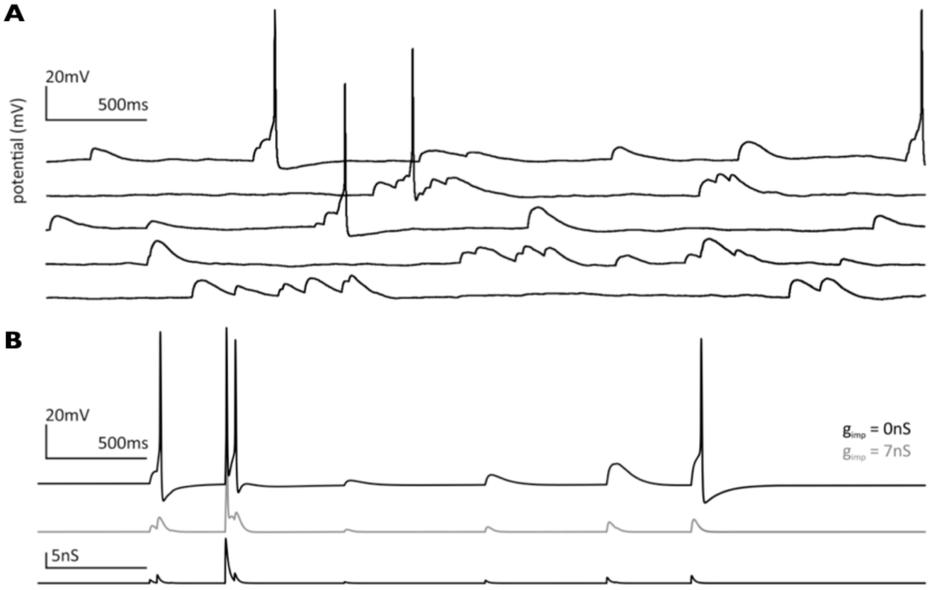

Figure 3.5 tSPN model neuron is capable of integrating synaptic inputs. (A) Example of synaptic summation leading to AP firing in a particularly active recording. Shown are five epochs of spontaneous synaptic activity. Cell resting membrane potential was -60 mV. In this neuron, a membrane time constant of 109 ms led to comparably long EPSP membrane voltage decays. Vertical scale bar is 20 mV; horizontal scale bar is 500 ms. **(B)** Top, Model neuron subjected to simulated synaptic input fires in response to synaptic summation. Middle, If an impalement conductance is added, synaptic summation is no longer effective. Bottom, Simulated synaptic conductances used to generate voltage traces. Horizontal scale bar is 500 ms; vertical scale bars are 20 mV and 5 nS, respectively. Figure was published in McKinnon *et al.,* 2019.

We then plotted the distribution of each ion channel density for NA2- and NA3-type tSPN models (Fig 3.6A), and found that compared to NA2-type tSPNs, NA3-type tSPNs have lower densities of I_{leak}, making them more capable of integrating synaptic inputs. NA3-type tSPNs also exhibit lower densities of hyperpolarizing currents such as I_{Kd}, I_{KCa}, and I_A, making the neurons more excitable. They also show a higher density of I_M, a current that reduces the excitability of neurons by enhancing spike rate adaptation.

To see whether NA2- and NA3-type tSPNs differ in their excitability due to the different distributions of ion channel densities, we plotted the f-I curves of model versions of both types, and found that within the range of firing rates observed *ex vivo*, NA3-type tSPNs fire at relatively high frequency while NA2-type tSPNs are capable of a wider range of firing (Fig 3.6B). Despite the difference in f-I curve distributions, the slope of f-I curves does not correlate with cell size (Fig 3.6C), which matches our experimental findings (McKinnon et al., 2019).

Given the different distributions of ion channel densities for NA2- and NA3-type tSPNs, we wondered how each type of ion channel influences the firing properties of tSPNs. To investigate this, we varied the density of I_M and I_A in the model neuron, one at a time, and found that increasing the density of either current switched the neuron from repetitive firing to phasic firing (Fig 3.7A). To examine how the firing mode of tSPNs switches in response to concurrent changes of I_M and I_A, we systematically varied I_M and I_A together, and found that the switch of firing mode is more sensitive to changes in I_A when I_M is high (Fig 3.7B).

To identify linear structures of all physiologically-realistic parameter sets, we employed similar strategies use9 in Chapter 2 to measure ion channel correlations by Pearson's correlation coefficient and visualized them by plotting the correlation matrix (Appendix, Fig 5.3A). We observed that G_h had the weakest correlations to other parameters, and plotted the distribution of G_h vs. G_{leak} as an example ($r = 0$) (Appendix, Fig 5.3B). We also plotted the distribution of the strongest correlation, which is between G_M and G_{leak} ($r = -0.51$) (Appendix, Fig 5.3B). Overall, all the ion channel correlations are weak or absent ($-0.6 < r < 0.6$). By further examining the distributions of pairwise parameters (Appendix, Fig 5.3B), we think this is due to both the narrow pre-defined search range of parameter values and the coarse grid of parameter search, and therefore cannot rule out the existence of strong correlations.

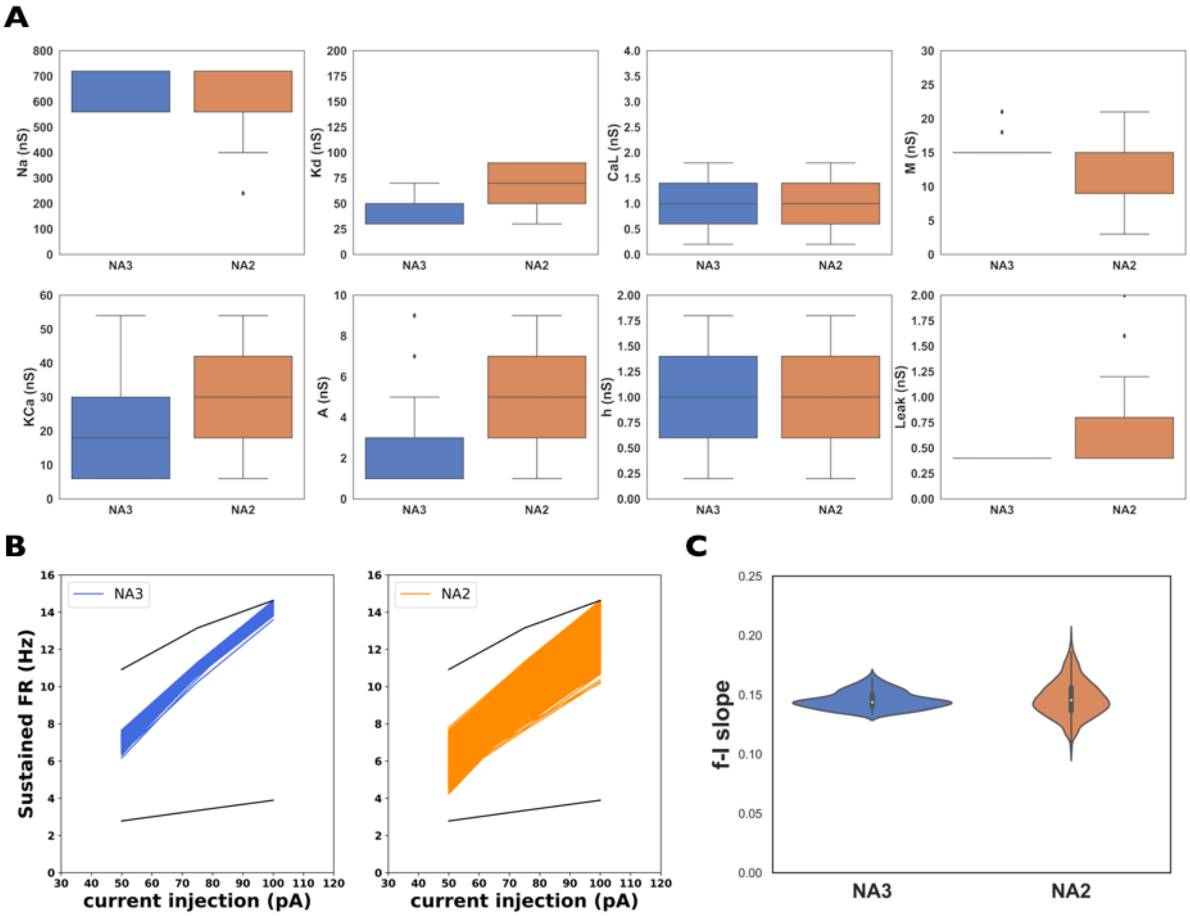

Figure 3.6 NA2- and NA3-type tSPNs differ in excitability. (A) Box plots showing the distribution of each parameter in NA2- (orange, n = 5,467) and NA3-type (blue, n =192) tSPNs. Black line in the box indicates the median of the distribution. Upper and lower edges of each box represents the 75% and 25% quartile, and the lines parallel to the boxes are minimum and/or maximum values of the distribution. Outliers are plotted as individual dots. **(B)** f-I curves for NA2- (orange) and NA3-type (blue) tSPNs. Black lines indicate the minimum and maximum firing rates observed at 50, 75, and 100 pA current injections *ex vivo*. **(C)** Violin plots showing the distribution of f-I slopes for NA2- (orange) and NA3-type (blue) tSPNs. Distribution of the f-I slopes is visualized by the “violin” shape, where the width reflects the frequency. White dot: median of the distribution. Black bar: interquartile range. Black vertical line: minimum and maximum of the distribution.

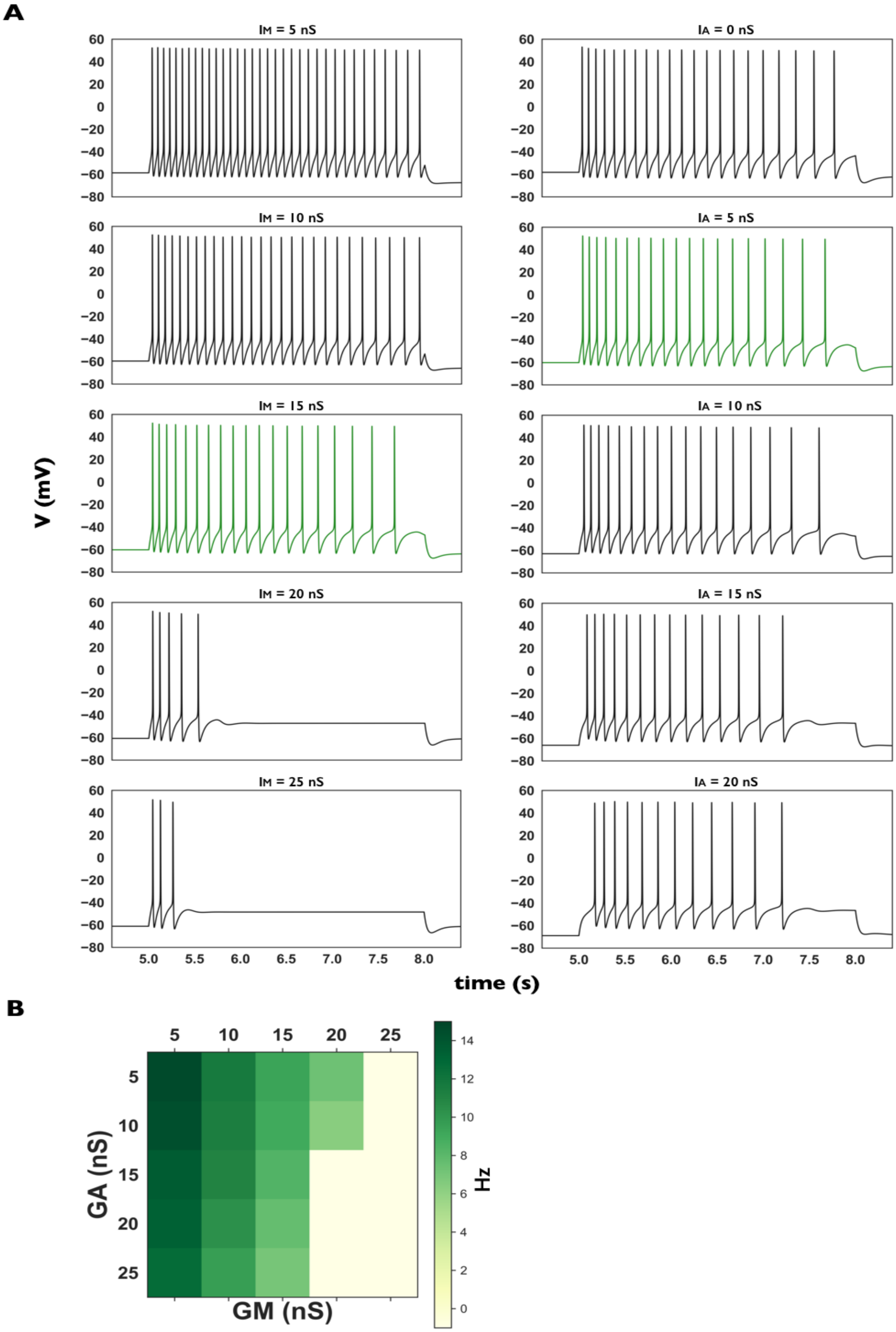
A
IM = 5 nS
IM = 10 nS
IM = 15 nS
IM = 20 nS
IM = 25 nS
IA = 0 nS
IA = 5 nS
IA = 10 nS
IA = 15 nS
IA = 20 nS
V (mV)
60
40
20
0
−20
−40
−60
−80
5.0
5.5
6.0
6.5
7.0
7.5
8.0
time (s)
B
5
10
15
20
25
GA (nS)
GM (nS)
Hz
14
12
10
8
6
4
2
0

Figure 3.7 Increasing either I_M or I_A switches tSPNs from repetitive to phasic firing. Maximal conductances of the model neuron (green) are: G_{Na} 720nS, G_{Kd} 90nS, G_{CaL} 1nS, G_M 15nS, G_{KCa} 42nS, G_A 5nS, G_h 1nS, G_{leak} 0.8nS, and C_m 75 pF. **(A)** I_M or I_A of the model neuron (green trace) was varied. Left: Maximal conductance of I_M increased from 5, 10, …, to 25 nS from top to bottom. Right: Maximal conductance of I_A increased from 0, 5, …, to 20 nS from top to bottom. **(B)** I_M and I_A of the model neuron were varied together. Maximal conductance of I_M and I_A increased from 5, 10, …, to 25 nS. Color bar indicates the firing rate of simulated tSPN spiking activities from each combination of I_M and I_A. Firing rate of zero (yellow) corresponds to phasic firing mode.

3.3.5 tSPNs with identical f-I curve differ in their ability to integrate synaptic inputs

Preliminary experimental data show that, six weeks after SCI, the slope and range of tSPNs' f-I curves were similar to those before SCI (Li, McKinnon and Hochman, personal communications). To identify vasculature-innervating tSPNs with similar f-I curves, we grouped NA2- and NA3-type tSPN models by how similar their f-I curves are. For each type, tSPNs were grouped together as one degenerate set if the difference of their f-I curves across all current injections is within 0.1 Hz. Under this definition, we found 39 non-overlapping degenerate groups in NA3-type tSPNs and 813 in NA2-type tSPNs, while the size of each degenerate group ranged from 2 to 25. To quantify the similarity of parameter sets within each degenerate group, for each parameter set, we computed the standard score of each parameter by comparing it to the mean and standard deviation of the degenerate group it belonged to, and plotted the distribution of standard scores for all parameter sets from all degenerate groups (Fig 3.8). By comparing the standard score distribution between NA2- and NA3-type tSPNs, we found that I_M is less variable for both NA2- and NA3-type tSPNs, indicating that a tight regulation of I_M is necessary to maintain the same (or similar) f-I curve (Fig 3.8A, B). I_{Kd} and I_{leak} are also tightly regulated in NA3-type tSPNs (Fig 3.8A). Combining with Fig 3.6A, we see that maximal conductances of both I_{Kd} and I_{leak} are aggregated near the minimum possible value, suggesting that tight regulations of I_{Kd} and I_{leak} are due to the narrow range of possible parameter values.

To investigate whether vasculature-innervating tSPNs with similar f-I curves differ in their capability to integrate synaptic inputs *in vivo*, we simulated a synaptic input template that matches the frequency and amplitude distributions of spontaneous excitatory synaptic inputs to tSPNs observed *ex vivo* (Fig 3.9A, Bottom), and fed it to two NA2-type tSPNs with identical f-I curves (Fig 3.9A, Top) but different underlying ion channel densities (Fig 3.9B, Bottom). The two tSPNs shown in Fig 3.9B came from a randomly selected NA2-type degenerate group. Despite having identical f-I curve and receiving identical synaptic inputs, the two NA2-type tSPNs differ in their capability to integrate synaptic inputs (Fig 3.9B, Top). This indicates that, although tSPNs show similar f-I curves before and six weeks after SCI, they may still differ in their capability to integrate synaptic inputs *in vivo*, and the f-I curve as a measure of excitability does not reveal this difference. A closer examination of the two parameter sets shows that the two tSPNs have the same leak conductance and capacitance, indicating that they have the same passive membrane time constant. Therefore, the different capability to integrate *in vivo* synaptic inputs results from combined changes of depolarizing and hyperpolarizing membrane currents.

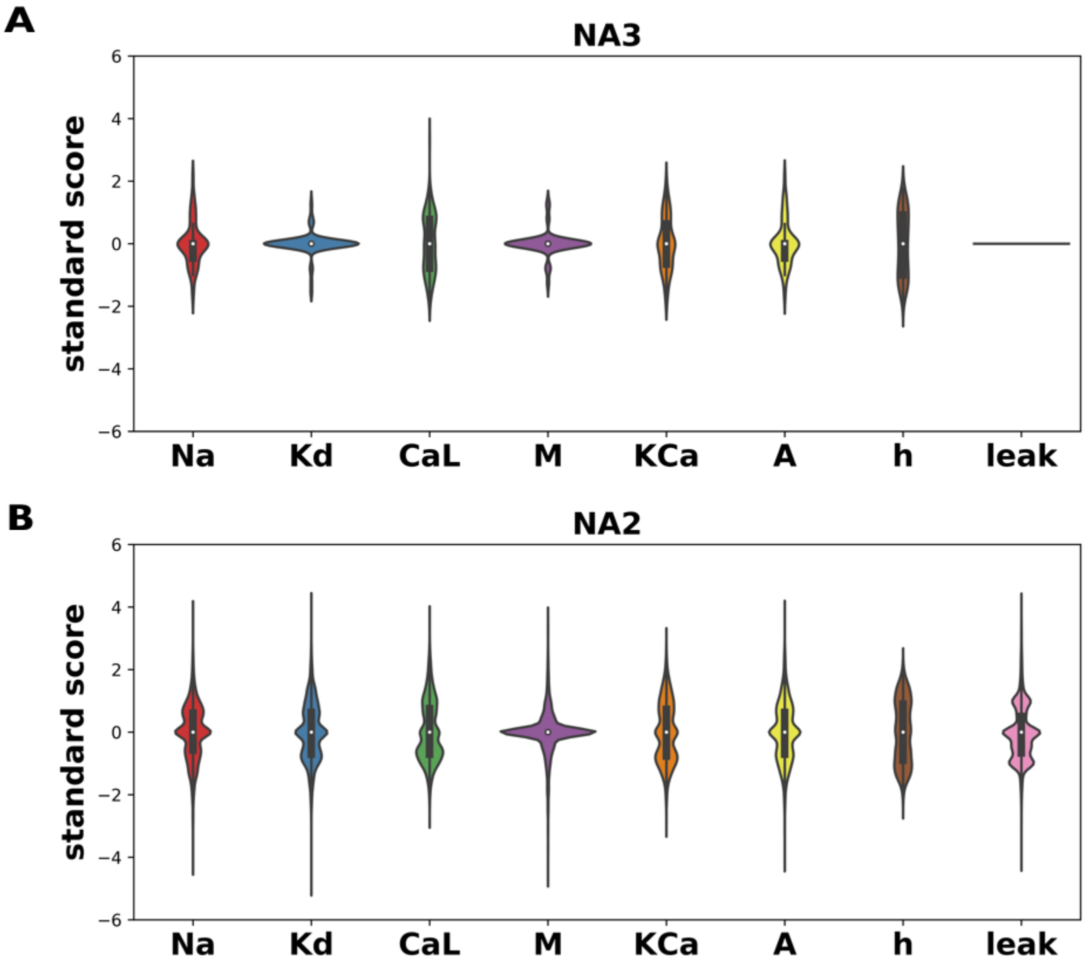

Figure 3.8 Degenerate solutions in vasculature-innervating tSPN models. (A) Violin plot showing the distribution of standard scores of each parameter for NA3-type tSPN models. **(B)** Violin plot showing the distribution of standard scores of each parameter for NA2-type tSPN models. Distribution is visualized by the "violin" shape, where the width of the distribution reflects the frequency. White dot: median of the distribution. Black bar: interquartile range. Black vertical line: minimum and maximum of the distribution.

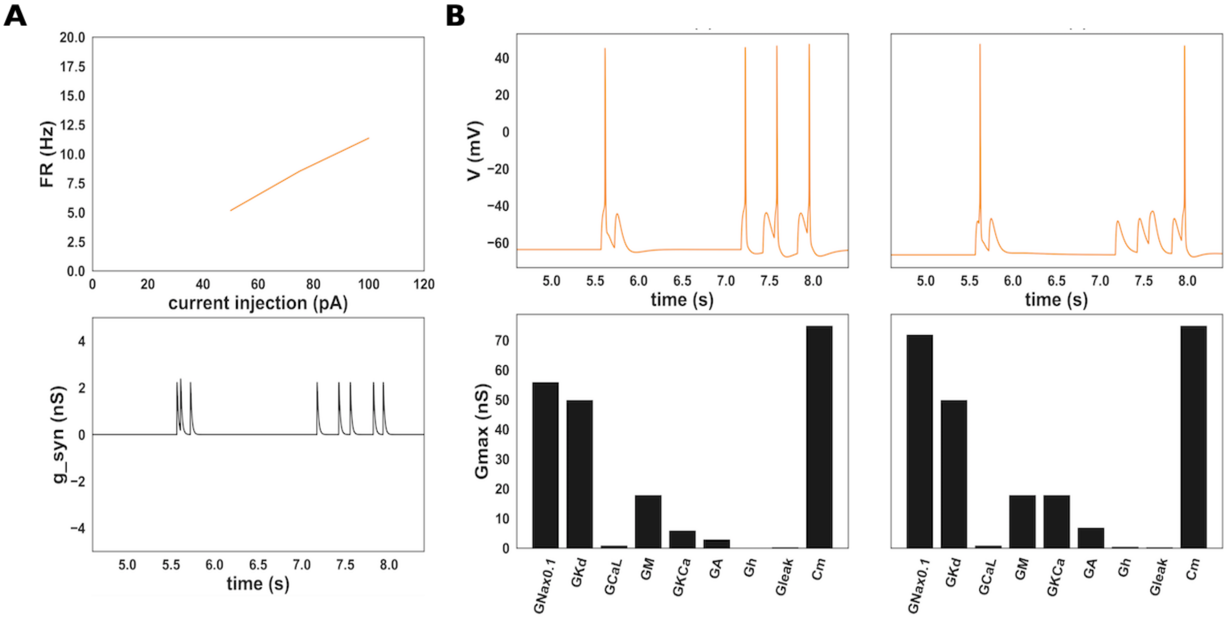

Figure 3.9 tSPNs with identical f-I curve differ in their capability to integrate synaptic inputs. (A) Two NA2-type model neurons show identical f-I curve (Top) and receive identical synaptic inputs (Bottom). **(B)** Two NA2-type model neurons, despite having identical f-I curve and synaptic inputs, differ in underlying ion channel densities (Bottom) and show different capability to integrate synaptic inputs (Top). Maximal conductances for model (left) is: G_{Na} 560 nS, G_K, 50 nS, G_{CaL} 1 nS, G_M 18 nS, G_{KCa} 6 nS, G_A 3 nS, G_h 0.2 nS, G_{leak} 0.4 nS, and C 75 pF. Maximal conductances for model (right) is: G_{Na} 720 nS, G_K, 50 nS, G_{CaL} 1 nS, G_M 18 nS, G_{KCa} 18 nS, G_A 7 nS, G_h 0.6 nS, G_{leak} 0.4 nS, and C 75 pF.

3.4 Discussion

3.4.1 Summary of results

Based on high-fidelity whole-cell patch clamp recordings of tSPNs, we built the first physiologically-realistic single neuron model of tSPNs in mice and elucidated the cellular mechanisms underlying the basic firing properties of tSPNs. We found that both I_M and I_{KCa} are necessary and sufficient to reproduce spike rate adaptation seen in tSPNs, and confirmed that an impalement leak conductance introduced by sharp microelectrode penetration reduces tSPNs' ability to integrate sub-threshold synaptic inputs. We further built a collection of models for both types of vasculature-innervating tSPNs, NA2 and NA3, and found that they differ in their distributions of underlying ion channel densities and f-I curves, which may affect their ability to integrate synaptic inputs. These insights into the cellular mechanisms of excitability in tSPNs will help us understand abnormal neural activities of tSPNs, such as the induction of hyperexcitability in tSPNs after SCI and how it might contribute to the spontaneous episodes of hypertension in AD patients.

3.4.2 The influence of cell size on neuronal excitability

Cell size of tSPNs varies, raising the possibility that recruitment of tSPNs could follow the size principle observed in motoneurons, where smaller neurons are recruited first because larger neurons with more membrane and thus more resistances in parallel would have lower total resistance (Cope and Pinter, 1995; Mendell, 2005). Recruitment of tSPNs by size principle has been observed in a few clinical studies (Steinback et al., 2010; Klassen et al., 2018). However, cell size is just one parameter that can affect the excitability of neurons, and its effect can be compensated by changes in the densities of various ion channels in the neuron. For example, in the lobster *Homarus americanus*, the bursting activity of pyloric neurons is similar between juveniles and adults, despite a many-fold increase in cell size (Bucher et al., 2005). To investigate whether two types of vasculature-innervating tSPNs, NA2 and NA3, differ in their intrinsic excitability because of their cell size difference, we combined our single neuron model of tSPNs with an ensemble modeling approach to generate a collection of models for each NPY$^+$ type, where the cell size in each model matches that of NA2 or NA3 but the underlying ion channel densities vary. Based on the distribution of ion channel densities and of f-I curves for NA2- and NA3-type tSPNs, we found that NA3-type tSPNs are more excitable than NA2-type tSPNs, which may lead to greater ability to integrate synaptic inputs *in vivo* (Furlan et al., 2016).

3.4.3 Firing mode: integrator vs. coincidence detector

The conventional view of tSPNs treats them as 1:1 relays that pass down the motor commands from the strongest preganglionic synaptic inputs to regulate vasculature (Macefield and Wallin, 2018; McLachlan, 2007; Guyenet, 2006). However, a recent study shows that, without the electrode impalement-induced leak conductance, the synaptic gain, defined as the average postsynaptic firing rate divided by the average presynaptic firing rate, of rat sympathetic neurons is 2.4-fold (Kullmann et al., 2016). This finding challenges the assumed 1:1 relay function of tSPNs and suggests that tSPNs amplify instead of relaying motor commands from the spinal cord.

Neurons can operate as integrators or coincidence detectors based on how they integrate synaptic inputs (König et al., 1996; Ratté et al., 2013). Integrators can summate temporally dispersed (i.e. asynchronous) inputs, whereas coincidence detectors only summate temporally coincident (i.e. synchronous) inputs. A previous study in mouse hippocampal neurons found that increased shunting, a likely consequence of strong excitatory synaptic input, in neurons with high I_M can switch the firing mode from integration to coincidence detection (Prescott et al., 2006). Synaptic inputs to vasculature-innervating tSPNs are entrained to the cardiac cycle, and recordings of action potentials generated by postganglionic sympathetic axons innervating muscles show tight cardiac rhythmicity (Springer et al., 2015; Macefield and Wallin, 2018), indicating that tSPNs transfer the temporal patterns of synaptic inputs to downstream targets, which may play an important role in regulating blood pressure. Future studies will examine the integrator and coincidence detector traits of NA2- and NA3-type tSPNs to see whether and how they differ in their ability to transfer temporal patterns of synaptic inputs.

3.4.4 Degenerate solutions and homeostatic regulation after SCI

Similar neural activities can be produced by multiple combinations of the underlying ion channel densities (Prinz et al., 2004), so instead of fitting one combination of ion channel densities each to NA2- and NA3-type tSPNs, we built a database to aggregate a collection of NA2- and NA3-type tSPN models, which enables a more rigorous and comprehensive examination of differences in their intrinsic excitability and capability to integrate synaptic inputs. This approach enables us to find that two NA2-type tSPNs receiving identical synaptic inputs and producing identical f-I curves differ in their underlying ion channel densities and in their ability to integrate *in vivo* synaptic inputs. Preliminary experimental data show that f-I curves of tSPNs six weeks after SCI were similar to those before SCI, suggesting that intrinsic excitability of tSPNs was either recovered or unchanged after SCI (Li, McKinnon and Hochman, personal communications). Our result indicates that the f-I curve as a measure of excitability has its limits, and tSPNs with similar f-I curves may still differ in their ability to integrate synaptic inputs. This insight would not be possible if we only fitted one parameter set each to NA2- and NA3-type tSPNs.

Degenerate solutions in each type of vasculature-innervating tSPNs were grouped by similarity of f-I curves. By quantifying the similarity of parameter sets within each degenerate group, we found that a tight regulation of I_M is needed to maintain f-I curve for both NA2- and NA3-type tSPNs, while most of the other ion channel densities are less constrained, indicating that tSPNs have a rich repertoire of tunable parameters to restore f-I curves after SCI. Preliminary data found increased I_{Kd} and I_{KCa} after SCI (Li, McKinnon and Hochman, personal communications), which matches our result. Our result also predicts that vasculature-innervating tSPNs exhibiting changes in either I_{Kd} or I_{leak} would be NA2-type tSPNs.

3.4.5 Future Direction: Elucidating intrinsic homeostatic plasticity mechanisms in tSPNs after SCI

tSPNs exhibit a rich repertoire of firing dynamics *ex vivo*. Our single neuron model can produce all the basic firing properties of tSPNs observed at hyperpolarized and depolarized current injections, such as "sag" conductance, rebound firing, and spike rate adaptation, etc. Some of the firing properties observed in experiments were not incorporated in this model. For example, repetitive firing led to a steadily increasing of an ultra-slow after-hyperpolarization (usAHP), which can hyperpolarize a cell membrane and reduce the reversal potential of K^+ (McKinnon et al., 2019). The time course of this usAHP is too long to be caused by I_M or I_{KCa}, and previous works indicate that it may be due to the activation of Na^+/K^+ -ATPase (Lees and Wallis, 1974; Picton et al., 2017). We did not integrate this phenomenon into our model because it was only observed in 2 out of 14 neurons tested and its functional relevance to SCI-induced changes was elusive. However, recent experiments observed increased usAHP in tSPNs after SCI, and found that usAHP can tune down tSPN excitability by increasing rheobase and reducing firing frequency (Li, McKinnon and Hochman, personal communications), which may help to prevent pain afferent induced hyperexcitabilty observed after SCI. Future work will implement and identify usAHP mechanisms in tSPNs.

Preliminary data also observed increased I_{Kd}, I_{KCa}, and a persistent inward current after SCI (Li, McKinnon and Hochman, personal communications), and therefore future work will first implement the persistent inward current in the tSPN model, and then conduct a thorough examination of all the tSPNs features I_{Kd}, I_{KCa}, and a persistent inward current influence. We will also re-run the brute force search with a wider search range of parameter values and finer search grid to examine the correlations between parameters.

3.4.6 Future direction: Determining factors that influence synaptic integration in tSPNs

Many factors influence tSPNs' ability to integrate synaptic inputs. One is the firing mode of the neuron, as discussed above. Another is the connectivity pattern between sympathetic preganglionic neurons in the spinal cord and tSPNs, which is assumed to follow the n + 1 rule.

The n+1 rule states that each postganglionic neuron receives one strong and suprathreshold input from the nearest preganglionic neuron, and several weak and sub-threshold inputs from preganglionic neurons originating in nearby segments. This rule was observed in the superior cervical and lumber SPNs (Karila and Horn, 2000; Rimmer and Horn, 2010), and therefore was assumed to dominate the synaptic recruitment at tSPNs. Future work will simulate synaptic inputs following the n + 1 rule with different number of sub-threshold inputs, and examine how the number of sub-threshold inputs influences synaptic gain in tSPNs.

The frequency and amplitude of synaptic inputs can also influence synaptic recruitment at tSPNs. Our collaborators have acquired preliminary data showing that the frequency and amplitude of the spontaneous synaptic events received by tSPNs increased six weeks after SCI. To examine whether these changes induce hyperexcitability in tSPNs after SCI, future work will simulate SCI-induced changes to synaptic inputs and see whether either type of the vasculature-innervating tSPNs becomes hyperexcitable.

Last but not least, changing ion channel densities or the correlations between ion channels can also affect synaptic integration. For example, in rat sympathetic neurons, increasing I_h using dynamic clamp led to enhanced synaptic integration (Kullmann et al., 2016). Another computational study found that balanced increase in I_A and I_h led to progressive decrease in the slope of the f-I curve (Burdakov, 2005). For both NA2- and NA3-type tSPNs, we will first characterize correlations between ion channels in each type, and then systematically vary each ion channel and correlation to see how they affect synaptic integration.

3.5 Acknowledgements

This work was supported by the CMBC Interdisciplinary Neuroscience Pilot Research Fund at Emory University and NIH grant 1R01NS102871. Parameter search was performed on the Neuroscience Gateway Portal (Sivagnanam et al., 2013).

Fig 3.2 to Fig 3.5 (except Fig 3.4C) were published in McKinnon et al., 2019, of which I am the second author and Michael McKinnon from the Hochman lab is the first author. I built the tSPN model and did the initial analysis for the work shown in these figures, while Michael McKinnon refined the analysis and made the final version of figures shown in the publication.

Chapter 4 General Discussion

Both the pyloric circuit in the crab *Cancer borealis* and the tSPNs in mice possess the ability to restore their neural activities after deafferentation, indicating that they are regulated by homeostatic plasticity mechanisms. In the pyloric circuit, the pyloric rhythm is disrupted after acute removal of all neuromodulatory inputs, but can recover 3-4 days later in the absence of neuromodulation. In the mouse tSPNs, preliminary data shows that the tSPNs' f-I curves are similar before and six weeks after SCI, indicating that neuronal excitability is maintained by homeostatic regulation. In Chapter 1, we reviewed homeostatic plasticity mechanisms in the context of degeneracy. Here, we discuss a few aspects of homeostatic plasticity mechanisms that are less relevant to degeneracy but fundamental to understand how homeostatic regulation works, which may eventually help us to understand how neurons and neural circuits employ their rich repertoire of degenerate solutions to restore neural activities after perturbations, both in the pyloric circuit and in tSPNs (Section 4.1 – 4.3). We then discuss a few future directions that may deepen our understanding of degeneracy in neurons and neural circuits (Section 4.4), followed by a zoom-out view on where this dissertation stands in the big picture (Section 4.5).

4.1 Homeostatic plasticity: tuners vs. targets

Homeostatic plasticity (HP) mechanisms have not only been observed in various animal models but also across multiple scales, ranging from the genetic to the neural network level. A parameter at the neuron level can be tuned to maintain activity at the neural network level, or become the target of maintenance by tuning its underlying mRNA expression levels. This can be confusing when examining HP mechanisms across different scales so we propose two concepts to resolve this ambiguity: tuners and targets. Roughly speaking, tuners are features of a single neuron or a neural circuit that are tuned/shifted during homeostatic regulation, and targets are features of a single neuron or a neural circuit that are maintained or restored by homeostatic regulation. For example, in cultured hippocampal networks, the balance between excitatory and inhibitory inputs, i.e. E/I ratio, was transiently decreased but returned to the baseline level two days after perturbation, in which case the E/I ratio appears to be a target of homeostatic regulation (Slomowitz et al., 2015). In rat visual cortex, however, E/I ratio increased to compensate for reduced firing rate caused by intraocular TTX injection, in which case the E/I ratio behaves like a tuner (Maffei and Turrigiano, 2008). Tuners can be distinguished from targets based on monotonic vs. non-monotonic change after perturbations. For example, if a feature shows monotonic change after perturbations, like the increase of E/I ratio to compensate for visual deprivation in rat visual cortex, it is defined as a tuner. On the other hand, if a feature shows non-monotonic change, either increasing first then decreasing, or decreasing first then increasing, it is a target that is maintained by homeostatic regulation.

At a single neuron level, changes in neuronal excitability can be characterized by various passive and active membrane properties, each can function as a tuner of homeostatic regulation. Common passive membrane properties are input resistance and the resting membrane potential (Grashow et al., 2010), and conductances and reversal potentials of individual ionic currents are the common active membrane properties (Golowasch, 2014; Marder, 2015). Changes in the current kinetics caused by perturbations, like gating variables and time constants, have also been observed, but occur less commonly (Thoby-Brisson and Simmers, 2002). A type of tuner that has been examined extensively in the stomatogastric nervous system in the crab *Cancer borealis* are the linear ratios between ion channel densities, i.e. ion channel correlations. These correlations have been observed at both mRNA and maximum conductance levels (MacLean et al., 2003; 2005; Khorkova and Golowasch, 2007; Ransdell et al., 2012; Zhao and Golowasch, 2012; Temporal et al., 2014), and they are often cell type-specific (Schulz et al., 2006; 2007; Hudson and Prinz, 2010). A theoretical study indicates that ion channel correlations can emerge from activity-dependent homeostatic tuning rules (O'Leary et al., 2013), and a recent experimental study proposes that ion channel correlations can stabilize neuronal activity while allowing conductances to change over wide ranges to compensate for perturbations (Zhao and Golowasch, 2012), all suggesting that neuronal excitability can be maintained by tuning ion channel correlations .

At the synaptic level, two widely identified tuners of HSP mechanisms are amplitude and frequency of miniature excitatory or inhibitory post-synaptic currents (mEPSC or mIPSC). HSP can occur both locally at a single synapse or globally across multiple synapses. The latter is called synaptic scaling, because the strengths of all synaptic inputs are scaled up or down to restore postsynaptic neural activity (Turrigiano et al., 1998; Soto-Treviño et al., 2001). Although most often changes of amplitude or frequency are monotonic, biphasic change of mean mEPSC amplitude was observed in the visual cortex of rats (Hengen et al., 2013; Lambo and Turrigiano, 2013). In general, increased mEPSC amplitude indicates a higher density/conductance of postsynaptic receptors, whereas higher frequency is often associated with increased presynaptic release probability or increased number of functional synaptic connections (Malenka and Nicoll, 1997; O'Brien et al., 1998; Kirov and Harris, 1999; Murthy et al., 2001; Queenan et al., 2012). An exception is that increased number of functional synapses by activating silent synapses could be caused either by an increase in the number of release sites (i.e. presynaptic unsilencing) or by an increase in the number of functional postsynaptic units (i.e. postsynaptic unsilencing) (Malenka and Nicoll, 1997; Kerchner and Nicoll, 2008; Queenan et al., 2012). Therefore, both pre- and postsynaptic events could induce higher mEPSC frequency. E/I ratio can either be a tuner or a target of homeostatic regulation, depending on the examined animal model and perturbation paradigms, as discussed above.

Targets of homeostatic plasticity mechanisms are quite similar at a single neuron and circuit level. For a spiking neuron or network consisting of spiking neurons, common targets are average firing rate, inter-spike interval distribution, etc. (Grashow et al., 2010; Hengen et al., 2013). For a bursting neuron or a central pattern generator consisting of bursting neurons, targets could be period, duty cycle, spikes per burst, and phase relationships, etc. (Golowasch, 2014). What the targets of homeostatic regulation are is a question rooted in the debate of whether information in the nervous system is coded by the firing rate or by spike timing (Gautrais and Thorpe, 1998). From the rate coding perspective, information is coded in the average firing rate of individual neurons or populations of neurons. Sometimes it is the firing rate distribution, defined by both the average firing rate and the variance, that encodes information (Triesch, 2007). Accordingly, when pathological perturbation occurs, firing rate or firing rate distribution should be maintained by homeostatic regulation. On the other hand, from the temporal coding perspective, the precise time of each spike encodes information (VanRullen et al., 2005; Butts et al., 2007), and therefore the firing pattern of the neural circuit should be maintained (Cudmore et al., 2010). Firing pattern refers to neural firing properties like inter-spike interval for spiking neurons, duty cycle for bursting neurons, and/or phase relationships for neural network synchrony. Firing rate and firing pattern codes are not mutually exclusive; they could both encode information in the same neural circuit and therefore could be both tightly regulated in face of perturbations. Clarifying what is being restored during a homeostatic tuning process is important for placing that process in the broader context of homeostatic plasticity mechanisms. Overall, researchers need to be open to the possibility that not only the firing rate, but also other firing properties like ISI distribution of a spiking neuron, duty cycle of a bursting neuron, and firing rate distribution, could be the targets of homeostatic regulation.

4.2 Homeostatic plasticity mechanisms: activity-dependent vs. activity-independent

A common basis that may support both intrinsic and synaptic homeostatic plasticity is an activity-dependent mechanism. Both experimental and theoretical studies have shown that an activity-dependent mechanism, with intracellular calcium concentration as the activity sensor, is sufficient to restore neural activities after perturbations (LeMasson et al., 1993; Turrigiano et al., 1994; Liu et al., 1998; Turrigiano et al., 1998). In the crab *Cancer borealis*, removal of all neuromodulators disrupts the pyloric rhythm, but the rhythm can recover in the absence of neuromodulators a few days later, and simulations showed that activity-dependent regulation of ionic currents of pyloric circuit neurons underlie this rhythm recovery (LeMasson et al., 1993; Golowasch et al., 1999; Thoby-Brisson and Simmers, 2002). A study conducted in cortical neuronal cultures explicitly showed that synaptic scaling was rapidly induced by blocking postsynaptic firing, but not by local synaptic blockade, suggesting that synaptic scaling depended on neural activity, but not neuromodulation (Ibata et al., 2008).

On the other hand, experimental studies in both invertebrate and vertebrate neural systems also suggest the existence of activity-independent mechanisms of homeostatic regulation. In the stomatogastric nervous system of the lobster *Panulirus interruptus*, overexpression of a *shal* gene that encodes a transient potassium current (I_A) was compensated by up-regulation of a hyperpolarization-activated inward current (I_h). This compensation also occurred in response to overexpression of a nonfunctional mutant version of *shal* that did not lead to increased amplitude of I_A, implying the existence of an activity-independent mechanism (MacLean et al., 2003; 2005). A recent study in cortical neuronal cultures blocked AMPAergic transmission while using optogenetic feedback to restore neural spiking, and found that AMPAergic activity blockade alone could induce synaptic scaling, suggesting that activity-independent mechanisms also exist in the mammalian nervous system (Fong et al., 2015). Activity-independent homeostatic regulation was also observed at the synaptic level, which appears to be triggered and expressed locally at the dendritic sites of the synapse being perturbed (Gonzalez-Islas et al., 2018). A Hodgkin-Huxley computational model of the PD neuron in the pyloric circuit of the crab *Cancer borealis* showed that activity-dependent and neuromodulator-dependent mechanisms together could reproduce key features of the pyloric rhythm recovery observed *in vitro* that were missing in a solely activity-dependent model (Zhang and Golowasch, 2011). Besides neuromodulation, extracellular matrix was also found to modulate homeostatic plasticity mechanisms. A recent study in the pyloric circuit of the crab *Cancer borealis* showed that degradation of an extracellular matrix component called chondroitin sulfate proteoglycans (CSPGs) before decentralization would delay the onset of rhythm recovery (Hudson et al., 2015). A biologically plausible model demonstrated that extracellular matrix could maintain firing rate homeostasis through adjusting both synaptic inputs and neuronal spike generation (Kazantsev et al., 2012). Together, these studies show that homeostatic plasticity mechanisms are regulated by both neural activity and neuromodulation, and modulated by other factors like extracellular matrix.

4.3 **Homeostatic plasticity and mathematical theory**

Control theory is a mathematical theory that employs feedback loops to precisely control a behavior or process by constantly calculating and minimizing the error between observed output and target output. Several excellent reviews have discussed the link between homeostatic regulation and control theory (Davis, 2006; O'Leary and Wyllie, 2011; Queenan et al., 2012), and most of the biophysical models that implement the activity-dependent homeostatic regulation of ion channel densities naturally fit in the control theory framework (Günay and Prinz, 2010; Olypher and Prinz, 2010). One way to integrate both intrinsic and synaptic homeostatic plasticity mechanisms in the control theory framework is that two feedback signals could independently regulate the synaptic input and neuronal spiking (Kazantsev et al., 2012). Feedback signals are implemented based on feedback controllers, and a recent review provides a broad collection of feedback controllers that can be applied to neuroscience (Grosenick et al., 2015). One problem with control theory is that it assumes that the neural circuit implicitly “knows” the target neural activity level, which is usually represented by a set point of intracellular calcium concentration, yet the physiological foundation of this set point is still vague (O'Leary and Wyllie, 2011). A recent computational study proposed that the “set point" of intracellular calcium concentration can be derived from central dogma. Specifically, the target intracellular calcium concentration level could be the ratio of the degradation rate and synthesis rate of some Ca^{2+}-sensitive enzyme complex (O'Leary et al., 2014).

Another mathematical theory that can be applied to analyze HP mechanisms is information theory. Information theory puts HP in the context of optimizing information transmission and/or representation, which is more about the "why" rather than the "how" of HP mechanisms. Optimizing information transmission is equivalent to maximizing mutual information, a measure of the amount of information one variable contains about another variable. For example, in a computational study, coordinated HIP and HSP mechanisms were shown to regulate the mean and variance of a firing rate distribution, respectively, through maximizing mutual information between neuronal input and output (Cannon and Miller, 2016). Examining HP in the context of f-I curves, a common method to quantify input-output relationships, can also help elucidate the relationships between HIP and HSP. For example, Turrigiano proposed that by scaling the strength of all the neuron's incoming synapses up or down (i.e. synaptic scaling), a neuron's firing response can be shifted up or down its f-I curve. In contrast, regulation of intrinsic plasticity changes the sensitivity of a neuron's response to synaptic inputs, and therefore shifts the f-I curve leftward (i.e. the neuron will fire less for a given level of synaptic drive) or rightward (i.e. it will fire more for a given level of synaptic drive) along the input axis (Turrigiano and Nelson, 2000).

4.4 **Future directions on degeneracy in neurons and neural circuits**

Much progress has been made toward identifying and characterizing structures of degenerate parameter sets and to relate them to functions of neurons and neural circuits. But like with all interesting questions, this progress also begets more questions yet to be explored. Below, we briefly discuss two questions that may further expand our understanding of degeneracy in neurons and neural circuits.

4.4.1 Defining measures of degeneracy

To compare degenerate parameter sets at different time points during homeostatic regulation and across preparations, we first need to define measures that can quantify degeneracy. Degeneracy is qualitatively defined as combinations of parameters that give rise to similar neural activity or behavior. But how similar is sufficient to be deemed as functionally equivalent? Is a system more degenerate because it has more parameters or because it has more degenerate parameter sets? Some attempts at quantifying degeneracy have been made using information theoretical concepts (i.e. mutual information and entropy) (Tononi et al., 1999; Man et al., 2016), but measures that can be implemented to analyze experimental data are yet to be developed.

Defining measures of degeneracy is challenging partially because degenerate systems usually contain a large amount of parameters that overlap in their functionality, making it difficult to quantify the effect of individual parameter on the function of neurons and neural circuits. The mathematician John von Neumann once said: “With four parameters I can fit an elephant, and with five I can make him wiggle his trunk.” Mathematicians and physicists have a taste for simple, elegant solutions, but if we not only want to model the mechanistic wiggle of the elephant’s trunk, but also how it lives, how it ages, how it thinks, and how it feels, the number of parameters needed quickly explodes. The computational model developed in Chapter 3, for example, needs eight types of ion channels to explain the basic firing properties of tSPNs, and therefore has at least eight parameters to tune. Fortunately, real data usually contain correlations and dependencies, which forms lower-dimensional structures in the high-dimensional parameter space. Our findings in Chapter 2 show that we can quantify the change of the lower-dimensional structures in response to perturbations or constraints, which may provide insight on how to quantify degeneracy later.

Therefore, to develop measures of degeneracy, we first need to better understand how multiple cellular and synaptic parameters change in response to perturbations on various timescales, ranging from seconds to days. This is challenging to do in experiments, but can be tackled by combining experiments and computational methods. It is feasible to monitor neural activities of hundreds of neurons cultured on a high-density multi-electrode array (Panas et al., 2015; Slomowitz et al., 2015) or activities of a neural circuit *in vitro* for days (Goaillard et al., 2009). Analyzing the space of all possible models instead of a single model that matches an experimental dataset would provide us a more comprehensive and deeper understanding of degenerate systems (Gao and Ganguli, 2015).

4.4.2 Degeneracy and robustness against injuries

Degenerate systems possess the flexibility to restore neural activities against a wide range of perturbations and injuries. A computational study in the pyloric circuit found that degenerate solutions made the system more robust to temperature perturbations (Caplan et al., 2014). Preliminary data show that tSPNs exhibit similar f-I curves before and six weeks after SCI, but the amplitude of I_{Kd}, I_{KCa}, and a persistent inward current increased (Li, McKinnon and Hochman, personal communications). Our simulation also confirmed that similar f-I curves can be generated from different parameter sets, and further found that degenerate parameter sets can differ in their ability to integrate synaptic inputs. This result indicates that switching between degenerate solutions can tune up or down tSPNs' ability to integrate synaptic inputs while maintaining neuronal excitability (measured by f-I curves), and therefore may make tSPNs more robust to SCI-induced changes. However, it is still unclear how neurons and neural circuits explore and exploit the degenerate solutions, especially the linear and nonlinear structures of them, to restore neural activities after injuries and perturbations. Several computational studies have shown that degenerate solutions do not respond to the same perturbation in an identical manner (Marder and Taylor, 2011; O'Leary et al., 2014), but why some are more susceptible to perturbations than others is still unknown. One possibility is that degenerate parameter sets that are more susceptible to perturbations lie near boundaries between regions of parameter space where the neuron or neural circuit switches from excitable to hyperexcitable state (Ratté et al., 2014; Ratté and Prescott, 2016). A deeper understanding of both linear and nonlinear structures of degenerate solutions would help us answer those questions.

In the meantime, we are aware that our models in Chapter 2 and 3 do not contain any homeostatic tuning rules discussed in section 4.2, and implementing homeostatic regulation of ion channel densities in these models may further constrain the pool of degenerate solutions.

4.5 Final thoughts

The human brain contains about 100 billion neurons, varying by its genetic, anatomical, and biophysical constructions. Can we expect to find two identical neurons in a human brain? It seems very unlikely. Variability in parameters has been observed across all scales in the brain. At the genetic level, recent studies suggest that neurons can contain different copies of the genome, which mutated and diverged during development (McConnell et al., 2017). At the biophysical level, two neurons in the same brain region may contain different types of ionic currents, and each type of ionic currents may be composed of different sub-types. Even if two neurons have the identical composition of ion channels, each ion channel density can vary in a 3-4 fold range (Schulz et al., 2006; 2007; Wilhelm et al., 2009). Cell morphologies can also vary by cell size, by shape, and by branching patterns of dendrites. Moreover, cell size and molecular composition constantly change during development.

Although it is unlikely that two neurons are identical, neurons in the same brain region tend to be functionally equivalent. So to what extent does the individuality or uniqueness of a single neuron matter? Or does the functional unit of the brain lie in the overlapping structures of neurons sharing similar functionality? At one end of the spectrum, we have the "grandma neuron" that fires only when the subject sees a very particular image of his or her grandmother. If each neuron in the brain fires only when specific faces or objects present, then according to the psychologist Fred Attneave, the volume of our brain needs to be measured in the unit of cubic light years (Attneave, 1954). Besides the explosion of volume, encoding information in a highly specific manner is not only inefficient, but also very fragile to both predictable perturbations like aging and unpredictable perturbations like injuries and extreme environmental conditions. At the other end of the spectrum, we have seen degeneracy in neurons and neural circuits, where neurons or neural circuits with different combination of ionic current densities and synaptic strengths show similar functionality. Studies have also found that neurons with different morphologies behave similarly (Otopalik et al., 2017; 2019). Degeneracy has been observed across all scales of neuroscience, from different codons encoding the same amino acid at the genetic level, to multiplicity of neural pathways and muscle configurations that can reach the same target at the motor control level. All of the above indicate that degeneracy is an essential coding strategy of the brain, and enables us to code vast amounts of information in a brain that weighs just about a pound. But a fully overlapping coding strategy is also inefficient, which poses questions like what is the optimal level of overlap, what are the optimal structures of overlapping, and how does the brain employ the overlapping structures to cope with perturbations. Examination of structures of degenerate parameter sets is a baby step towards solving these puzzles, while many great challenges and opportunities are awaiting us ahead.

5. Appendix

5.1 Equations for pyloric circuit model

Fast sodium current:

$$m_\infty = \frac{1}{\left(1+e^{\frac{-(V+25.5)}{5.29}}\right)} \qquad h_\infty = \frac{1}{1+e^{\frac{V+48.9}{5.18}}}$$

$$\tau_m = 2.64 - \frac{2.52}{1+e^{\frac{-(V+120)}{25}}} \qquad \tau_h = \frac{1.34}{1+e^{\frac{V+62.9}{10}}} \cdot \left(1.5 + \frac{1}{1+e^{\frac{V+34.9}{3.6}}}\right)$$

$$\frac{dm}{dt} = \frac{m_\infty - m}{\tau_m} \qquad \frac{dh}{dt} = \frac{h_\infty - h}{\tau_h}$$

$$I_{Na} = G_{Na} \cdot m^3 h \cdot (V - E_{Na})$$

Delayed rectifier potassium current:

$$h_\infty = \frac{1}{1+e^{\frac{-(12.3+V)}{11.8}}}$$

$$\tau_h = 14.4 - \frac{12.8}{1+e^{\frac{-(V+28.3)}{19.2}}}$$

$$\frac{dh}{dt} = \frac{h_\infty - h}{\tau_h}$$

$$I_K = G_K \cdot h^4 \cdot (V - E_K)$$

S-type calcium current:

$$m_\infty = \frac{1}{1+e^{\frac{-(V+33)}{8.1}}} \qquad h_\infty = \frac{1}{1+e^{\frac{V+60}{6.2}}}$$

$$\tau_m = 2.8 + \frac{14}{e^{\frac{V+27}{10}}} + e^{\frac{-(V+70)}{13}} \qquad \tau_h = 120 + \frac{300}{e^{\frac{V+55}{9}}} + e^{\frac{-(V+65)}{16}}$$

$$\frac{dm}{dt} = \frac{m_\infty - m}{\tau_m} \qquad \frac{dh}{dt} = \frac{h_\infty - h}{\tau_h}$$

$$I_{CaS} = G_{CaS} \cdot m^3 h \cdot (V - E_{Ca})$$

T-type calcium current:

$$m_\infty = \frac{1}{1 + e^{\frac{-(V+27.1)}{7.2}}}$$

$$h_\infty = \frac{1}{1 + e^{\frac{V + 32.1}{5.5}}}$$

$$\tau_m = 43.4 - \frac{42.6}{1 + e^{\frac{-(V+68.1)}{20.5}}}$$

$$\tau_h = 210 - \frac{179.6}{1 + e^{\frac{-(V+55)}{16.9}}}$$

$$\frac{dm}{dt} = \frac{m_\infty - m}{\tau_m}$$

$$\frac{dh}{dt} = \frac{h_\infty - h}{\tau_h}$$

$$I_{CaT} = G_{CaT} \cdot m^3 h \cdot (V - E_{Ca})$$

Calcium-dependent potassium current:

$$m_\infty = \frac{[Ca^{2+}]}{[Ca^{2+}]+3} \cdot \frac{1}{1 + e^{\frac{-(V+28.3)}{12.6}}}$$

$$\tau_m = 180.6 - \frac{150.2}{1 + e^{\frac{-(V+46)}{22.7}}}$$

$$\frac{dm}{dt} = \frac{m_\infty - m}{\tau_m}$$

$$I_{KCa} = G_{CaS} \cdot m^4 \cdot (V - E_K)$$

A-type potassium current:

$$m_\infty = \frac{1}{1 + e^{\frac{-(V+27.2)}{8.7}}}$$

$$h_\infty = \frac{1}{1 + e^{\frac{V + 56.9}{4.9}}}$$

$$\tau_m = 23.2 - \frac{20.8}{1 + e^{\frac{-(V+32.9)}{15.2}}}$$

$$\tau_h = 77.2 - \frac{58.4}{1 + e^{\frac{-(V+38.9)}{26.5}}}$$

$$\frac{dm}{dt} = \frac{m_\infty - m}{\tau_m}$$

$$\frac{dh}{dt} = \frac{h_\infty - h}{\tau_h}$$

$$I_A = G_A \cdot m^3 h \cdot (V - E_K)$$

Hyperpolarization-activated mixed ion current:

$$m_\infty = \frac{1}{1 + e^{\frac{-(V+75)}{5.5}}}$$

$$\tau_m = \frac{2}{e^{\frac{-(V+169.7)}{11.6}}} + e^{\frac{V-26.7}{14.3}}$$

$$\frac{dm}{dt} = \frac{m_\infty - m}{\tau_m}$$

$$I_h = G_h \cdot m \cdot (V - E_h)$$

Leak current:

$$I_{leak} = G_{leak} \cdot (V - E_{leak})$$

Modulation-activated inward current:

$$m = \frac{1}{1 + e^{0.2\cdot(-V-55)}}$$

$$I_{MI} = G_{MI} \cdot m \cdot (V - E_{MI})$$

Synaptic current:

$$s_\infty = \frac{1}{1 + e^{\frac{V_{th} - V_{pre}}{\Delta V}}}, \; V_{th} = -35\ mV,\ \Delta V = 5\ mV$$

$$\tau_s = k \cdot (1 - s_\infty), \; k_{Glu} = 0.025\ ms,\ k_{ACh} = 0.01\ ms$$

$$\frac{ds}{dt} = \frac{s_\infty - s}{\tau_s}$$

5.2 Equations for single neuron model of tSPNs

Fast sodium current:

$$\alpha_m = 0.36 \cdot \frac{V + 33}{1 - e^{\frac{-(V+33)}{3}}} \qquad \alpha_h = -0.1 \cdot \frac{V + 55}{1 - e^{\frac{-(V+55)}{6}}}$$

$$\beta_m = -0.4 \cdot \frac{V + 42}{1 - e^{\frac{-(V+42)}{20}}} \qquad \beta_h = \frac{4.5}{1 + e^{\frac{-V}{10}}}$$

$$\tau_m = \frac{2}{\alpha_m + \beta_m} \qquad \tau_h = \frac{2}{\alpha_h + \beta_h}$$

$$m_\infty = \frac{\alpha_m}{\alpha_m + \beta_m} \qquad h_\infty = \frac{\alpha_h}{\alpha_h + \beta_h}$$

$$\frac{dm}{dt} = \frac{m_\infty - m}{\tau_m} \qquad \frac{dh}{dt} = \frac{h_\infty - h}{\tau_h}$$

$$I_{Na} = G_{Na} \cdot m^2 h \cdot (V - E_{Na})$$

Delayed rectifier potassium current:

$$\alpha_n = 0.0047 \cdot \frac{\mathrm{V} + 12}{1 - \mathrm{e}^{\frac{-(\mathrm{V}+12)}{12}}}$$

$$\beta_n = e^{\frac{-(V+147)}{30}}$$

$$\tau_n = \frac{1}{\alpha_n + \beta_n}$$

$$n_\infty = \frac{\alpha_n(V-20)}{\alpha_n(V-20)+\beta_n(V-20)}$$

$$\frac{dn}{dt} = \frac{n_\infty - n}{\tau_n}$$

$$I_K = G_K \cdot n^4 \cdot (V - E_K)$$

L-type calcium current:

$$\alpha_m = \frac{7.5}{1 + e^{\frac{-(V-13)}{7}}} \qquad \alpha_h = \frac{0.0068}{1 + e^{\frac{V + 30}{12}}}$$

$$\beta_m = \frac{1.65}{1 + e^{\frac{V-14}{4}}} \qquad \beta_h = \frac{0.006}{1 + e^{\frac{-V}{11}}}$$

$$\tau_m = \frac{1}{\alpha_m + \beta_m} \qquad \tau_h = \frac{1}{\alpha_h + \beta_h}$$

$$m_\infty = \frac{\alpha_m}{\alpha_m + \beta_m} \qquad h_\infty = \frac{\alpha_h}{\alpha_h + \beta_h}$$

$$\frac{dm}{dt} = \frac{m_\infty - m}{\tau_m} \qquad \frac{dh}{dt} = \frac{h_\infty - h}{\tau_h}$$

$$I_{CaL} = G_{CaL} \cdot mh \cdot (V - E_{Ca})$$

M-type potassium current:

$$\tau_m = \frac{2000}{3.3 \cdot \left(e^{\frac{V+35}{40}} + e^{\frac{-(V+35)}{20}}\right)}$$

$$m_\infty = \frac{1}{1 + e^{\frac{-(V+35)}{10}}}$$

$$\frac{dm}{dt} = \frac{m_\infty - m}{\tau_m}$$

$$I_M = G_M \cdot m^2 \cdot (V - E_K)$$

Calcium-dependent potassium current:

$$\tau_m = \frac{50}{1 + [Ca^{2+}]^2}$$

$$m_\infty = \frac{[Ca^{2+}]^2}{[Ca^{2+}]^2 + 1}$$

$$\frac{dm}{dt} = \frac{m_\infty - m}{\tau_m}$$

$$I_{KCa} = G_{KCa} \cdot m \cdot (V - E_K)$$

A-type potassium current:

$$\tau_m = 0.3632 + \frac{1.158}{1 + e^{\frac{V + 55.96}{20.12}}}$$

$$\tau_h = 0.124 + \frac{2.678}{1 + e^{\frac{V + 50}{16.027}}}$$

$$m_\infty = \left(0.0761 \cdot \frac{e^{\frac{V + 94.22}{31.84}}}{1 + e^{\frac{V + 1.17}{28.93}}}\right)^{1/3}$$

$$h_\infty = \left(\frac{1}{1 + e^{0.069(V+53.3)}}\right)^4$$

$$\frac{dm}{dt} = \frac{m_\infty - m}{\tau_m}$$

$$h_\infty = \frac{h_\infty - h}{\tau_h}$$

$$I_A = G_A \cdot m^3 h \cdot (V - E_K)$$

Hyperpolarization-activated current:

$$\tau_m = \frac{\tau_0}{cosh\left(\frac{V + 80}{13.5}\right)}, \tau_0 = 1000\, ms$$

$$m_\infty = \frac{1}{1 + e^{\frac{V + 75}{5.5}}}$$

$$\frac{dm}{dt} = \frac{m_\infty - m}{\tau_m}$$

$$I_h = G_h \cdot m \cdot (V - E_h)$$

Leak current:

$$I_{leak} = G_{leak} \cdot (V - E_{leak})$$

Synaptic current:

$$g_{syn}(t) = s \cdot \left(e^{-t/_{15}} - e^{-t/_{1}}\right)$$

$$I_{syn} = \sum_{i=1}^{n} A_i \cdot g_{syn}(t - t_i) \cdot \left(V - E_{syn}\right)$$

Intracellular calcium dynamics:

$$\frac{d[Ca^{2+}]}{dt} = 0.01 \cdot (-0.002 \cdot I_{CaL} - 0.024 \cdot [Ca^{2+}])$$

5.3 Supplemental data: Distribution of each parameter before and after I_{MI} removal

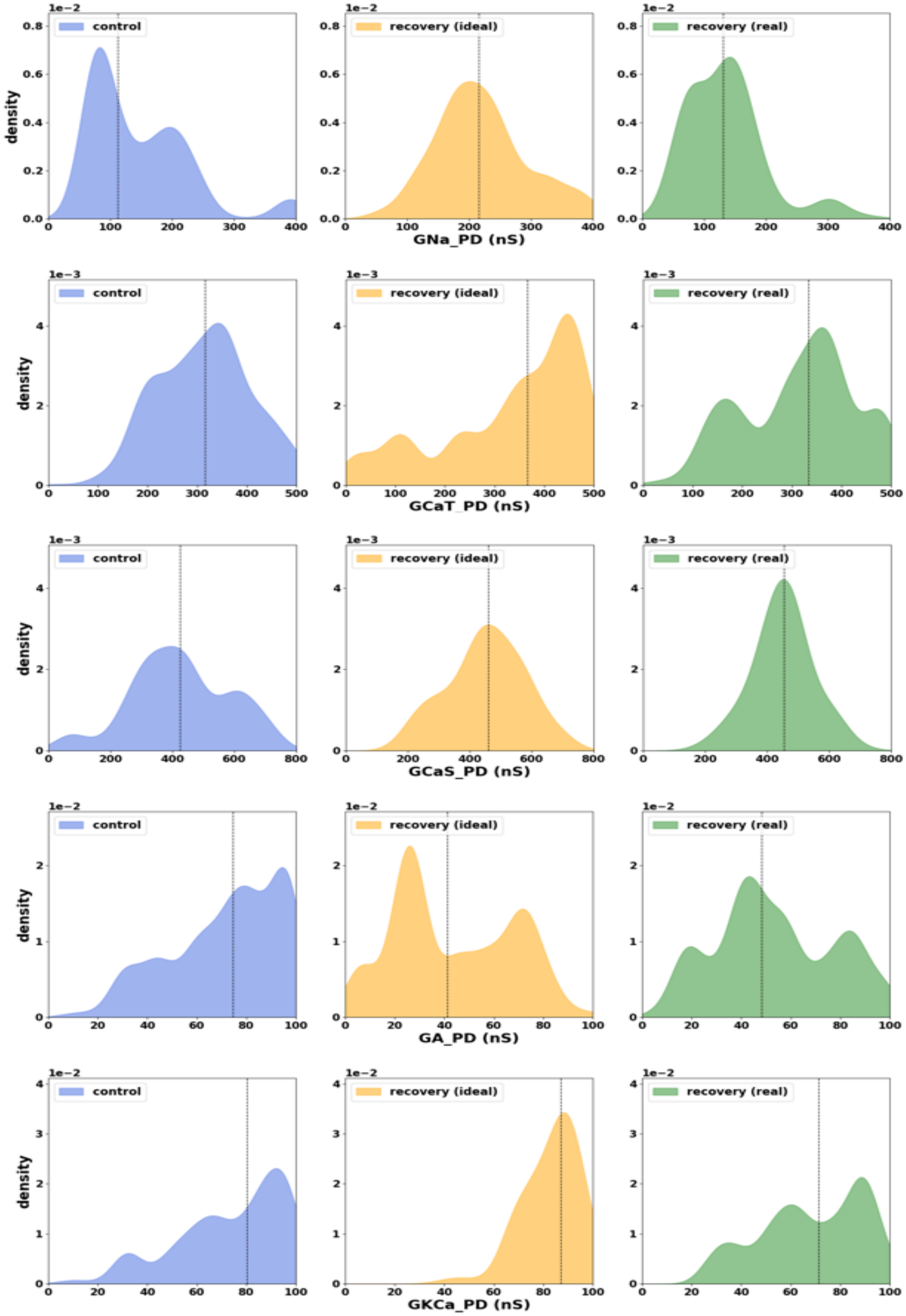

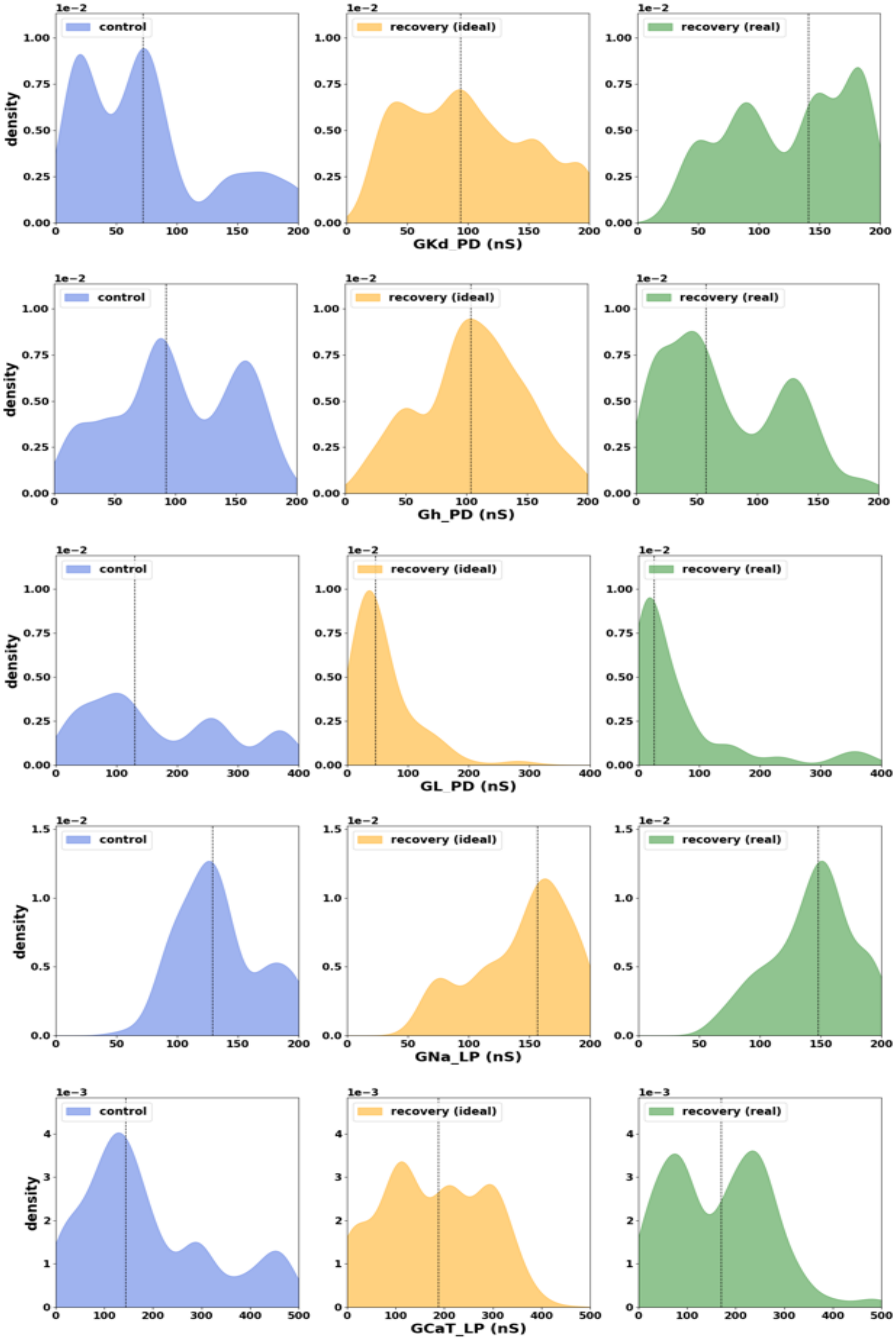
1e−2
control
recovery (ideal)
recovery (real)
density
1.00
0.75
0.50
0.25
0.00
0
50
100
150
200
GKd_PD (nS)
Gh_PD (nS)
GL_PD (nS)
300
400
1.5
1.0
0.5
0.0
GNa_LP (nS)
1e−3
4
3
2
1
0
500
GCaT_LP (nS)

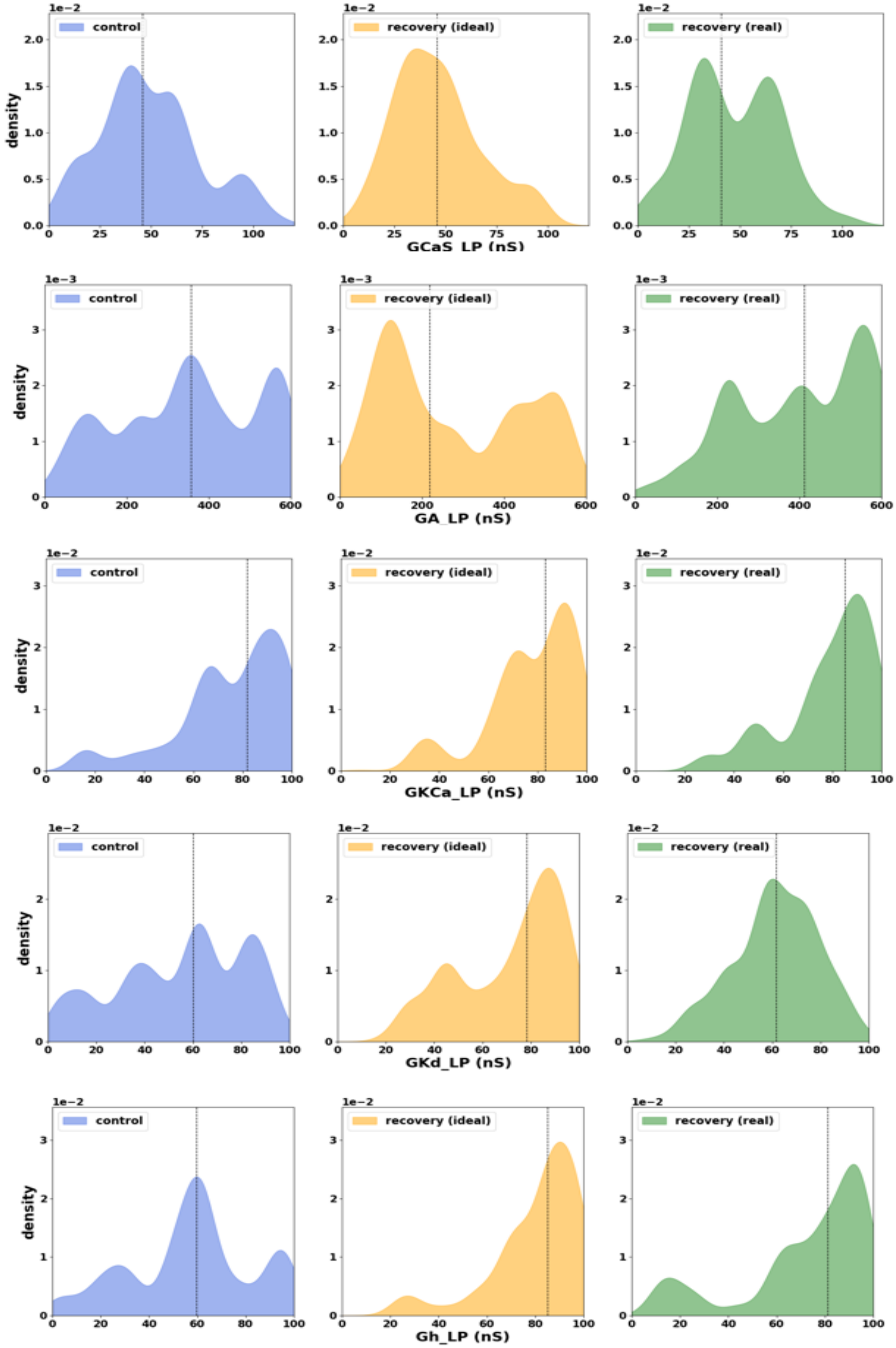
control
recovery (ideal)
recovery (real)
density
1e−2
1e−3
GCaS_LP (nS)
GA_LP (nS)
GKCa_LP (nS)
GKd_LP (nS)
Gh_LP (nS)

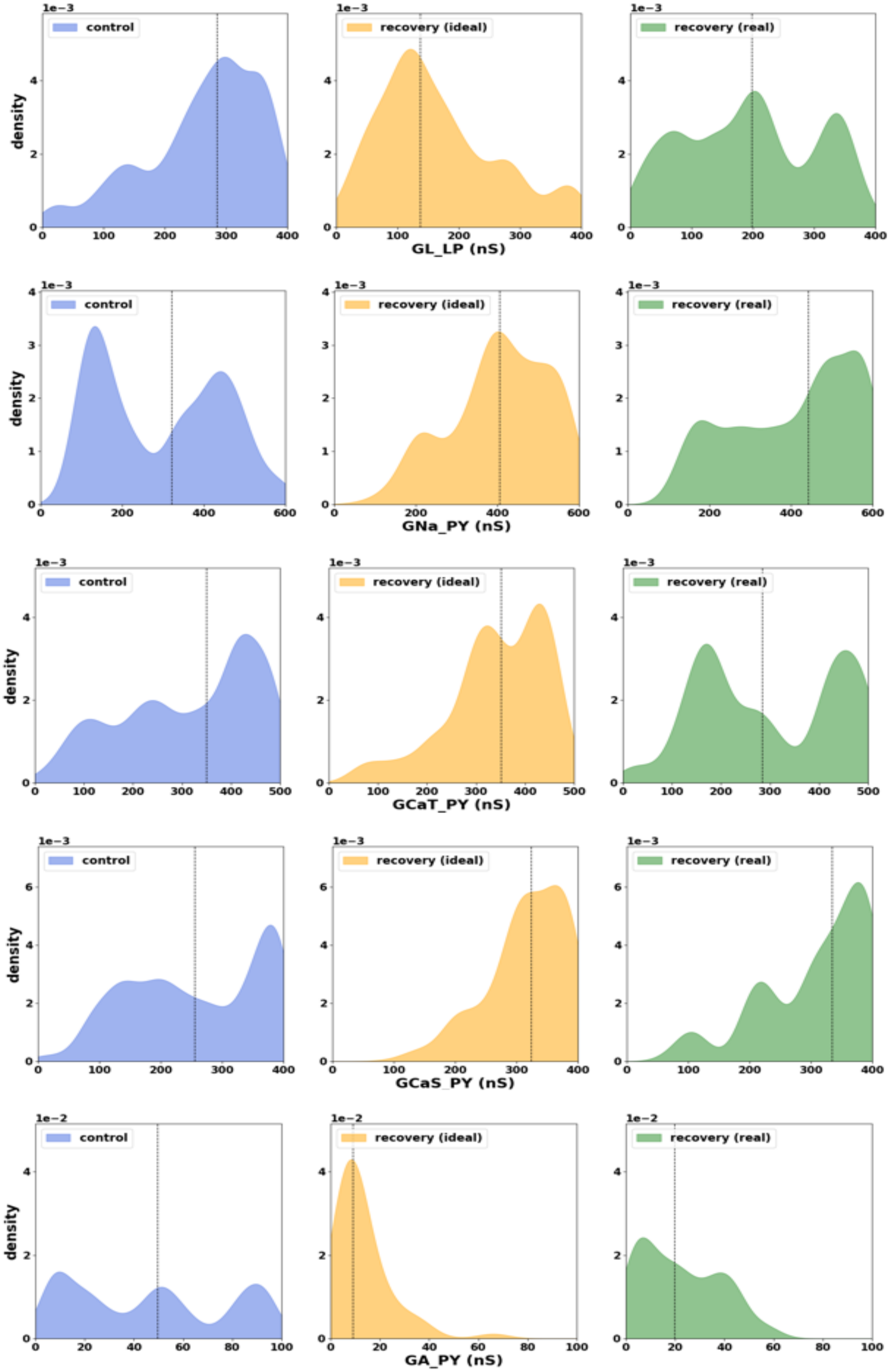
1e−3
control
recovery (ideal)
recovery (real)
density
0
2
4
100
200
300
400
GL_LP (nS)
1e−3
0
1
2
3
4
600
GNa_PY (nS)
1e−3
500
GCaT_PY (nS)
1e−3
6
GCaS_PY (nS)
1e−2
20
40
60
80
100
GA_PY (nS)

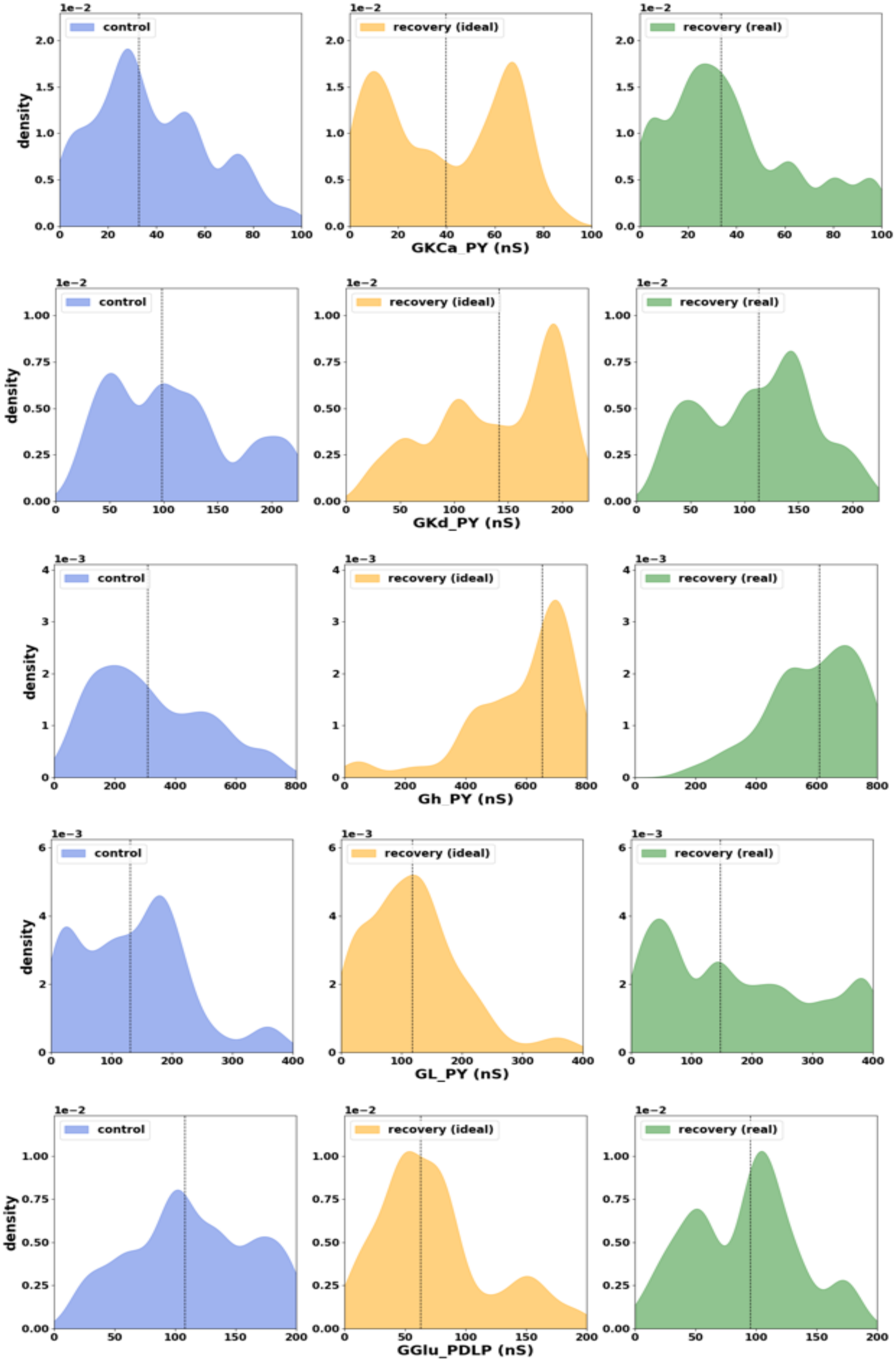
1e−2
control
recovery (ideal)
recovery (real)
density
GKCa_PY (nS)
1e−2
control
recovery (ideal)
recovery (real)
density
GKd_PY (nS)
1e−3
control
recovery (ideal)
recovery (real)
density
Gh_PY (nS)
1e−3
control
recovery (ideal)
recovery (real)
density
GL_PY (nS)
1e−2
control
recovery (ideal)
recovery (real)
density
GGlu_PDLP (nS)

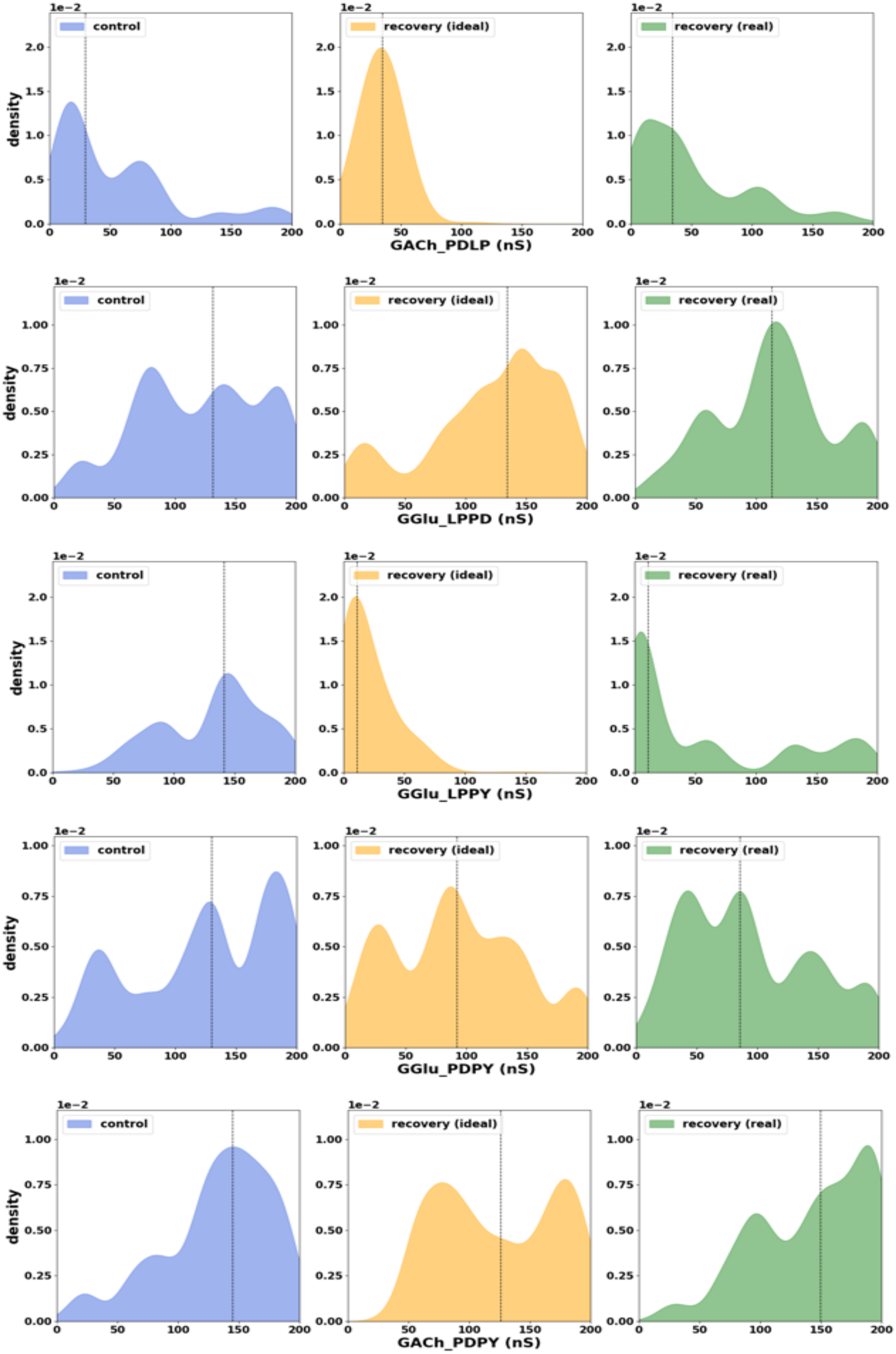
1e−2
control
recovery (ideal)
recovery (real)
density
0.0
0.5
1.0
1.5
2.0
0
50
100
150
200
GACh_PDLP (nS)
0.00
0.25
0.50
0.75
1.00
GGlu_LPPD (nS)
GGlu_LPPY (nS)
GGlu_PDPY (nS)
GACh_PDPY (nS)

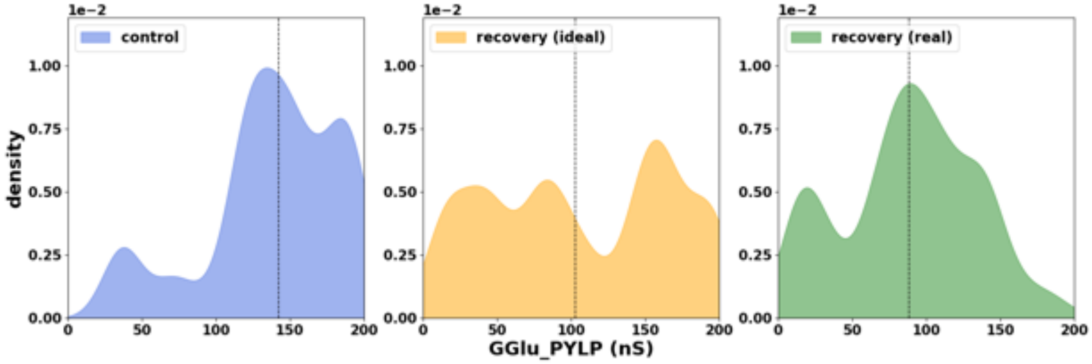

Figure 5.1 Distribution of each cellular or synaptic parameter in the pyloric circuit model before and after I_{MI} removal. Distributions are smoothed by kernel density estimation. Blue: Control. Yellow: Recovery (ideal). Green: Recovery (real). Dotted vertical line: median of the distribution.

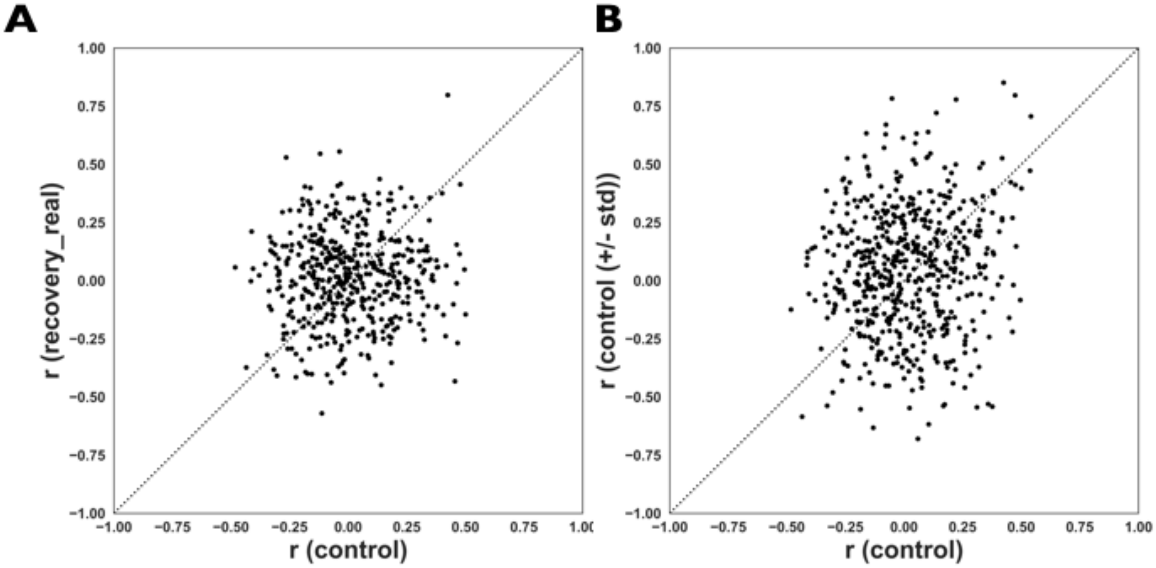

Figure 5.2 Scatter plot of ion channel correlations before and after applying constraints. (A) Ion channel correlations from the "Control" vs. the "Recovery (real)" datasets. **(B)** Ion channel correlations from the "Control" vs. the "Control (+/- std)" datasets. Dotted line: identical line.

5.4 Supplemental data: Ion channel correlations in tSPNs

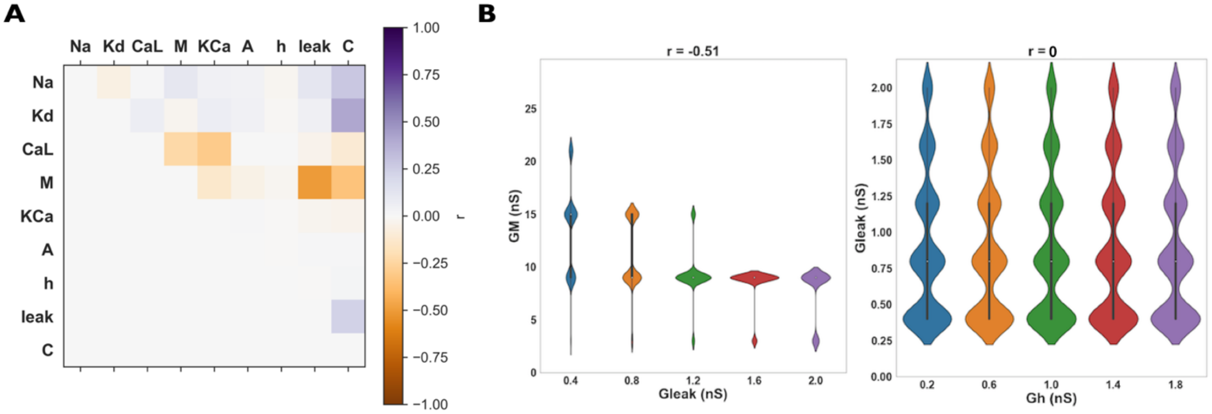

Figure 5.3 Ion channel correlations in all physiologically-realistic tSPN models. (A) Correlation matrix of all pairs of parameters, where each parameter is indicated on the axis label. Correlations are measured by Pearson's correlation coefficients, and fall within the range of [-1, 1]. **(B)** Violin plots showing the distribution of ion channel correlations. Correlation values are indicated in the title. Left: G_M vs. G_{leak}. Right: G_h vs. G_{leak}.

References

Achard P, De Schutter E (2006) Complex parameter landscape for a complex neuron model. PLoS Comput Biol 2:e94.

Amendola J, Woodhouse A, Martin-Eauclaire M-F, Goaillard J-M (2012) Ca^{2+}/cAMP-sensitive covariation of I(A) and I(H) voltage dependences tunes rebound firing in dopaminergic neurons. J Neurosci 32:2166–2181.

Anirudhan A, Narayanan R (2015) Analogous synaptic plasticity profiles emerge from disparate channel combinations. J Neurosci 35:4691–4705.

Attneave F (1954) Some informational aspects of visual perception. Psychol Rev 61:183–193.

Ayroles JF, Buchanan SM, O'Leary C, Skutt-Kakaria K, Grenier JK, Clark AG, Hartl DL, de Bivort BL (2015) Behavioral idiosyncrasy reveals genetic control of phenotypic variability. Proc Natl Acad Sci USA 112:6706–6711.

Bahuguna J, Tetzlaff T, Kumar A, Hellgren Kotaleski J, Morrison A (2017) Homologous Basal Ganglia Network Models in Physiological and Parkinsonian Conditions. Frontiers in Computational Neuroscience 11:79.

Ball JM, Franklin CC, Tobin A-E, Schulz DJ, Nair SS (2010) Coregulation of ion channel conductances preserves output in a computational model of a crustacean cardiac motor neuron. J Neurosci 30:8637–8649.

Bergquist S, Dickman DK, Davis GW (2010) A hierarchy of cell intrinsic and target-derived homeostatic signaling. Neuron 66:220–234.

Berman GJ, Bialek W, Shaevitz JW (2016) Predictability and hierarchy in Drosophila behavior. PNAS 113:11943–11948.

Beverly M, Anbil S, Sengupta P (2011) Degeneracy and neuromodulation among thermosensory neurons contribute to robust thermosensory behaviors in Caenorhabditis elegans. J Neurosci 31:11718–11727.

Bhalla US, Bower JM (1993) Exploring parameter space in detailed single neuron models: simulations of the mitral and granule cells of the olfactory bulb. Journal of Neurophysiology 69:1948–1965.

Blackman JG, Purves RD (1969) Intracellular recordings from ganglia of the thoracic sympathetic chain of the guinea-pig. The Journal of Physiology 203:173–198.

Bratton B, Davies P, Jänig W, McAllen R (2010) Ganglionic transmission in a vasomotor pathway studied in vivo. The Journal of Physiology 588:1647–1659.

Bucher D, Prinz AA, Marder E (2005) Animal-to-animal variability in motor pattern production in adults and during growth. J Neurosci 25:1611–1619.

Burdakov D (2005) Gain Control by Concerted Changes in IAand IHConductances. Neural Comput 17:991–995.

Butts DA, Weng C, Jin J, Yeh C-I, Lesica NA, Alonso J-M, Stanley GB (2007) Temporal precision in the neural code and the timescales of natural vision. Nature 449:92–95.

Buzsaki G (2006) Rhythms of the Brain.

Cannon J, Miller P (2016) Synaptic and intrinsic homeostasis cooperate to optimize single neuron response properties and tune integrator circuits. Journal of Neurophysiology 116:2004–2022.

Cao X-J, Oertel D (2011) The magnitudes of hyperpolarization-activated and low-voltage-activated potassium currents co-vary in neurons of the ventral cochlear nucleus. Journal of Neurophysiology 106:630–640.

Caplan JS, Williams AH, Marder E (2014) Many parameter sets in a multicompartment model oscillator are robust to temperature perturbations. J Neurosci 34:4963–4975.

Chen K, Aradi I, Thon N, Eghbal-Ahmadi M, Baram TZ, Soltesz I (2001) Persistently modified h-channels after complex febrile seizures convert the seizure-induced enhancement of inhibition to hyperexcitability. Nat Med 7:331–337.

Cope TC, Pinter MJ (1995) The Size Principle: Still Working After All These Years. Physiology 10:280–286.

Craver CF (2014) Levels.

Cropper EC, Dacks AM, Weiss KR (2016) Consequences of degeneracy in network function. Current Opinion in Neurobiology 41:62–67.

Cudmore RH, Fronzaroli-Molinieres L, Giraud P, Debanne D (2010) Spike-time precision and network synchrony are controlled by the homeostatic regulation of the D-type potassium current. J Neurosci 30:12885–12895.

Daniels BC, Chen Y-J, Sethna JP, Gutenkunst RN, Myers CR (2008) Sloppiness, robustness, and evolvability in systems biology. Curr Opin Biotechnol 19:389–395.

Das I and Dennis J (1998) Normal-boundary intersection: A new method for generating the Pareto surface in nonlinear multicriteria optimization problems. SIAM Journal of Optimization, vol. 8, no. 3, pp. 631–657.

Daur N, Nadim F, Bucher D (2016) The complexity of small circuits: the stomatogastric nervous system. Current Opinion in Neurobiology 41:1–7.

Dayan, P., Abbott, L. F., & Abbott, L. (2001). Theoretical neuroscience: computational and mathematical modeling of neural systems.

Davis GW (2006) Homeostatic control of neural activity: from phenomenology to molecular design. Annu Rev Neurosci 29:307–323.

Davis GW, DiAntonio A, Petersen SA, Goodman CS (1998) Postsynaptic PKA controls quantal size and reveals a retrograde signal that regulates presynaptic transmitter release in Drosophila. Neuron 20:305–315.

Deb K, Pratap A, Agarwal S, Meyarivan T (2002) A fast and elitist multiobjective genetic algorithm: NSGA-II. IEEE Trans Evol Computat 6:182–197.

Deb K, Jain H: An Evolutionary Many-Objective Optimization Algorithm Using Reference-Point-Based Nondominated Sorting Approach, Part I: Solving Problems With Box Constraints. *IEEE Trans Evol Computat* 2014, **18**:577–601.

Doloc-Mihu A, Calabrese RL (2014) Identifying crucial parameter correlations maintaining bursting activity. Graham LJ, ed. PLoS Comput Biol 10:e1003678.

Drion G, O'Leary T, Marder E (2015) Ion channel degeneracy enables robust and tunable neuronal firing rates. Proc Natl Acad Sci USA 112:E5361–E5370.

Druckmann S, Banitt Y, Gidon A, Schürmann F, Markram H, Segev I (2007) A novel multiple objective optimization framework for constraining conductance-based neuron models by experimental data. Front Neurosci 1:7–18.

Echegoyen J, Neu A, Graber KD, Soltesz I (2007) Homeostatic plasticity studied using in vivo hippocampal activity-blockade: synaptic scaling, intrinsic plasticity and age-dependence. Nicolelis M, ed. PLoS ONE 2:e700.

Edelman GM, Gally JA (2001) Degeneracy and complexity in biological systems. PNAS 98:13763–13768.

Eisen JS, Marder E (1982) Mechanisms underlying pattern generation in lobster stomatogastric ganglion as determined by selective inactivation of identified neurons. III. Synaptic connections of electrically coupled pyloric neurons. Journal of Neurophysiology 48:1392–1415.

Ermentrout, G. B., & Terman, D. H. (2010). *Mathematical foundations of neuroscience* (Vol. 35). Springer Science & Business Media.

Errington TM, Iorns E, Gunn W, Tan FE, Lomax J, Nosek BA (2014) An open investigation of the reproducibility of cancer biology research. Elife 3:5773.

Fong M-F, Newman JP, Potter SM, Wenner P (2015) Upward synaptic scaling is dependent on neurotransmission rather than spiking. Nat Commun 6:6339.

Fortin F-A, Parizeau M (2013) Revisiting the NSGA-II crowding-distance computation. In, pp 623–630. New York, New York, USA: ACM Press.

Furlan A, La Manno G, Lübke M, Häring M, Abdo H, Hochgerner H, Kupari J, Usoskin D, Airaksinen MS, Oliver G, Linnarsson S, Ernfors P (2016) Visceral motor neuron diversity delineates a cellular basis for nipple- and pilo-erection muscle control. Nat Neurosci 19:1331–1340.

Galvan M, Sedlmeir C (1984) Outward currents in voltage-clamped rat sympathetic neurones. The Journal of Physiology 356:115–133.

Gao P, Ganguli S (2015) On simplicity and complexity in the brave new world of large-scale neuroscience. Current Opinion in Neurobiology 32:148–155.

Gautrais J, Thorpe S (1998) Rate coding versus temporal order coding: a theoretical approach. BioSystems 48:57–65.

Goaillard J-M, Taylor AL, Schulz DJ, Marder E (2009) Functional consequences of animal-to-animal variation in circuit parameters. Nat Neurosci 12:1424–1430.

Goldman MS, Golowasch J, Marder E, Abbott LF (2001) Global structure, robustness, and modulation of neuronal models. J Neurosci 21:5229–5238.

Golowasch J (2014) Ionic Current Variability and Functional Stability in the Nervous System. Bioscience 64:570–580.

Golowasch J, Abbott LF, Marder E (1999) Activity-dependent regulation of potassium currents in an identified neuron of the stomatogastric ganglion of the crab Cancer borealis. J Neurosci 19:RC33.

Golowasch J, Buchholtz F, Epstein IR, Marder E (1992) Contribution of individual ionic currents to activity of a model stomatogastric ganglion neuron. Journal of Neurophysiology 67:341–349.

Golowasch J, Goldman MS, Abbott LF, Marder E (2002) Failure of Averaging in the Construction of a Conductance-Based Neuron Model. Journal of Neurophysiology 87:1129–1131.

Golowasch J, Marder E (1992) Proctolin activates an inward current whose voltage dependence is modified by extracellular Ca2+. J Neurosci 12:810–817.

Gonzalez-Islas C, Bülow P, Wenner P (2018) Regulation of synaptic scaling by action potential-independent miniature neurotransmission. J Neurosci Res 96:348–353.

Gonzalez-Islas C, Wenner P (2006) Spontaneous network activity in the embryonic spinal cord regulates AMPAergic and GABAergic synaptic strength. Neuron 49:563–575.

Gorur-Shandilya S, Marder E, O'Leary T (2019) Homeostatic plasticity rules that compensate for cell size are susceptible to channel deletion. bioRxiv 271:753608.

Grashow R, Brookings T, Marder E (2010) Compensation for variable intrinsic neuronal excitability by circuit-synaptic interactions. J Neurosci 30:9145–9156.

Greenhill SD, Ranson A, Fox K (2015) Hebbian and Homeostatic Plasticity Mechanisms in Regular Spiking and Intrinsic Bursting Cells of Cortical Layer 5. Neuron 88:539–552.

Gutenkunst RN, Waterfall JJ, Casey FP, Brown KS, Myers CR, Sethna JP (2007) Universally Sloppy Parameter Sensitivities in Systems Biology Models. PLoS Comput Biol 3:e189.

Gutierrez GJ, O'Leary T, Marder E (2013) Multiple mechanisms switch an electrically coupled, synaptically inhibited neuron between competing rhythmic oscillators. Neuron 77:845–858.

Guyenet PG (2006) The sympathetic control of blood pressure. Nature Reviews Neuroscience 7:335–346.

Günay C, Edgerton JR, Jaeger D (2008) Channel density distributions explain spiking variability in the globus pallidus: a combined physiology and computer simulation database approach. J Neurosci 28:7476–7491.

Günay C, Prinz AA (2010) Model calcium sensors for network homeostasis: sensor and readout parameter analysis from a database of model neuronal networks. J Neurosci 30:1686–1698.

Haddad SA, Marder E (2018) Circuit Robustness to Temperature Perturbation Is Altered by Neuromodulators. Neuron 100:609–623.e3.

Hartline DK, Gassie DV (1979) Pattern generation in the lobster (Panulirus) stomatogastric ganglion. I. Pyloric neuron kinetics and synaptic interactions. Biol Cybern 33:209–222.

Hendrickson EB, Edgerton JR, Jaeger D (2011) The use of automated parameter searches to improve ion channel kinetics for neural modeling. J Comput Neurosci 31:329–346.

Hengen KB, Lambo ME, Van Hooser SD, Katz DB, Turrigiano GG (2013) Firing rate homeostasis in visual cortex of freely behaving rodents. Neuron 80:335–342.

Hengen KB, Torrado Pacheco A, McGregor JN, Van Hooser SD, Turrigiano GG (2016) Neuronal Firing Rate Homeostasis Is Inhibited by Sleep and Promoted by Wake. Cell 165:180–191.

Hooper SL, Marder E (1987) Modulation of the lobster pyloric rhythm by the peptide proctolin. J Neurosci 7:2097–2112.

Hou S, Rabchevsky AG (2014) Autonomic consequences of spinal cord injury. Compr Physiol 4:1419–1453.

Hudson AE, Gollnick C, Gourdine J-P, Prinz AA (2015) Degradation of extracellular chondroitin sulfate delays recovery of network activity after perturbation. Journal of Neurophysiology 114:1346–1352.

Hudson AE, Prinz AA (2010) Conductance Ratios and Cellular Identity Gutkin BS, ed. PLoS Comput Biol 6:e1000838.

Ibata K, Sun Q, Turrigiano GG (2008) Rapid Synaptic Scaling Induced by Changes in Postsynaptic Firing. Neuron 57:819–826.

Ioannidis JPA (2005) Why most published research findings are false. PLoS Med 2:e124.

Jänig W (2008) Integrative action of the autonomic nervous system: Neurobiology of homeostasis.

Jobling P, Gibbins IL (1999) Electrophysiological and morphological diversity of mouse sympathetic neurons. Journal of Neurophysiology 82:2747–2764.

Kandel ER, Schwartz JH, Jessell TM (2000) Principles of neural science.

Karila P, Horn JP (2000) Secondary nicotinic synapses on sympathetic B neurons and their putative role in ganglionic amplification of activity. J Neurosci 20:908–918.

Karlsson AK (1999) Autonomic dysreflexia. Spinal Cord 37:383–391.

Karmarkar UR, Buonomano DV (2006) Different forms of homeostatic plasticity are engaged with distinct temporal profiles. Eur J Neurosci 23:1575–1584.

Kazantsev V, Gordleeva S, Stasenko S, Dityatev A (2012) A homeostatic model of neuronal firing governed by feedback signals from the extracellular matrix. Tsilibary EC, ed. PLoS ONE 7:e41646.

Keck T, Keller GB, Jacobsen RI, Eysel UT, Bonhoeffer T, Hübener M (2013) Synaptic Scaling and Homeostatic Plasticity in the Mouse Visual Cortex In Vivo. Neuron 80:327–334.

Kerchner GA, Nicoll RA (2008) Silent synapses and the emergence of a postsynaptic mechanism for LTP. Nature Reviews Neuroscience 9:813–825.

Khorkova O, Golowasch J (2007) Neuromodulators, not activity, control coordinated expression of ionic currents. J Neurosci 27:8709–8718.

Kim EZ, Vienne J, Rosbash M, Griffith LC (2017) Nonreciprocal homeostatic compensation in Drosophila potassium channel mutants. Journal of Neurophysiology 117:2125–2136.

Kirov SA, Harris KM (1999) Dendrites are more spiny on mature hippocampal neurons when synapses are inactivated. Nat Neurosci 2:878–883.

Klassen SA, Limberg JK, Baker SE, Nicholson WT, Curry TB, Joyner MJ, Shoemaker JK (2018) The role of the paravertebral ganglia in human sympathetic neural discharge patterns. The Journal of Physiology 596:4497–4510.

König P, Engel AK, Singer W (1996) Integrator or coincidence detector? The role of the cortical neuron revisited. Trends in Neurosciences 19:130–137.

Krenz W-DC, Hooper RM, Parker AR, Prinz AA, Baro DJ (2013) Activation of high and low affinity dopamine receptors generates a closed loop that maintains a conductance ratio and its activity correlate. Frontiers in Neural Circuits 7:169.

Krenz W-DC, Parker AR, Rodgers EW, Baro DJ (2014) Dopaminergic tone persistently regulates voltage-gated ion current densities through the D1R-PKA axis, RNA polymerase II transcription, RNAi, mTORC1, and translation. Front Cell Neurosci 8.

Krenz WD, Parker AR, Rodgers E (2015) Monoaminergic tone supports conductance correlations and stabilizes activity features in pattern generating neurons of the lobster, Panulirus interruptus. Frontiers in Neural Circuits.

Kullmann PHM, Sikora KM, Clark KL, Arduini I, Springer MG, Horn JP (2016) HCN hyperpolarization-activated cation channels strengthen virtual nicotinic EPSPs and thereby elevate synaptic amplification in rat sympathetic neurons. Journal of Neurophysiology 116:438–447.

Kurian M, Crook SM, Jung R (2011) Motoneuron model of self-sustained firing after spinal cord injury. J Comput Neurosci 31:625–645.

Lamb DG, Calabrese RL (2013) Correlated conductance parameters in leech heart motor neurons contribute to motor pattern formation. Coleman MJ, ed. PLoS ONE 8:e79267.

Lambo ME, Turrigiano GG (2013) Synaptic and intrinsic homeostatic mechanisms cooperate to increase L2/3 pyramidal neuron excitability during a late phase of critical period plasticity. J Neurosci 33:8810–8819.

Lane BJ, Samarth P, Ransdell JL, Nair SS, Schulz DJ (2016) Synergistic plasticity of intrinsic conductance and electrical coupling restores synchrony in an intact motor network. Elife 5:2166.

Lees GM, Wallis DI (1974) Hyperpolarization of rabbit superior cervical ganglion cells due to activity of an electrogenic sodium pump. British Journal of Pharmacology 50:79–93.

LeMasson G, Marder E, Abbott LF (1993) Activity-dependent regulation of conductances in model neurons. Science 259:1915–1917.

Leonardo A (2005) Degenerate coding in neural systems. J Comp Physiol A Neuroethol Sens Neural Behav Physiol 191:995–1010.

Lichtman JW, Purves D, Yip JW (1980) Innervation of sympathetic neurones in the guinea-pig thoracic chain. The Journal of Physiology 298:285–299.

Liu Z, Golowasch J, Marder E, Abbott LF (1998) A model neuron with activity-dependent conductances regulated by multiple calcium sensors. J Neurosci 18:2309–2320.

Luke, S. Essentials of Metaheuristics. Lulu, 2013. *URL http://cs.gmu.edu/sean/book/metaheuristics*.

Luther JA, Robie AA, Yarotsky J, Reina C, Marder E, Golowasch J (2003) Episodic bouts of activity accompany recovery of rhythmic output by a neuromodulator- and activity-deprived adult neural network. Journal of Neurophysiology 90:2720–2730.

Lütcke H, Margolis DJ, Helmchen F (2013) Steady or changing? Long-term monitoring of neuronal population activity. Trends in Neurosciences 36:375–384.

Macefield VG, Wallin BG (2018) Physiological and pathophysiological firing properties of single postganglionic sympathetic neurons in humans. Journal of Neurophysiology 119:944–956.

MacLean JN, Zhang Y, Goeritz ML, Casey R, Oliva R, Guckenheimer J, Harris-Warrick RM (2005) Activity-Independent Coregulation of IA and Ih in Rhythmically Active Neurons. Journal of Neurophysiology 94:3601–3617.

MacLean JN, Zhang Y, Johnson BR, Harris-Warrick RM (2003) Activity-independent homeostasis in rhythmically active neurons. Neuron 37:109–120.

Maffei A, Turrigiano GG (2008) Multiple modes of network homeostasis in visual cortical layer 2/3. J Neurosci 28:4377–4384.

Malenka RC, Nicoll RA (1997) Silent Synapses Speak Up. Neuron 19:473–476 Available at: http://www.sciencedirect.com/science/article/pii/S0896627300803621.

Man M, Zhang Y, Ma G, Friston K, Liu S (2016) Quantification of degeneracy in Hodgkin-Huxley neurons on Newman-Watts small world network. Journal of Theoretical Biology 402:62–74.

Marder E (2015) Understanding brains: details, intuition, and big data. PLoS Biol 13:e1002147.

Marder E, Eisen JS (1984) Transmitter identification of pyloric neurons: electrically coupled neurons use different transmitters. Journal of Neurophysiology 51:1345–1361.

Marder E, Goaillard J-M (2006) Variability, compensation and homeostasis in neuron and network function. Nature Reviews Neuroscience 7:563–574.

Marder E, Taylor AL (2011) Multiple models to capture the variability in biological neurons and networks. Nat Neurosci 14:133–138.

Mason PH (2015) Degeneracy: Demystifying and destigmatizing a core concept in systems biology. Complexity 20:12–21.

Mason PH, Domínguez D JF, Winter B, Grignolio A (2015) Hidden in plain view: degeneracy in complex systems. BioSystems 128:1–8.

McConnell MJ et al. (2017) Intersection of diverse neuronal genomes and neuropsychiatric disease: The Brain Somatic Mosaicism Network. Science 356:eaal1641.

McKinnon ML, Tian K, Li Y, Sokoloff AJ, Galvin ML, Choi MH, Prinz A, Hochman S (2019) Dramatically Amplified Thoracic Sympathetic Postganglionic Excitability and Integrative Capacity Revealed with Whole-Cell Patch-Clamp Recordings. eNeuro 6:ENEURO.0433–18.2019.

McLachlan EM (2007) Diversity of sympathetic vasoconstrictor pathways and their plasticity after spinal cord injury. Clin Auton Res 17:6–12.

Mendell LM (2005) The size principle: a rule describing the recruitment of motoneurons. Journal of Neurophysiology 93:3024–3026.

Mizrahi A, Dickinson PS, Kloppenburg P, Fénelon V, Baro DJ, Harris-Warrick RM, Meyrand P, Simmers J (2001) Long-term maintenance of channel distribution in a central pattern generator neuron by neuromodulatory inputs revealed by decentralization in organ culture. J Neurosci 21:7331–7339.

Murthy VN, Schikorski T, Stevens CF, Zhu Y (2001) Inactivity produces increases in neurotransmitter release and synapse size. Neuron 32:673–682.

O'Leary T, Williams AH, Caplan JS, Marder E (2013) Correlations in ion channel expression emerge from homeostatic tuning rules. Proc Natl Acad Sci USA 110:E2645–E2654.

O'Leary T, Williams AH, Franci A, Marder E (2014) Cell types, network homeostasis, and pathological compensation from a biologically plausible ion channel expression model. Neuron 82:809–821.

O'Leary T, Wyllie DJA (2011) Neuronal homeostasis: time for a change? The Journal of Physiology 589:4811–4826.

Olypher AV, Prinz AA (2010) Geometry and dynamics of activity-dependent homeostatic regulation in neurons. J Comput Neurosci 28:361–374.

Otopalik AG, Pipkin J, Marder E (2019) Neuronal morphologies built for reliable physiology in a rhythmic motor circuit. Elife 8:9151.

Otopalik AG, Sutton AC, Banghart M, Marder E (2017) When complex neuronal structures may not matter. Elife 6:2066.

O’Brien RJ, Kamboj S, Ehlers MD, Rosen KR, Fischbach GD, Huganir RL (1998) Activity-Dependent Modulation of Synaptic AMPA Receptor Accumulation. Neuron 21:1067–1078.

Panas D, Amin H, Maccione A, Muthmann O, van Rossum M, Berdondini L, Hennig MH (2015) Sloppiness in spontaneously active neuronal networks. J Neurosci 35:8480–8492.

Picton LD, Zhang H, Sillar KT (2017) Sodium pump regulation of locomotor control circuits. Journal of Neurophysiology 118:1070–1081.

Prescott SA, Ratté S, De Koninck Y, Sejnowski TJ (2006) Nonlinear interaction between shunting and adaptation controls a switch between integration and coincidence detection in pyramidal neurons. J Neurosci 26:9084–9097.

Prinz AA (2010a) Computational approaches to neuronal network analysis. Philosophical Transactions: Biological Sciences 365:2397–2405.

Prinz AA (2010b) Computational approaches to neuronal network analysis. Philos Trans R Soc Lond, B, Biol Sci 365:2397–2405.

Prinz AA, Billimoria CP, Marder E (2003) Alternative to hand-tuning conductance-based models: construction and analysis of databases of model neurons. Journal of Neurophysiology 90:3998–4015.

Prinz AA, Bucher D, Marder E (2004) Similar network activity from disparate circuit parameters. Nat Neurosci 7:1345–1352.

Queenan BN, Lee KJ, Pak DTS, Queenan BN, Lee KJ, Pak DTS (2012) Wherefore Art Thou, Homeo(stasis)? Functional Diversity in Homeostatic Synaptic Plasticity. Neural Plasticity 2012:1–12.

Ransdell JL, Nair SS, Schulz DJ (2012) Rapid homeostatic plasticity of intrinsic excitability in a central pattern generator network stabilizes functional neural network output. J Neurosci 32:9649–9658.

Ransdell JL, Nair SS, Schulz DJ (2013a) Neurons within the same network independently achieve conserved output by differentially balancing variable conductance magnitudes. J Neurosci 33:9950–9956.

Ransdell JL, Temporal S, West NL, Leyrer ML, Schulz DJ (2013b) Characterization of inward currents and channels underlying burst activity in motoneurons of crab cardiac ganglion. Journal of Neurophysiology 110:42–54.

Ratté S, Hong S, De Schutter E, Prescott SA (2013) Impact of neuronal properties on network coding: roles of spike initiation dynamics and robust synchrony transfer. Neuron 78:758–772.

Ratté S, Prescott SA (2016) Afferent hyperexcitability in neuropathic pain and the inconvenient truth about its degeneracy. Current Opinion in Neurobiology 36:31–37.

Ratté S, Zhu Y, Lee KY, Prescott SA (2014) Criticality and degeneracy in injury-induced changes in primary afferent excitability and the implications for neuropathic pain. Elife 3:e02370.

Rho Y-A, Prescott SA (2012) Identification of molecular pathologies sufficient to cause neuropathic excitability in primary somatosensory afferents using dynamical systems theory. Gutkin BS, ed. PLoS Comput Biol 8:e1002524.

Rimmer K, Horn JP (2010) Weak and straddling secondary nicotinic synapses can drive firing in rat sympathetic neurons and thereby contribute to ganglionic amplification. Front Neurol 1:130.

Rittenhouse AR, Zigmond RE (1999) Role of N- and L-type calcium channels in depolarization-induced activation of tyrosine hydroxylase and release of norepinephrine by sympathetic cell bodies and nerve terminals. J Neurobiol 40:137–148.

Rush ME, Rinzel J (1995) The potassium A-current, low firing rates and rebound excitation in hogkin-huxley models. Bulletin of mathematical biology 2:299–312.

Sacchi O, Rossi ML, Canella R (1995) The slow Ca(2+)-activated K+ current, IAHP, in the rat sympathetic neurone. The Journal of Physiology 483 (Pt 1):15–27.

Schulz DJ, Goaillard J-M, Marder E (2006) Variable channel expression in identified single and electrically coupled neurons in different animals. Nat Neurosci 9:356–362.

Schulz DJ, Goaillard J-M, Marder EE (2007) Quantitative expression profiling of identified neurons reveals cell-specific constraints on highly variable levels of gene expression. PNAS 104:13187–13191.

Schulz DJ, Lane BJ (2017) Homeostatic plasticity of excitability in crustacean central pattern generator networks. Current Opinion in Neurobiology 43:7–14.

Science OSC, 2015 (n.d.) Estimating the reproducibility of psychological science. sciencesciencemagorg.

Sivagnanam S, Majumdar A, Yoshimoto K, Astakhov V, Bandrowski A, Martone ME, and Carnevale NT. Introducing the Neuroscience Gateway, IWSG, volume 993 of CEUR Workshop Proceedings, CEUR-WS.org, 2013

Slomowitz E, Styr B, Vertkin I, Milshtein-Parush H, Nelken I, Slutsky M, Slutsky I (2015) Interplay between population firing stability and single neuron dynamics in hippocampal networks. Elife 4:126.

Soofi W, Archila S, Prinz AA (2012) Co-variation of ionic conductances supports phase maintenance in stomatogastric neurons. J Comput Neurosci 33:77–95.

Soofi W, Goeritz ML, Kispersky TJ, Prinz AA, Marder E, Stein W (2014) Phase maintenance in a rhythmic motor pattern during temperature changes in vivo. Journal of Neurophysiology 111:2603–2613.

Soto-Treviño C, Thoroughman KA, Marder E, Abbott LF (2001) Activity-dependent modification of inhibitory synapses in models of rhythmic neural networks. Nat Neurosci 4:297–303.

Springer MG, Kullmann PHM, Horn JP (2015) Virtual leak channels modulate firing dynamics and synaptic integration in rat sympathetic neurons: implications for ganglionic transmission in vivo. The Journal of Physiology 593:803–823.

Staley KJ, Otis TS, Mody I (1992) Membrane properties of dentate gyrus granule cells: comparison of sharp microelectrode and whole-cell recordings. Journal of Neurophysiology 67:1346–1358.

Steinback CD, Salmanpour A, Breskovic T, Dujic Z, Shoemaker JK (2010) Sympathetic neural activation: an ordered affair. The Journal of Physiology 588:4825–4836.

Swensen AM, Bean BP (2005) Robustness of burst firing in dissociated purkinje neurons with acute or long-term reductions in sodium conductance. J Neurosci 25:3509–3520.

Swensen AM, Marder E (2000) Multiple peptides converge to activate the same voltage-dependent current in a central pattern-generating circuit. J Neurosci 20:6752–6759.

Taylor AL, Goaillard J-M, Marder E (2009) How multiple conductances determine electrophysiological properties in a multicompartment model. J Neurosci 29:5573–5586.

Taylor AL, Hickey TJ, Prinz AA, Marder E (2006) Structure and Visualization of High-Dimensional Conductance Spaces. Journal of Neurophysiology 96:891–905.

Temporal S, Desai M, Khorkova O, Varghese G, Dai A, Schulz DJ, Golowasch J (2012) Neuromodulation independently determines correlated channel expression and conductance levels in motor neurons of the stomatogastric ganglion. Journal of Neurophysiology 107:718–727.

Temporal S, Lett KM, Schulz DJ (2014) Activity-dependent feedback regulates correlated ion channel mRNA levels in single identified motor neurons. Curr Biol 24:1899–1904.

Thoby-Brisson M, Simmers J (1998) Neuromodulatory inputs maintain expression of a lobster motor pattern-generating network in a modulation-dependent state: evidence from long-term decentralization in vitro. J Neurosci 18:2212–2225.

Thoby-Brisson M, Simmers J (2002) Long-term neuromodulatory regulation of a motor pattern-generating network: maintenance of synaptic efficacy and oscillatory properties. Journal of Neurophysiology 88:2942–2953.

Tononi G, Sporns O, Edelman GM (1999) Measures of degeneracy and redundancy in biological networks. PNAS 96:3257–3262.

Tran T, Unal CT, Severin D, Zaborszky L, Rotstein HG, Kirkwood A, Golowasch J (2019) Ionic current correlations are ubiquitous across phyla. Sci Rep 9:1687.

Transtrum MK, Machta BB, Brown KS, Daniels BC, Myers CR, Sethna JP (2015) Perspective: Sloppiness and emergent theories in physics, biology, and beyond. J Chem Phys 143:010901.

Triesch J (2007) Synergies between intrinsic and synaptic plasticity mechanisms. Neural Comput 19:885–909.

Turrigiano G (2011) Too many cooks? Intrinsic and synaptic homeostatic mechanisms in cortical circuit refinement. Annu Rev Neurosci 34:89–103.

Turrigiano G (2012) Homeostatic synaptic plasticity: local and global mechanisms for stabilizing neuronal function. Cold Spring Harb Perspect Biol 4:a005736–a005736.

Turrigiano G, Abbott LF, Marder E (1994) Activity-dependent changes in the intrinsic properties of cultured neurons. Science 264:974–977.

Turrigiano G, LeMasson G, Marder E (1995) Selective regulation of current densities underlies spontaneous changes in the activity of cultured neurons. J Neurosci 15:3640–3652.

Turrigiano GG, Leslie KR, Desai NS, Rutherford LC, Nelson SB (1998) Activity-dependent scaling of quantal amplitude in neocortical neurons. Nature 391:892–896.

Turrigiano GG, Nelson SB (2000) Hebb and homeostasis in neuronal plasticity. Current Opinion in Neurobiology 10:358–364.

Van der Maaten L, Hinton G (2008) Visualizing data using t-SNE. Journal of Machine Learning ….

Van Geit W, De Schutter E, Achard P (2008) Automated neuron model optimization techniques: a review. Biol Cybern 99:241–251.

VanRullen R, Guyonneau R, Thorpe SJ (2005) Spike times make sense. Trends in Neurosciences 28:1–4.

Vertkin I, Styr B, Slomowitz E, Ofir N, Shapira I, Berner D, Fedorova T, Laviv T, Barak-Broner N, Greitzer-Antes D, Gassmann M, Bettler B, Lotan I, Slutsky I (2015) GABAB receptor deficiency causes failure of neuronal homeostasis in hippocampal networks. Proc Natl Acad Sci USA 112:E3291–E3299.

Vitureira N, Letellier M, Goda Y (2012) Homeostatic synaptic plasticity: from single synapses to neural circuits. Current Opinion in Neurobiology 22:516–521.

Wheeler DW, Kullmann PHM, Horn JP (2004) Estimating use-dependent synaptic gain in autonomic ganglia by computational simulation and dynamic-clamp analysis. Journal of Neurophysiology 92:2659–2671.

Wilhelm JC, Rich MM, Wenner P (2009) Compensatory changes in cellular excitability, not synaptic scaling, contribute to homeostatic recovery of embryonic network activity. Proc Natl Acad Sci USA 106:6760–6765.

Wilhelm JC, Wenner P (2008) GABAA transmission is a critical step in the process of triggering homeostatic increases in quantal amplitude. Proc Natl Acad Sci USA 105:11412–11417.

Zhang Y, Golowasch J (2011) Recovery of rhythmic activity in a central pattern generator: analysis of the role of neuromodulator and activity-dependent mechanisms. J Comput Neurosci 31:685–699.

Zhao S, Golowasch J (2012) Ionic current correlations underlie the global tuning of large numbers of neuronal activity attributes. J Neurosci 32:13380–13388.